Influence of Protein and Lipid Domains on the Structure, Fluidity and Phase Behavior of Lipid Bilayer Membranes

by

MARGARET R. HORTON

Bachelor of Science, Chemical Engineering
Purdue University, 2002

Submitted to the Department of Chemical Engineering in Partial Fulfillment of the Requirements for the Degree of

DOCTOR OF PHILOSOPHY IN CHEMICAL ENGINEERING

at the

MASSACHUSETTS INSTITUTE OF TECHNOLOGY

February 2007

Author_____
Margaret R. Horton
Department of Chemical Engineering
December 21, 2006

Certified by_____
Alice P. Gast
Adjunct Professor of Chemical Engineering
Thesis Supervisor

Accepted by_____
William M. Deen
Professor of Chemical Engineering
Chairman, Committee for Graduate Students

Influence of Protein and Lipid Domains on the Structure, Fluidity and Phase Behavior of Lipid Bilayer Membranes

by

Margaret R. Horton

Abstract

The lipid bilayer forms the basic structure of the cell membrane, which is a heterogeneous matrix of proteins and lipids that provides a barrier between the interior of a cell and its outside environment. Protein and lipid domains in cell membranes can facilitate receptor localization, stabilize membranes, and influence membrane fluidity. In this thesis, we study how ordered protein and lipid domains influence the physical properties of lipid bilayers to better understand the roles of membrane domains in biological mechanisms. Model cellular membranes that mimic the behavior of biological membranes offer a controllable environment for systematically studying the isolated effects of protein and lipid ordering on membrane organization. Using fluid and solid-supported lipid bilayers, we study ordered peripheral membrane proteins and lateral lipid phase separation with fluorescence microscopy and X-ray reflectivity. To model cellular protein coatings and peripheral proteins, we prepare biotin-functionalized membranes that bind the proteins streptavidin and avidin. Fluorescence microscopy studies demonstrate that proteins crystallized in a single layer on lipid bilayer surfaces can change the lipid curvature and stabilize lipid vesicles against osmotic collapse. At solid interfaces, we characterize the electron density profiles of protein-coated bilayers to determine how a water layer separates an immobile protein layer from the fluid lipid bilayer. Liquid-ordered lipid phases enriched in cholesterol and sphingomyelin can localize molecules in cell membranes and this lipid phase separation behavior may be influenced by proteins and molecules in the membrane. Caveolae are specialized liquid-ordered domains in the plasma membrane that are enriched in the protein caveolin-1. We demonstrate that caveolin-1 peptides influence the onset of lipid phase separation and bind phase-separated lipid bilayers in solution. On solid surfaces, the formation of liquid-ordered lipid phases is influenced by surface roughness; with reflectivity, we determine that lipid bilayers containing cholesterol and sphingomyelin thicken with increasing cholesterol content. The membrane receptor GM1 also thickens the lipid bilayer when it is incorporated into the bilayer upper leaflet. The diverse experimental platforms that we present are applicable to studying additional and more complex biological systems to elucidate the influence of lipid and protein domains on cell membrane structure, organization and fluidity.

Thesis Supervisor: Alice P. Gast
Title: Adjunct Professor of Chemical Engineering

ACKNOWLEDGMENTS

I thank my advisor Alice Gast for her support during my graduate career. It is impressive and extraordinary how she wore so many hats at MIT as a professor and administrator. I feel honored to be her first PhD student at MIT. My thesis committee, Paul Matsudaira and Klaus Jensen have so helpful and patient as I have corresponded from Europe during the past few months and have offered invaluable feedback for my thesis research. I extend a sincere *herzlichen Dank* to my colleagues at the Ludwig-Maximilians-Universität in München; I would have never been able to complete this work without their support and guidance. The members of Lehrstuhl Rädler have been welcoming and always willing to discuss scientific problems and actively help me to improve my German language skills. I thank Prof. Dr. Joachim Rädler for his generosity as my host and mentor during my multiple research visits to Germany. I thank Dr. Bert Nickel and Christian Reich for inviting me to participate in their work at the European Synchrotron Radiation Facility; our X-ray reflectivity experiments have become an essential component of my thesis. I am so grateful for the opportunity to collaborate with Christian Reich, who was my untiring labmate during long synchrotron visits. I appreciate his patience in discussing our projects exclusively in German; he has indeed been my primary technical German language instructor. Suliana Manley has been an amazing scientific advisor, writing mentor and friend and I feel very fortunate that she was a postdoc in our laboratory. Her guidance in showing me how to write a clear scientific story based on our experiments was generous and invaluable.

My collaborators have been essential to the completion of my doctoral degree program and the chapters in this work are the result of collaboration. Joachim Rädler is the co-author of Chapter 3. Suliana Manley, undergraduate Silvana Arevalo and Alexander Lobkovsky of the Earth, Atmospheric and Planetary Sciences Department are co-authors of Chapter 4. Christian Reich, Bert Nickel and Joachim Rädler are the co-authors of Chapters 5 and 6.

Very importantly, I thank my parents and sister for their unconditional support.

TABLE OF CONTENTS

CHAPTER 1. INTRODUCTION

1.1 Background and Motivation

1.1.1 Function and Structure of Biological Membranes

The cell membrane provides a barrier between the interior of a cell and its outside environment and mediates the transport of molecules into and out of the cell. A continuous lipid bilayer is the base structure for all cell membranes and is described as a two-dimensional fluid comprising amphiphilic phospholipid molecules [1], shown schematically in Figure 1-1. Many of the protective and selective biological transport functions of the cell membrane are attributed to the unique structure of the lipid bilayer interface. Lipid molecules have a hydrophilic headgroup attached to fatty acid chains (Figure 1-1, *center*) and self-assemble into bilayers. The resulting interface has a hydrophobic core and the headgroups are exposed to the aqueous environments interior to and exterior to the cell. The hydrophobic core limits passage of ionic molecules through the membrane and the packed lipids resist passage of large molecules.

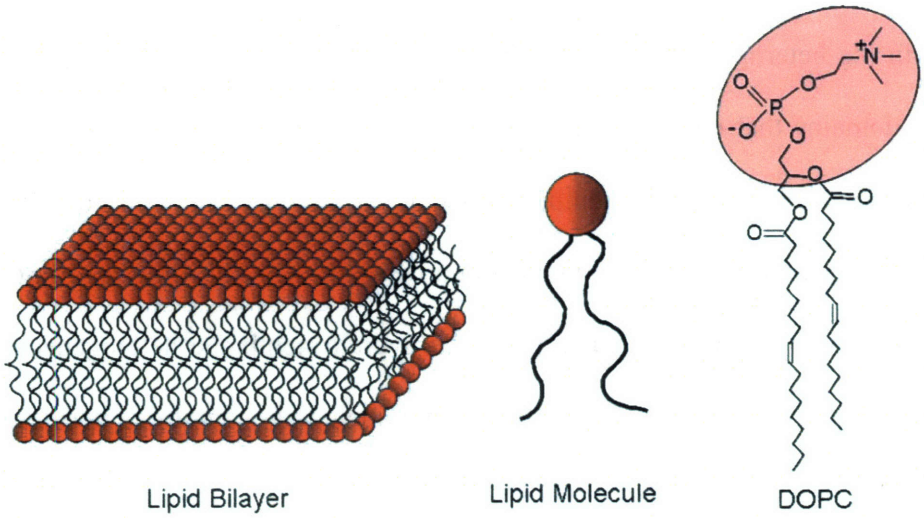

Figure 1-1. Schematic of lipid bilayer membrane (*left*), a single lipid molecule (*center*) and the unsaturated phospholipid dioleoylphosphatidylcholine or DOPC (*right*).

The lipid bilayer serves as a fluid matrix in which membrane proteins and protein complexes reside. Proteins are a significant part of the composition of cell membranes and are attached peripherally or imbedded within lipid bilayer membranes [1]; the nature of this physical arrangement can influence the overall membrane structure and fluidity and affect the organization of surrounding lipids.

1.1.2 Heterogeneity in Biological Membranes

In the heterogeneous cell membrane, both lipids and proteins can assemble into ordered domains that confer spatial organization to the membrane. Lipids can laterally phase separate into domains, membrane-associated proteins can form complexes in the cell membrane, and lipids can assemble around proteins [2]. This ordering of proteins and lipids into heterogeneous structures gives the overall membrane heterogeneous fluidity. The mechanical properties of the membrane, including curvature, permeability and stability, can be influenced by protein and lipid ordering.

1.1.2.1 Lipid Ordering in Cell Membranes

The concept of liquid-ordered lipid domains in the cell membrane has revised our understanding of membrane organization, as lipids can self-organize into lateral phases into which proteins can preferentially partition [3]. Lipid rafts, or detergent-insoluble domains of the plasma membrane enriched in cholesterol and sphingolipids, are thought to play a role in sequestering molecules to facilitate cell signaling. Interestingly, model lipid membrane experiments demonstrate lipid phase separation very similar to cellular membrane extracts; thus, simple lipid mixtures have provided an important basis for understanding lipid raft formation in cells [4]. The formation of lipid rafts is thought to be driven by packing among saturated lipids, sphingolipids and cholesterol to create a

liquid-ordered phase where different membrane molecules, including gangliosides [5], GPI-anchored proteins [6] and crosslinked lipid-associated proteins [7], reside.

The preferential partitioning of proteins and glycolipids into liquid-ordered phases of the cell membrane is a possible biological function of lipid rafts, where molecules collected in a particular phase are brought into closer proximity to enable binding and interaction. An important related mechanism is the induction of lipid phase separation by proteins, where proteins rearrange their local lipid environment into lipid phases. Model systems of proteins and lipids show that proteins bound to lipids can sort lipids into liquid-ordered domains [8, 9]. Lipid shell theory suggests that nanoscopic domains of proteins and contiguous lipids are targeted to other protein/lipid complexes to build large liquid-ordered lipid phases enriched in selective proteins [10]. The nature of protein interactions with phase-separated lipid membranes and the selective partitioning into lipid domains is not completely understood. Biological examples of proteins that associate with liquid-ordered lipid phases are caveolin-1 and cholera toxin, which binds to the ganglioside GM1. Caveolae are domains in the membrane with invaginated morphology that are important for lipid metabolism [11-15] that are identified by the presence of caveolin-1. The lipid composition of caveolae is similar to rafts, though it is unclear how caveolin-1 is targeted to these cholesterol and sphingolipids-enriched domains. Among the membrane molecules that can be localized to caveolae fractions of the membrane is the GM1 receptor, and the cholera toxin-GM1 complex may enter the cell by uptake through caveolae [16]. Model membrane experiments suggest that GM1 localization to

liquid-ordered lipid phases may be assisted by an induction of lipid phase separation, as GM1 can change the temperature-mediated onset of lipid phase separation [17, 18].

1.1.2.2 Protein Ordering in Cell Membranes

Since proteins are significant part of molecular composition of cell membranes and can interact with lipid domains, it is important to study the effect of protein ordering on lipid bilayer membranes. Proteins that order and self-assemble in cell membranes have many functions, including structural membrane deformation [19, 20] and transduction of external signals [21]. The lipid bilayer membrane is a highly flexible material capable of deforming into diverse shapes and proteins are often required to guide and direct membrane deformation. An example of protein-assisted membrane deformation is endocytosis, where the budding of the membrane into vesicles [19, 22] is assisted by the protein clathrin. The assembly of clathrin molecules into a well-defined lattice on the cellular membrane surface forms invaginations termed clathrin-coated pits that bud into the cell [23-25]. Similarly, transport vesicles that bud from the endoplasmic reticulum to traffic proteins in the cell are formed by insertion of the GTPase Sar1p into in the bilayer, which disrupts lipid packing and expands the area of the outer membrane leaflet [26, 27]. Caveolae are also part of an endocytotic pathway, though the filamentous protein coat found in caveolae and how it deforms the membrane is less understood [28, 29]. Monomolecular surface layers on archae and bacteria, termed S-layers, may play a role in the sieving of molecules crossing the membrane and physical protection of the cell [30]. Modification of the lipid bilayer is also an important biological function attributed to

membrane-associated proteins. Phospholipase A_2 binds lipid bilayers and catalyzes the hydrolysis of phospholipids into fatty acids and single-chained lipids, thus changing the lipid composition and increasing membrane heterogeneity [31]. As part of its mechanism to gain entry to cells, the B subunit of bacterial cholera toxin binds the membrane receptor GM1, forming pentagonal complex that eventually forms a pore through which cholera toxin crosses the membrane [16].

In this thesis, we examine both lipid and protein ordering in model lipid bilayer membranes. Our model membrane experiments, which allow us to isolate the effects of lipid ordering and protein-lipid interactions, may help us to understand how domains in cell membranes are important to the overall biological function of the membrane. We present studies of lipid ordering in fluid membranes in Chapter 3, where we study peptides derived from caveolin-1 interacting with model lipid rafts to understand how proteins can influence lipid phase separation. In Chapter 4, we study protein ordering and its influence on the shape and stability of lipid bilayer vesicles. In Chapters 5 and 6, we present our experiments combining X-ray reflectivity and fluorescence microscopy to study planar supported lipid bilayers. We combine these microscopic and nanoscopic techniques to study ordered proteins tethered to bilayers in Chapter 5. And in Chapter 6, we examine how a model membrane receptor influences the structure of the lipid membrane and we study the structure of bilayers with model lipid rafts.

1.2 Model Biological Membrane Systems

Due to its complexity and the diversity of protein and lipid molecules present, the cell membrane is impossible to re-create artificially. Model biological membranes that attempt to mimic the structure and function of cell membranes are thus commonly used in experimental investigations; these model membranes can be monolayers, bilayers or multilamellar membranes. Lipid monolayers spread at the air-water interface comprise a single bilayer leaflet and can be studied with microscopy, neutron and X-ray reflectivity and surface-sensitive optical techniques [32]. Multilamellar stacks of bilayers are often used in calorimetry [33] and X-ray and neutron reflectivity studies [34, 35]. In this thesis, we exclusively use model systems based on a single lipid bilayer, either supported on surfaces or in the fluid phase. The single lipid bilayer most closely mimics the native structure of biological membranes and, unlike multilamellar membranes, is appropriate for studying surface-bound protein complexes.

1.2.1 Biomimetic Lipid Bilayer Membranes

We synthesize model lipid bilayer membranes to mimic the structure of cell membranes and to investigate how lipid and protein ordering impacts lipid bilayer membrane fluidity and structure at microscopic and nanoscopic scales. Chapter 2 describes our methods of preparing and characterizing model lipid bilayers.

1.2.1.1 Planar Supported Lipid Bilayers

The supported lipid bilayer (SLB) is a single lipid bilayer deposited onto a solid surface with a thin water layer separating the bilayer and substrate, shown schematically in Figure 1-2. The advantage of using an SLB as a model biological membrane is that the planar surface is convenient for microscopy as well as surface-sensitive techniques including surface plasmon resonance spectroscopy and ellipsometry [36]. If a sufficiently flat and reflective substrate is used, then neutron or X-ray reflectivity is possible [37, 38]. A possible disadvantage of the SLB is that the mobility of the inner leaflet may be affected by its proximity to the surface. In addition, transmembrane proteins and lipids may interact with the substrate [39]. These mechanical coupling effects, however, may also appropriately model cell membranes that are tethered to a cytoskeletal matrix [40].

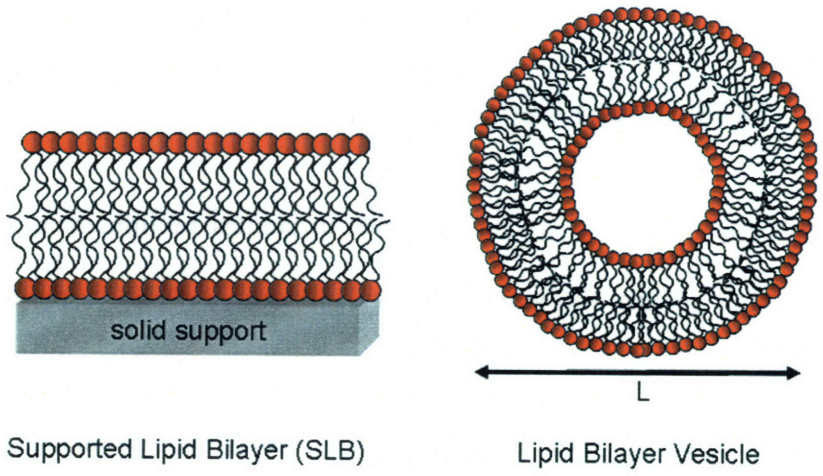

Figure 1-2. Schematic of planar supported lipid bilayer (*left*) and spherical lipid bilayer vesicle (*right*).

1.2.1.2 Lipid Bilayer Vesicles

Unilamellar lipid bilayer vesicles are spherical fluid membranes of a single lipid bilayer, illustrated in Figure 1-2. The length scale L is used to classify the sizes of vesicles: for small unilamellar vesicles (SUVs), L is ~1-50 nm, large unilamellar vesicles (LUVs) have L ~100-500 nm and for giant unilamellar vesicles (GUVs), L is ~1-100 μm. The larger dimension of GUVs is similar to cells; thus GUVs are often used to model cells [41].

1.2.2 Model Systems of Lipid and Protein Ordering

We study two general model systems for lipid and protein ordering: cholesterol-enriched membranes that phase separate into liquid-ordered and liquid-disordered phases and two-dimensional crystalline protein bound to lipid bilayers.

1.2.2.1 Model Lipid Rafts

One of the interesting initial outcomes in studies of lipid phase separation in model membranes is that the simple ternary mixture of DOPC, sphingomyelin and cholesterol demonstrates phase separation behavior very similar to that found in complex mixtures of cell extracts [4]. The chemical structure of these lipids and an illustration of their phase separation are depicted in Figure 1-3. DOPC is a symmetric unsaturated lipid and is enriched in the less-dense liquid-disordered (L_d) phase. The denser and thicker

liquid-ordered (L_o) phase is enriched in sphingomyelin and cholesterol. The packing of the L_o phase may be driven by hydrogen bonding between the cholesterol and saturated phospholipids or sphingomyelin [42] or complexation between sphingomyelin and cholesterol [43].

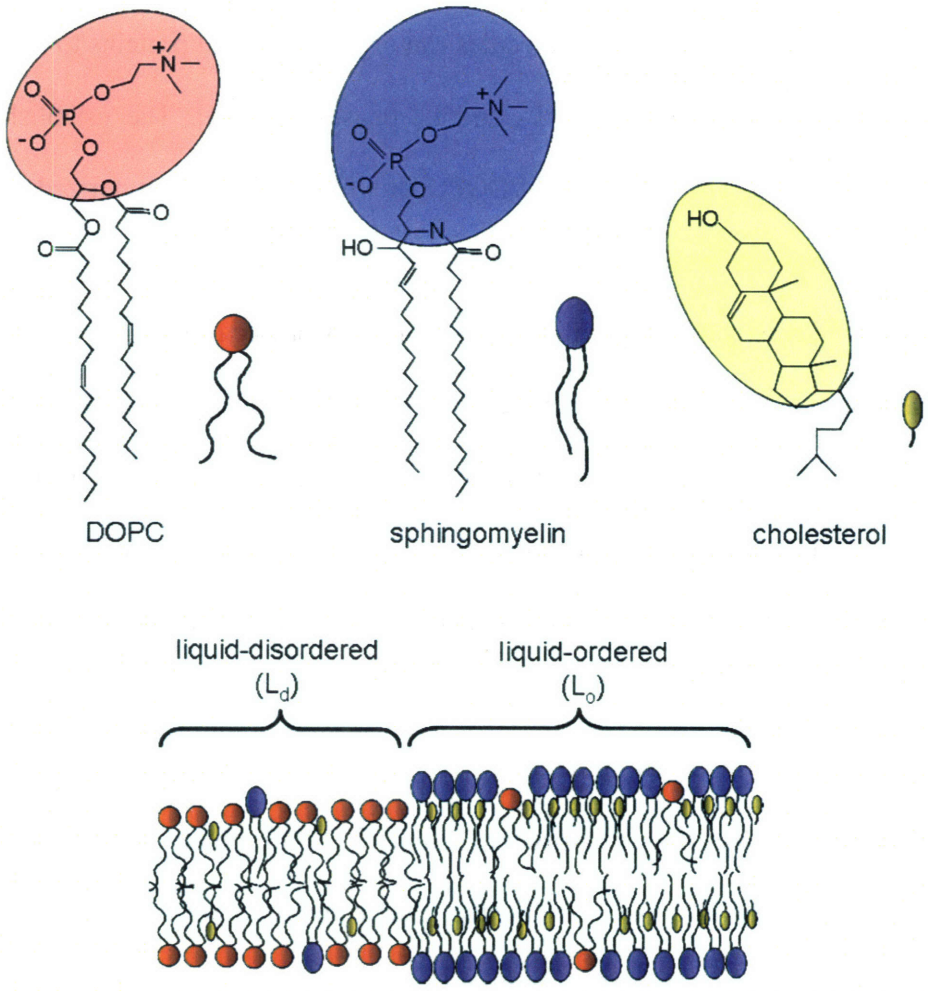

Figure 1-3. Lipid structure and schematic of model lipid rafts in a phase-separated lipid bilayer.

The L_o and L_d phases appear below the lipid mixture's melting temperature T_m; phase diagrams demonstrating how T_m depends on the lipid composition for cholesterol/BSM/DOPC and similar ternary systems further illustrate the ability of lipids to self-organize within a bilayer and to demonstrate complex phase behavior [44, 45]. It has also been suggested that lipid molecules can organize around proteins to modulate the segregation of the membrane into L_o and L_d phases [10, 46]. The established phase diagram behavior of cholesterol/BSM/DOPC provides a well-characterized system for studying how proteins and peptides interact with phase-separating lipid mixtures [47]. In Chapter 3, we investigate the partitioning and phase behavior of cholesterol/DOPC/BSM lipid bilayer membranes containing peptides derived from the scaffolding domain of caveolin-1. We study the scaffolding domain because of its function in attaching caveolin-1 to membranes and interacting with lipid phases in cell membranes [48]. We also develop an assay for measuring how peptides bind and impact the phase diagram of phase-separating lipid mixtures.

While lipid mixtures of cholesterol/BSM/DOPC membranes in fluid vesicles readily phase-separate into microscopic domains, lipid phase separation on solid-supported membranes is more complicated. Stable microscopic lipid domains exist on SLBs [4, 49-51] and the lipids are mobile; however, the domains themselves tend to be immobile [49, 50]. In cell membranes, microscopic domains are not typically observed [52] and lipid rafts are believed to be nanoscopic [53]. In Chapter 6 we study lipid mixtures of cholesterol/BSM/DOPC with X-ray reflectivity and fluorescence microscopy

to measure how lipid compositions change lipid packing, density and fluidity. We also measure membrane thickening and reduced fluidity when the model membrane receptor GM1 (Figure 1-4) is inserted in SLBs. GM1 binds cholera toxin B (CTB) with pentagonal symmetry. The diffusion of GM1 in the membrane and the formation of this complex precedes the entry of CTB into cells to induce disease [16]. GM1 can be localized in cellular caveolae, enabling CTB binding and cholera toxin uptake into the cell through caveolae.

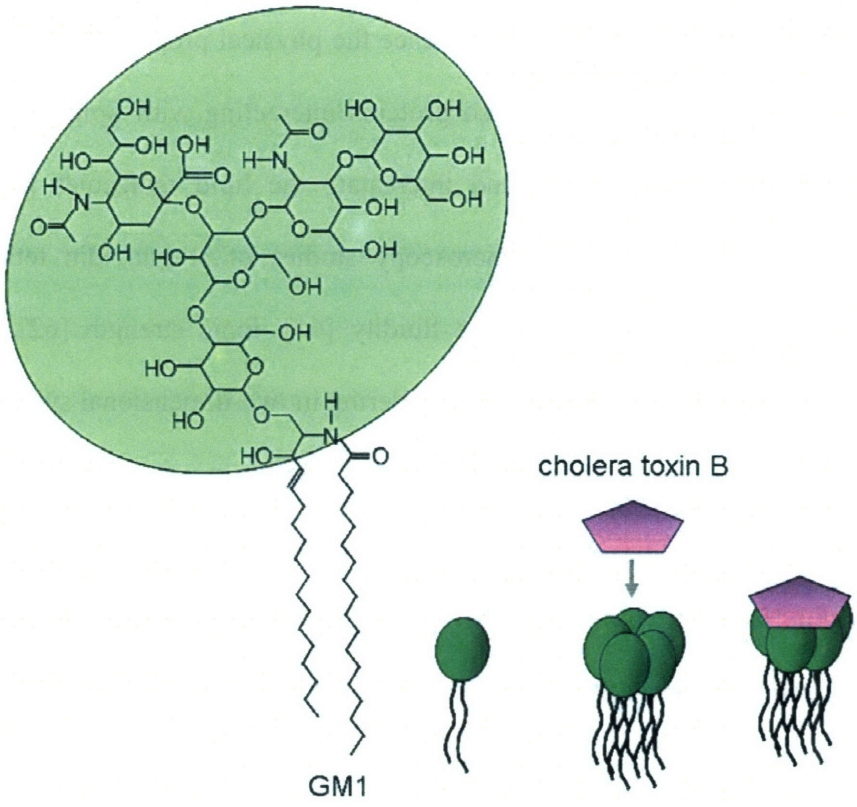

Figure 1-4. Structure of GM1 ganglioside and schematic of GM1 as receptor binding cholera toxin B.

1.2.2.2 Model Ordered Protein Domains

Investigations of protein ordering using model biological membranes gives insight into two-dimensional ordering on a fluid substrate and proteins' influence on the physical properties of lipid membranes. Bacterial surface proteins reconstituted on lipid bilayer vesicles form rigid two-dimensional crystals that deform the membrane into conical and cylindrical shapes [54]. S-layers re-crystallized on vesicles stabilize the membrane against rupture [55]. Similarly, streptavidin crystallized on lipid bilayers deforms and stiffens the membrane [56]. The molecular detail of reflectivity studies can refine mechanisms of how proteins influence the physical properties of the lipid bilayer. Reflectivity experiments with ordered proteins interacting with lipid monolayers show how ordered proteins rearrange and intercalate the lipid molecules [57-60]. At the microscopic scale, fluorescence microscopy studies of streptavidin tethered to lipid membranes illustrates how membrane fluidity [61], ionic strength [62], pH [63] and surface diffusion [64] can impact protein ordering in two-dimensional systems.

We use the streptavidin-avidin model system to investigate two-dimensional protein ordering and its impact on lipid membrane fluidity in GUVs and SLBs. Streptavidin forms two-dimensional crystalline domains when bound to biotin-functionalized lipids incorporated in a stearoyloleoylphosphatidylcholine (SOPC) bilayer. Streptavidin is a tetrameric globular protein that binds biotin in at two sites per side. Avidin is a protein with biotin-binding structure and activity similar to that of streptavidin [65] but does not readily crystallize. Fluorescently-labeled avidin provides a bright background for visualizing streptavidin crystal formation. Figure 1-5 shows the

biotin-functionalized lipid structure and illustrates streptavidin ordering on biotinlyated lipid bilayers.

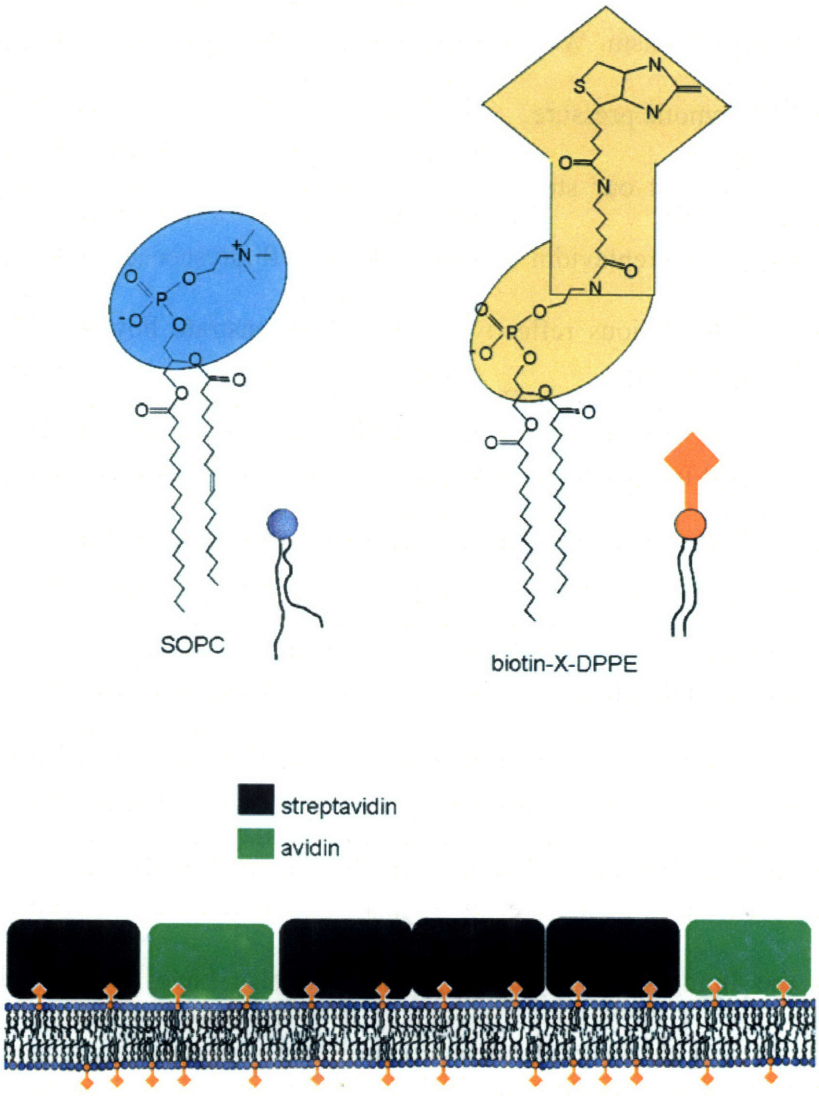

Figure 1-5. Lipid structure and schematic of streptavidin-biotin model system for studying protein ordering. Streptavidin and fluorescently-labeled avidin bind the biotinylated lipids, the streptavidin forms two-dimensional crystals.

Previous studies of streptavidin ordering on GUVs demonstrate that streptavidin-coatings on GUVs stiffen the bilayer and deform vesicles into prolate shapes [56, 62]. In Chapter 4, we explore how protein domains align and deform lipid bilayer vesicles with a size-dependent mechanism. We also demonstrate that crystalline protein confers vesicle stability against osmotic pressure.

To complement our studies of crystalline proteins on GUVs, we also present structural studies of streptavidin bound SLBs with fluorescence microscopy and X-ray reflectivity. While previous reflectivity studies demonstrate how proteins arrange and interact with lipid monolayers [66], the recent ability to characterize single lipid bilayers at the solid support using X-ray reflectivity [38, 67, 68] provides an opportunity to study single protein layers on a single SLB. Studying model peripheral proteins at bilayers offers a more biologically-relevant lipid interface than monolayers. In Chapter 5 we study streptavidin and avidin bound to a single biotinylated SLB with X-ray reflectivity. Fluorescence microscopy characterization of the samples provides direct evidence of crystal formation and allows us to quantify the lipid bilayer fluidity.

In addition to their role in fundamental studies for elucidating biological processes, the lipid bilayer systems we present also have potential applications in biosensing and drug delivery. Ordered proteins on membranes have potential application in biosensing, where a template of functionalized proteins can be immobilized on vesicles [55] or on planar bilayers. Stable SLBs at the solid interface have potential lab-on-a-chip applications, where a single membrane directly coupled to a surface can be used for detection and measurement of molecular binding events [69].

1.3 Thesis Overview

We describe our preparation and characterization of these different model biological membrane systems, both vesicles at supported bilayers, in Chapter 2. The subsequent chapters describe our investigations of protein and lipid ordering in different model system. The first model biological membrane system that we present is caveolin-1 peptides interacting with ordered lipid phases in fluid vesicles. We determine the phase partitioning behavior and lipid phase diagram of caveolin-1 peptides in bilayer vesicles in Chapter 3. We continue studies of lipid bilayer vesicles in Chapter 4, where we examine how streptavidin influences vesicle shape and stability by ordering and self-arrangement. Streptavidin ordering on lipid bilayers is presented in more structural detail in Chapter 5, where we use X-ray reflectivity to study the structure of supported lipid bilayers coated with a protein layer comprising streptavidin and avidin. We then use reflectivity to examine the influence the membrane receptor GM1 and its influence on lipid and membrane structure in Chapter 6, and we present our reflectivity investigation of the structure of cholesterol-enriched lipid membranes.

CHAPTER 2. EXPERIMENTAL METHODS

2.1 Preparation of Biomimetic Membranes

All lipid solutions for experiments are prepared in high performance liquid chromatography-grade (HPLC) chloroform. Solutions are transferred only with glass pipettes and stored in teflon-sealed sterile glass containers.

2.1.1 Electroformation of GUVs

Giant unilamellar vesicles (GUVs) are spherical lipid bilayers that are 1-100 μm in diameter. GUVs can be visualized by optical microscopy and they are used to model cellular membranes, because they are a size comparable to that of cells [70]. The electroformation method for synthesizing giant unilamellar vesicles (GUVs) produces a high yield of GUVs [71, 72]. As depicted schematically in Figure 2-1, a dry lipid film on a conductive substrate is hydrated in aqueous solution; upon application of a gentle AC field, large bilayers swell from the film to form GUVs.

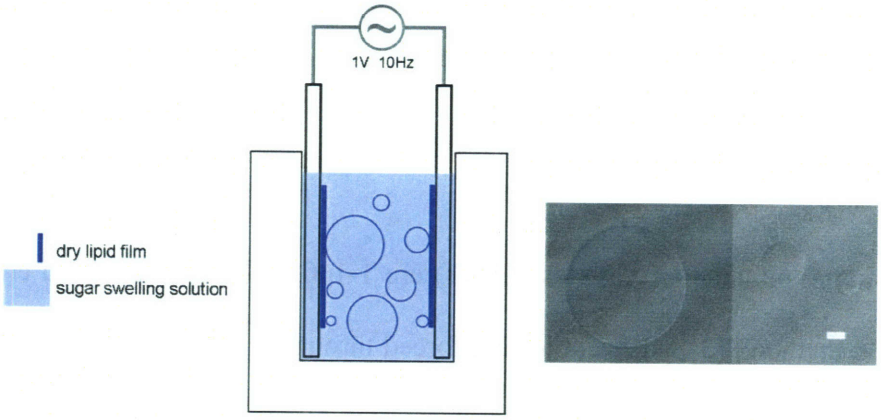

Figure 2-1. Schematic of GUV electroformation (*left*) and difference interference contrast micrographs of GUVs (*right*). 10 μm scale bar.

We use electroformation for the preparation of GUVs. Indium tin oxide- (ITO) coated substrates purchased from Präzisions Glas and Optik GmbH (Iserlohn, Germany) are rinsed with detergent and sonicated 30 min in deionized (DI) water. Approximately 40 μL of lipids in chloroform at a concentration of 5 mg/mL are spread on the ITO plates; the lipid film is dried 2 h in a vacuum chamber. The dried plates are placed parallel 5 mm apart in a Teflon holder filled with swelling solution and connected to a function generator with 1 V AC, 10 Hz signal (Figure 2-1). The AC signal is applied 1.5-2.5 h to form GUVs. To provide density and optical contrast and allow for osmotic stressing, we form the GUVs is a sugar solution. For upright microscopy, GUVs are filled with glucose then re-suspended in sucrose; the GUVs then float to the top of the viewing cell. Similarly, sucrose-filled GUVs are used for inverted microscopy experiments. We place the vesicles in chambers created from CoverWell silicone gaskets purchased from Grace

Bio-Labs (Bend, OR) sealed to coverslips. All surfaces are soaked for 30 min in 1 mg/mL bovine serum albumin solution to prevent GUVs from adhering to surfaces.

2.1.2 Extrusion of LUVs

Large unilamellar vesicles (LUVs) are 1-100 nm in diameter and created by the extrusion method [73], where lipids are forced through uniform pores of a polycarbonate filter, resulting in LUVs with monodisperse size distributions. LUVs can be spread on substrates to form supported lipid bilayers (SLBs) by the vesicle fusion method [74, 75].

Lipids in chloroform are placed in a clean glass vial and initially dried with N_2 then completely dried for 8 h in a vacuum chamber. The dried lipid film is hydrated in an aqueous solution for a final lipid concentration of 1 mg/mL then agitated on a vortex mixer to completely hydrate the film; this suspension is heated to 40 °C for 1 h. The lipid suspension is then passed through a 100-nm polycarbonate filter 10 times using the Avanti Mini-Extruder from Avanti Polar Lipids (Alabaster, AL). Extruded LUVs are discarded after 5 days.

2.1.3 SLB Preparation

Supported lipid bilayers (SLBs) are prepared by vesicle fusion, where LUVs adsorb and rupture on substrates, or by spin-coating of lipids from organic solution directly onto substrates followed by hydration.

All supported lipid bilayers (SLBs) are prepared on silicon substrates 20 × 15 mm^2 in size and 675 μm thick cut from polished 6" silicon wafers with a 100-nm thick thermal oxide layer. The substrates are cleaned by sonication for 10 min in isopropanol followed by rinsing with DI water then a three-stage chemical cleaning treatment. First, the substrates are boiled in acetone for 10 min at 100°C, then in a mixture of 1:1:5 $H_2O_2/HCl/H_2O$ by volume for 15 min at 150°C, then in 1:1:5 $H_2O_2/NH_4OH/H_2O$ for 15 min at 150°C. After each step, the substrates are rinsed with DI water. The substrates are stored in DI water until the SLB formation procedure.

Microfluidic chambers, shown schematically in Figure 2-2, are used for solution exchange and the formation of protein layers on SLBs and also serve as our platform for microscopy and X-ray measurements [37, 67]. Plastic chambers with two reservoirs connected by a channel of dimensions 5 × 0.4 × 50 mm are purchased from ibidi GmbH (München, Germany). The chambers are cleaned before use with isopropanol. An area of 20 × 15 mm^2 is milled into the center of the channel for embedding the SiO_2 substrates. The microchannel minimizes the amount of reagents required and the fluid reservoirs ensure constant hydration of the SLBs, as hydrated SLBs are destroyed if air bubbles enter the chamber and contact the surfaces.

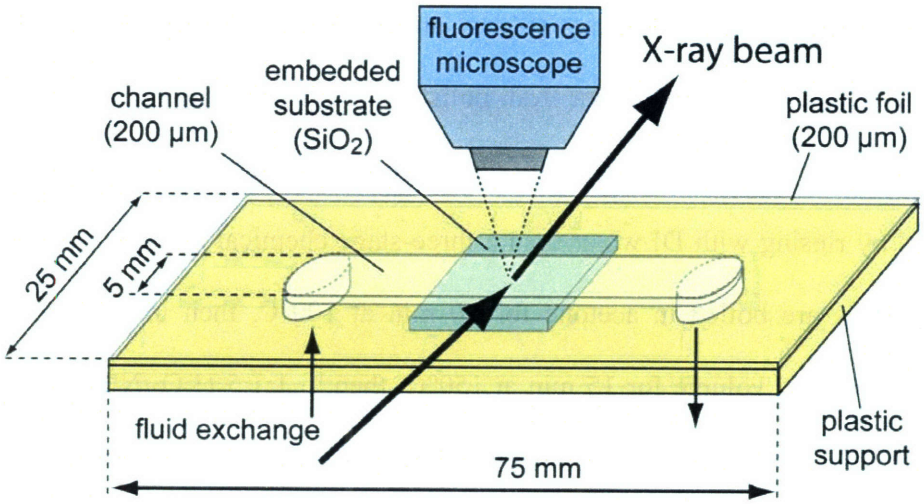

Figure 2-2. Schematic of microfluidic chamber used to prepare and study SLBs. The SLB on the SiO_2 substrate is measured with reflectivity and visualized with fluorescence microscopy.

2.1.3.1 Vesicle Fusion

The vesicle fusion method is used to spread LUVs onto substrates to form homogeneous lipid bilayers [74-76]. Clean substrates are first secured in microfluidic chambers using two-component UHU epoxy glue that hardens in 5 min (Bühl, Germany). After the allowing the epoxy glue to pre-dry for 30 min, the chambers with glued-in substrates are placed under vacuum for 6 h for final hardening.

We use osmotic concentration gradients to assist in the rupture of the LUVs to form SLBs, as illustrated in Figure 2-3. LUVs are extruded in solutions with modified HEPES buffer (10mM HEPES, 100mM NaCl, 2mM $MgCl_2$, 2 mM $CaCl_2$, pH 7.4). The

microfluidic chamber is then filled with this buffer and ~200 μL of LUV solution are pipetted into the channel and left undisturbed 30 min to allow LUVs to adsorb to substrate. The substrate is then rinsed with DI water, causing the LUVs to rupture under osmotic stress to form the lipid bilayer. The layer is heated to 35-40 °C for at least 2 h to anneal the membrane.

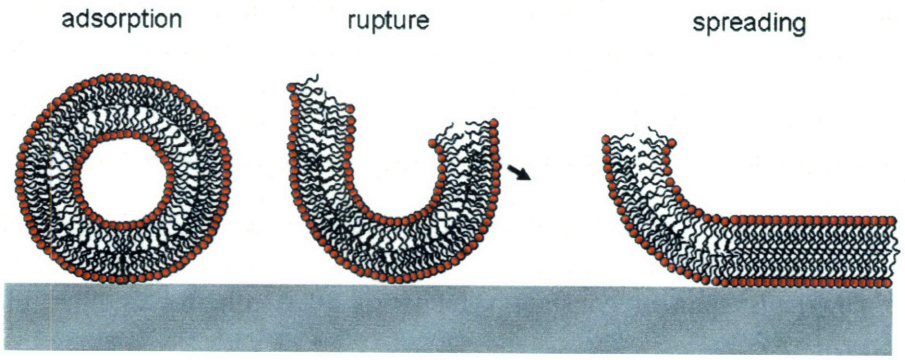

Figure 2-3. Schematic of vesicle fusion illustrating adsorption of LUVs on surface (*left*), rupture from osmotic stress (*middle*), and spreading to form SLB (*right*).

2.1.3.2 Spin-coating

We are not able to reproducibly produce homogeneous and fluid lipid bilayers with the vesicle fusion method for lipid mixtures containing the ganglioside GM1 or biotin-functionalized lipids. For these molecules, we use the alternative preparation

procedure of spin-coating of lipids from organic solution [77, 78] to prepare single SLBs on our substrates. We prepare 3 mg total lipid in chloroform in clean glass vials; the chloroform is then evaporated from each vial in a nitrogen stream followed by evacuation in a vacuum chamber for at least 12 h. Dried lipids are then re-dissolved in isopropanol to a final concentration of 1.5 mg/mL. This concentration ensures the formation of a complete single bilayer [77]. Unlike chloroform, isopropanol completely wets the hydrophilic silicon substrates.

To coat the substrates, 200 μL of lipid solution is dropped onto a clean silicon substrate in a Delta 10 spin-coater from BLE Lab Equipment (Radolfzell, Germany). The substrate is immediately accelerated with the following profile: a ramp from 0 to 2000 rpm is driven for 2 s, followed by another ramp from 2000 to 3000 rpm for 2 s. Then the sample is spun at constant velocity of 3000 rpm for another 118 s. The substrates are then placed in a vacuum chamber for at least 4 h to ensure complete evaporation of the isopropanol. Dried spin-coated substrates are then glued into microfluidic chambers with two-component UHU epoxy glue and dried in air for 30 min, then in vacuum for 6 h. The SLBs are hydrated by flushing the microfluidic chambers several times with DI water to ensure that excess lipids are flushed away.

2.2 Microscopy

2.2.1 Differential Interference Contrast Microscopy

In order to study the shapes of GUV samples that do not have fluorescent contrast, we use differential interference contrast (DIC) microscopy. We obtain DIC images of GUVs using a Cooke SensiCam digital camera (Cooke Corporation, Romulus, MI) and a Zeiss Axioplan fluorescence microscope with 40× and 100× objectives (Oberkochen, Germany). We form GUVs in glucose solutions and dilute them in sucrose to provide optical and density contrast. DIC micrographs are analyzed using ImageJ software (NIH, Bethesda, MD).

2.2.2 Fluorescence Microscopy

Fluorescently-labeled lipids, proteins and peptides in our lipid bilayers are visualized with fluorescence microscopy. The lipid Texas Red 1,2-dihexadecanoyl-*sn*-glycero-3-phosphoethanolamine, triethylammonium salt (TR-DPPE) from Invitrogen (Carlsbad, CA) provides constrast for fluorescence microscopy. TR-DPPE is relatively photostable and identifies phase-separation by selectively partitioning into less-dense or liquid-disordered phases [79]. For visualizing peptide and proteins structures in lipid bilayers, we require dyes of a different color. Alexa Fluor 488 conjugate (Alexa488-

avidin) from Invitrogen provides fluorescent contrast to visualize protein ordering. We use FITC-labeled peptides to study peptide partitioning into lipid phases.

2.2.2.1 Lipid Phase Diagrams

To determine the lipid phase diagram of GUVs made from phase-separating lipid mixtures, we observe miscibility transitions with fluorescence microscopy and a heating stage [44, 45, 79]. Phase separation and domain morphology on the surface of the GUVs are visualized using a Nikon Diaphot inverted microscope with 100× objective equipped with a microscope heating stage unit (Instec, Boulder, CO) and an objective collar heater (Bioptechs, Butler, PA). We measure the sample chamber temperature with a thermocouple (Omega, Stamford, CT). The miscibility transition temperatures are measured by both heating and cooling. We calculate the fractional area of the GUV surface occupied by fluorescently-labeled phases using ImageJ software. Images are thresholded to distinguish bright and non-fluorescently-labeled phases. As described elsewhere [80], the geometry of the system prevents the use of automated algorithms for calculating the relative fractional areas of each phase, as the threshold level must be adjusted individually for each GUV. We therefore analyze at least 20 different GUV surfaces are analyzed to determine the average fractional area of phases at each composition.

2.2.2.2 Continuous Bleaching

We use the continuous bleaching method to measure the fluidity of SLBs with a standard fluorescence microscope setup [67, 81]. We visualize and characterize SLBs in microfluidic chambers with a portable Zeiss Axiotech vario fluorescence microscope (Oberkochen, Germany) equipped with 10× (NA 0.3) and long distance 63× (NA 0.75) Plan-Neofluar objectives. Images are captured with an ORCA C4742-95 CCD camera and WASABI imaging software from Hamamatsu Photonics (Tutzing, Germany). ImageJ software is used to determine the fractional area coverage of crystalline protein and to estimate protein domain size. We align a HBO 103 Hg lamp from Zeiss to ensure even illumination of the sample. Continuous bleaching data are analyzed with MATLAB software from Mathworks (Cambridge, MA). The theory of continuous bleaching and data analysis are explained in detail in Chapter 5.

2.2.3 Fluorescence Confocal Microscopy

In order visualize lipid phase separation and protein ordering on GUVs in three-dimensions, we use confocal fluorescence microscopy. All fluorescence confocal microscopy experiments are performed at the W.M. Keck Microscopy Facility at the Whitehead Institute with a Zeiss laser scanning module (LSM) microscope with a Zeiss C-Apochromat 40× water immersion objective with numerical aperture (NA) of 1.2. For two-channel experiments, the excitation light from lasers at 488 nm and 543 nm is

reflected by a dichroic mirror (HFT 488/543) and the emission is split by another dichroic mirror (NFT 490) into two channels and passed through a 505-719 emission filter in the first channel and a 558-719 emission filter in the second channel to detect the green-labeled species and TR-DPPE, respectively. For the one-channel experiments of FITC-labeled peptides, we use a 488-nm laser and a LP 505 filter. For three-dimensional image projections of vesicles, *z*-scans are taken in 0.45-μm increments and projected using Zeiss LSM software.

2.3 Fluorescence Correlation Spectroscopy

Fluorescence correlation spectroscopy (FCS) is the time-correlated measurement of the fluctuation of fluorescence intensity in an illuminated volume. FCS is employed to measure the diffusion constants of lipids and proteins in biological membranes [82, 83]. We use FCS to measure the binding of a fluorescently-labeled peptide to LUVs in solution [84]. As depicted in Figure 2-4, *left*, the peptide freely diffuses in an illuminated volume with a characteristic diffusion time, $\tau_{D,peptide}$ and, when bound to a large LUV, the peptide diffuses with the characteristic diffusion time of the LUV, $\tau_{D,LUV}$. Analysis of the autocorrelated fluorescence intensity indicates the relative amounts of peptide diffusing free in solution and bound to LUVs (Figure 2-4, *right*).

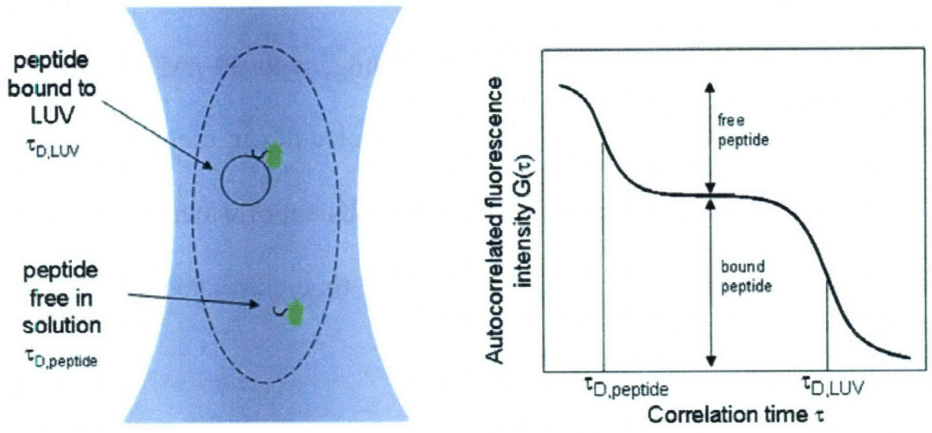

Figure 2-4. Schematic adapted from [84] of the FCS measurement of peptide binding to LUVs in solution (*left*) and a two-component autocorrelation function (*right*).

We measure the characteristic diffusion times of the free peptide and the LUVs in separate experiments using a Zeiss ConfoCor2 instrument with 40× Apochromat water-immersion objective. In order to prevent adhesion of the LUVs to surfaces, we treat Lab-Tek chamber slides by filling them with 1 mg/mL bovine serum albumin dissolved in water for at least 30 min then air-drying the chambers before filling them with our FCS samples. The incident laser power is 160 μW for all experiments; we verify that photobleaching does not affect the measurements by measuring control samples at 480 μW laser power. A sugar buffer solution of 100 mM glucose with 5 mM KCl is used for all FCS measurements and calibrations. The focus volume is calibrated with Rhodamine 6G for experiments at 488 nm and with Cy5 at 633 nm. To adjust the pinhole, the time-correlated fluorescence intensity spectra for 100 nM fluorescent dye in solution is

measured. After pinhole adjustment, the volume of the focus is determined by measuring 10 consecutive correlation spectra, each 30 s long, with 30 nM solution of calibration dye. The known dye concentration, fraction of molecules in the triplet state T and triplet time τ_{Tr} of the calibration dye and the diffusion constant of water D are used to determine the dimensions of the focus volume from the time-correlated fluorescence intensity measurement from the equation [84]:

$$G(\tau) = \frac{1}{N} \times g(\tau) = \frac{1}{N} \times \left(1 + \frac{T}{1-T} e^{-\tau/\tau_{Tr}}\right)\left(\frac{1}{1+\tau/\tau_D}\right)\left(\frac{1}{1+\tau/S^2\tau_D}\right)^{\frac{1}{2}} \qquad (2\text{-}1).$$

The number of particles in the focus volume is N, the correlation time of the dye is $\tau_D = \omega^2/4D$, where ω is the radius of the focus volume and S is ratio of the radial and axial distances from the center of the laser focus beam. We fix the structural parameter in Equation 2-1 with the value measured from our calibration; since our experiments involve LUVs, which we expect to have a longer diffusion time than free dyes in solution, we measure all samples with LUVs for at least 60 s. Diffusion times for LUVs at each lipid composition are determined by measuring LUVs containing 0.01 mol % of the lipophilic fluorescent dye 1,1'-dioctadecyl-3,3,3',3'-tetramethylindodicarbocyanine,4-chlorobenzensulfonate salt (DiD, Invitrogen) at 633 nm excitation. To use FCS to quantify the binding of fluorescent peptides to LUVs, the peptide concentration should be proportional to the number of particles detected in the focus volume, N. Measurement of N over a range of peptide concentrations, as shown in

Figure 2-5, indicates peptide solubility as monomolecular units and characterizes the signal/noise ratio to determine the appropriate linear measurement regime. In our experiments of soluble peptide binding to LUVs presented in Chapter 3, characterization of this linear detection range (Figure 2-5, *red line*) motivated our choice of peptide concentration of 50 nM to study binding to LUVs.

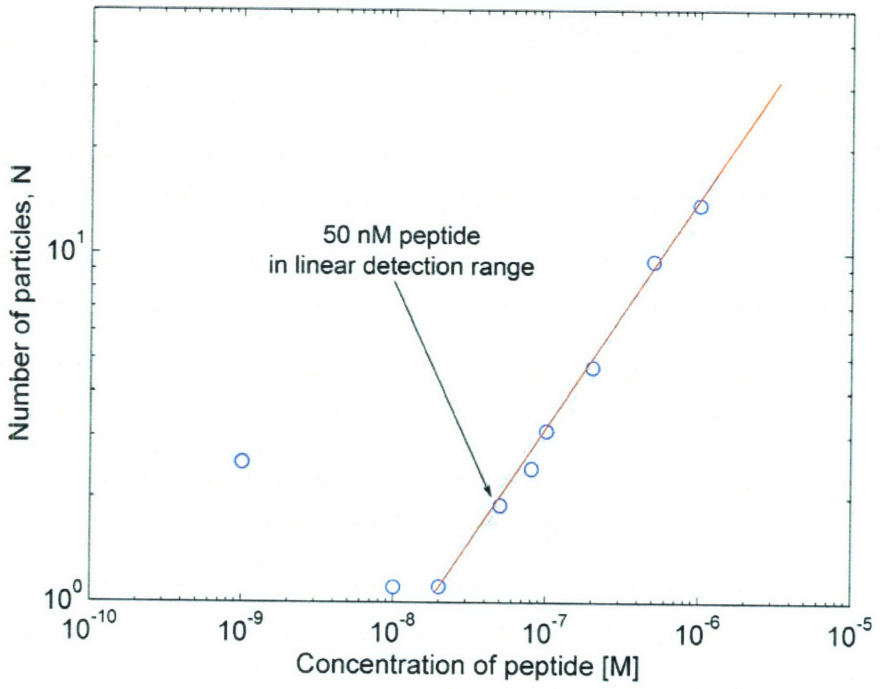

Figure 2-5. The number of particles in the FCS volume plotted as a function of concentration of peptide to indicate measurement range appropriate for quantitative determination of peptide binding.

2.4 X-ray Reflectivity

X-ray reflectivity measurements are performed at the undulator beamline ID1 at the European Synchrotron Radiation Facility (ESRF) in Grenoble, France. Sample chambers are mounted in a horizontal scattering geometry with a vertical plane of incidence; the X-ray beam geometry is shown in Figure 2-6; a top view of the microfluidic chamber is shown in Figure 2-2. We identify the interface and the center of rotation of the substrate for each sample before measurement. For reflectivity studies of SLBs on SiO_2, we choose an X-ray energy of 19.9 keV (λ = 0.623 Å) for the grazing-incidence beam.

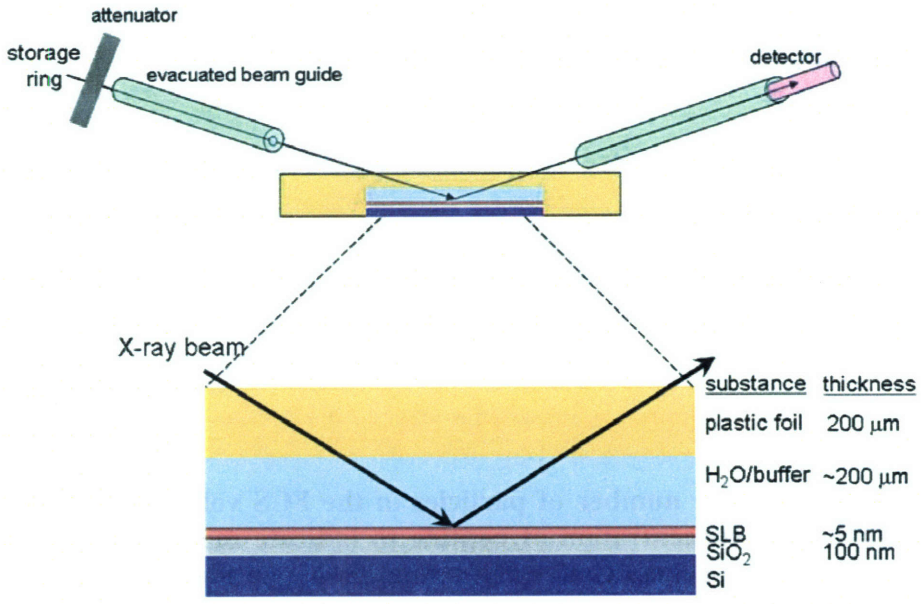

Figure 2-6. X-ray reflectivity geometry used to study a SLB interface in a microfluidic channel.

The beam cross section is limited by a pre-sample aperture of 200 × 1000 μm^2 (vertical × horizontal). The relatively large beam size ensures a wide illumination of the surface area even at higher grazing incidence angles. Evacuated beam guides with Kapton windows (Figure 2-6) positioned in close proximity to the sample chamber minimize air scattering. The reflected intensity is collected with a NaI point detector. The loss of X-ray beam intensity by transmission through the chamber is less than an order of magnitude and the small vertical post-sample aperture completely suppresses parasitic contributions due to reflectivity from the top plastic foil of the sample chamber [37].

We take different measures to minimize X-ray beam damage; at full beam intensity, beam damage is apparent and results in reduced surface coverage of the membranes [37]. These data also provide a basis to compare to reflectivity scans to identify possible beam damage qualitatively. To minimize damage, we position automatic attenuators in front of the chambers to reduce the beam intensity (Figure 2-6). Each reflectivity scan is also performed on a fresh spot and an automatic shutter prevents exposure to X-rays during motor movements.

The reflectivity data are analyzed using Parratt's method [85] and presented with Fresnel normalization: the reflectivity is divided by the Fresnel reflectivity (R_F), where

$$R_F = \left| \left(1 - \sqrt{1 - (q_c / q_z)^2}\right) \Big/ \left(1 + \sqrt{1 - (q_c / q_z)^2}\right) \right|^2 \qquad (2\text{-}2).$$

The momentum transfer at the critical angle of total external reflection is q_c and q_z is the momentum transfer perpendicular to the interface. To fit our measured reflectivity we

model the bilayers as a stack of slabs with varying thickness (z) and density (ρ), positioned between water and the SiO_2 substrate. The thickness and number of slabs appropriate for modeling varies with the different protein and lipid mixtures; the different slab models used to fit the data from our SLBs are described in Chapters 5 and 6. For a homogeneous single supported lipid bilayer, we use 7 slabs: each leaflet has 2 slabs representing the headgroup and another slab for the acyl chain region; the interleaflet space is an additional slab. Using the software Parratt32 (Hahn Meitner Institute), we fit our reflectivity data to determine the electron density profile, $\rho(z)$, for our specified number of slabs. An example of the 7 slabs used to represent a SLB of SOPC is shown in Figure 2-7. To model the electron density profile to N slabs, we use the following equation:

$$\rho(z) = \sum_{i=1}^{N} \frac{\rho_i - \rho_{i+1}}{2}\left(1 + erf\left(\frac{z - z_i}{\sqrt{2}\sigma}\right)\right) \qquad (2\text{-}3).$$

The slab profiles are smoothed by an overall roughness, σ. For our substrates, we use σ = 3 Å. The electron density profile for our 7 slab model fit to SOPC is shown in Figure 2-7 (*blue curve*).

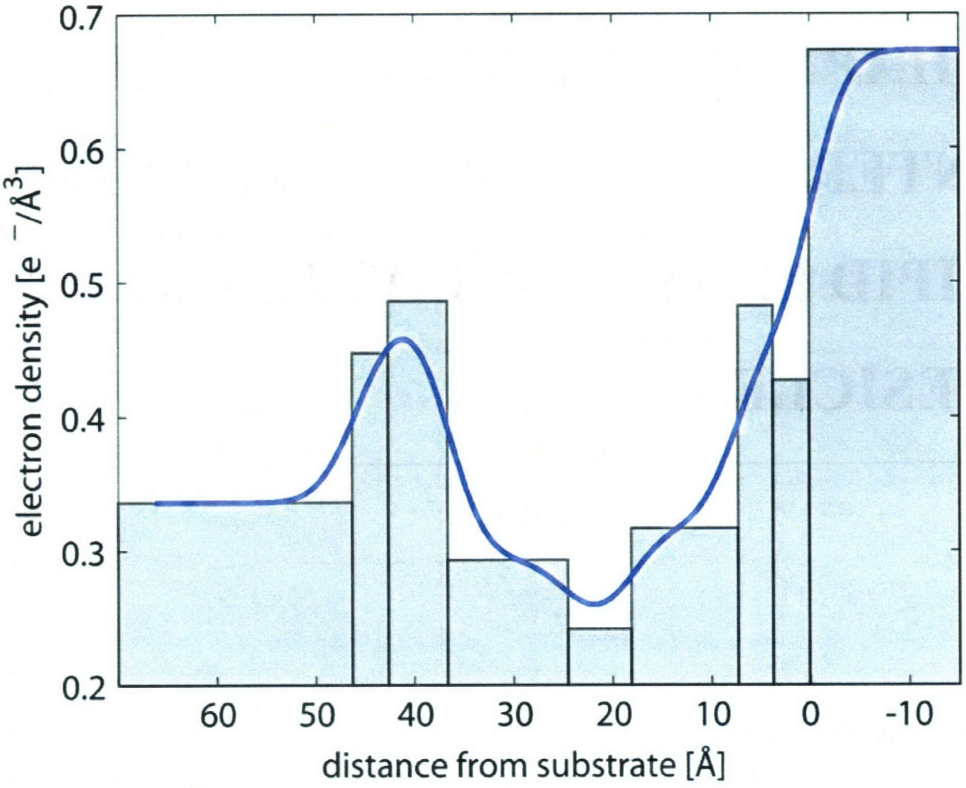

Figure 2-7. Electron density profile of SOPC (*blue curve*) and the corresponding 7 slabs between the water and SiO_2 used to model the lipid bilayer. Each slab has density ρ_i, and thickness z_i and the electron density profile $\rho(z)$ is smoothed with surface roughness $\sigma = 3$ Å.

CHAPTER 3. MODEL PEPTIDE INTERACTIONS WITH ORDERED LIPID PHASES IN LIPID BILAYER VESICLES

3.1 Introduction

Lipid rafts, or detergent-insoluble domains of the plasma membrane enriched in cholesterol and sphingolipids, are thought to play a role in sequestering various molecules to facilitate cell signaling. Caveolae are a specialized type of lipid raft with flask-like invaginated morphology enriched in the protein caveolin-1 that participate in cell signaling and lipid metabolism [11-15]. Caveolin-1 has been shown to bind cholesterol [86] and associate with sphingolipids [87] and may have a structural role in the formation of caveolae [29, 88].

Model lipid rafts in synthetic lipid bilayers have provided a basis for understanding cholesterol-enriched phases of the plasma membrane. Lipids extracted from cell membranes and reconstituted in giant unilamellar vesicles (GUVs) exhibit microscopic phase coexistence with lipid domains resembling ternary lipid mixtures of

cholesterol, phosphatidylcholine and sphingomyelin [4]. In this widely-studied model system, liquid-ordered (L_o) domains are formed from the packing among saturated lipid acyl chains and cholesterol and are immiscible with liquid-disordered (L_d) domains enriched in phosphatidylcholine [45]. These L_o lipid domains are considered models of lipid rafts in the plasma membrane. Various physical properties of model lipid rafts, including composition, morphology and molecular mobility have been studied [45, 83]. There has also been an increasing effort to understand how proteins partition into either the L_o phase or L_d phase [47]. What remains to be well-studied, however, is how peptides and proteins influence the lipid phase behavior of these model lipid rafts.

Proteins are significant part of the composition of cell membranes and it is therefore important to consider proteins in model studies of lipid rafts and caveolae. Studying the interplay between proteins and lipid phase separation may give insight into the formation of lipid rafts, as proteins have been suggested promote domain formation by associating with certain lipids [89]. It has also been suggested that lipid molecules can organize around proteins and modulate phase separation [10, 46]. Using model lipid membranes, researchers have studied how proteins and peptides can cause lateral redistribution of lipids in bilayer membranes using differential scanning calorimetry (DSC) [89] and fluorescence microscopy [17]. An advantage of fluorescence microscopy is that it allows one to directly observe the lipid phase partitioning of labeled molecules as well as microscopic phase separation.

In this study we investigate the partitioning and phase behavior of lipid bilayer membranes containing caveolin-1. We selected caveolin-1 because caveolae are enriched

in the lipid raft components cholesterol and sphingomyelin and the membrane interaction of caveolin-1 is not well understood. Mutagenesis experiments have identified the caveolin scaffolding domain (CSD) as the region of caveolin-1 responsible for membrane binding and targeting the full-length protein to caveolae [48]. The CSD comprises amino acids 82-101 of the N terminal domain of caveolin-1 and has been shown to associate with detergent-insoluble membrane fractions assayed *in vivo* [90]. We have selected model peptides derived from the CSD of caveolin-1 to study phase separation and the influence of cholesterol concentration on peptide-lipid interactions in lipid bilayers.

In previous model membrane experiments, the full-length CSD formed cholesterol-enriched domains in model membranes composed of DOPC, the acidic lipids phosphatidylserine and phosphatidylinositol-4,5-biphosphate (PIP_2), and cholesterol [91]. Subregions of the CSD and their membrane interactions have also been previously investigated. In live-cell mutagenesis experiments, KYWFYR was shown to be the membrane-attachment sequence [90] of caveolin-1 and in recent model membrane experiments, authors have demonstrated using DSC that KYWFYR does not promote local high cholesterol concentrations nor does it bind cholesterol in phosphatidylcholine membranes [33]. DSC analysis has been used to study the peptide *N*-acetyl-VTKYWFYR amide, which was shown to promote local cholesterol crystal formation and depletion from other domains, though this effect was more pronounced with the full-length CSD [92]. The effect of acidic lipids [91, 93] and cholesterol [91, 92] on the spatial organization and binding of CSD peptides has been investigated; thus, our primary goal is to study caveolin-1 in model membranes with defined L_o and L_d domains and to

investigate how the CSD can impact the phase behavior of L_o and L_d phases. Sphingomyelin is a component of caveolae *in vivo* [87] and thus we focus on a membrane containing sphingomyelin in order to understand caveolin and lipid interactions.

3.2 Materials and Methods

1,2-Dioleoyl-*sn*-glycero-3-phosphocholine (DOPC), cholesterol and brain sphingomyelin (BSM) are purchased from Avanti Polar Lipids, TR-DPPE and DiD from Invitrogen. Rhodamine 6G and Cy5 dyes in sugar solutions (Merck, Darmstadt, Germany are used for FCS system calibration. Lipids are dissolved in HPLC-grade chloroform and methanol from either Fluka (Switzerland) or Mallinckrodt (Phillipsburg, NJ). All other chemicals used are reagent grade. We purchase fluorescently-labeled synthetic peptides containing sequences derived from the caveolin scaffolding domain (CSD) from SynPep (Dublin, CA) and the MIT Biopolymers Laboratory. The CSD is peptide labeled at the N terminus with fluorescein isothiocyanate is FITC-CGIWKASFTTFTVTKYWFYR-acetyl (CAV-CSD). A shorter fluorescently-labeled peptide containing the membrane-attachment segment amino acid sequence residues 89-101 is FITC-FTTFTVTKYWFYR-acetyl (CAV-INSOL). The soluble peptide containing these residues is synthesized with an FITC label at the N-terminus and the sequence SGS between the FITC and CSD residues to improve peptide water solubility without adding net charge resulting in a final peptide structure of FITC-SGSFTTFTVTKYWFYR-acetyl (CAV-SOL). All peptides are

purified using HPLC. The pI's of the three peptides were estimated to be in the range 9.5–10.5 [94]. The structures of the three peptides are shown schematically in Figure 3-1.

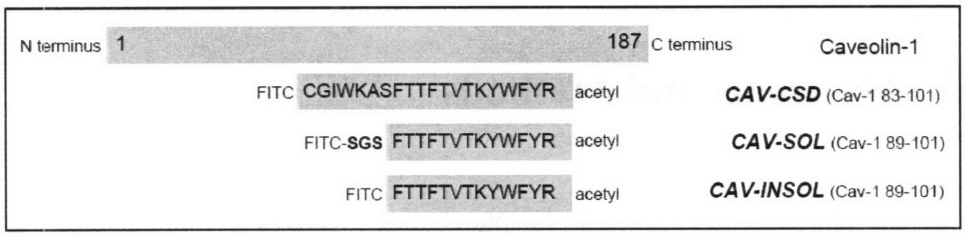

Figure 3-1. Schematic of fluorescently-labeled synthetic peptides.

We prepare giant unilamellar vesicles (GUVs) with the electroformation technique [95] described in Chapter 2. Approximately 40 μL of lipid solution is spread onto conductive indium tin oxide plates and dried under vacuum. To this lipid mixture, we add 1 mol % of the water-insoluble caveolin-1 peptides CAV-CSD or CAV-INSOL. We visualize the lipid phases by adding 0.1 mol % of TR-DPPE to the lipid mixture. The GUVs are grown in a 100 mM sucrose and 5 mM KCl solution for 1.5–2 h at a temperature above the lipid miscibility transition temperature. We form large unilamellar vesicles (LUVs) using the extrusion technique [73] and dried lipids are then rehydrated in 100 mM glucose and 5 mM KCl. This solution is passed 10 times through two 100-nm polycarbonate filters using the Avanti Mini-Extruder.

To determine the lipid phase diagram, miscibility transitions are observed using fluorescence microscopy [44], as described in Chapter 2. The stock GUV solution is

diluted approximately twofold with 100 mM glucose and 5 mM KCl, to provide density contrast. Sample heating over a temperature range of 10°C-50°C is accomplished by our microscope heating stage unit. The miscibility transition temperatures are measured both by heating and cooling and the error bars represent the range over which phase miscibility was observed. In order to observe the impact of the water soluble CAV-SOL peptide on microscopic phase separation, the soluble peptide is dissolved in glucose buffer and added to GUVs in solution. The fractional area of the GUV surface occupied by the DOPC-enriched liquid phase is calculated using ImageJ software.

3.3 Fluorescence Correlation Spectroscopy

Recently, fluorescence correlation spectroscopy (FCS) has been used to measure the binding between large unilamellar vesicles (LUVs) and water-soluble peptides in nanomolar concentrations [84]. We employ this FCS peptide-membrane assay to measure the binding of fluorescently-labeled water-soluble CAV-SOL peptide to LUVs with only slight modifications. Attaching the water-soluble FITC peptide to the end of the caveolin scaffolding domain peptide away from the membrane attachment sequence should minimize the influence of the fluorophore on the peptide-membrane binding. As a control experiment, we verifiy that the binding of free FITC to membranes is negligible for the lipid compositions used. The calculation of molar partition coefficients from FCS data is outlined [84]. The expression for the normalized time correlation function $G(\tau)$ is in reference [96]:

$$G(\tau) = \frac{1}{N} \times g(\tau) = \frac{1}{N} \times \left(1 + \frac{T}{1-T} e^{-\tau/\tau_{Tr}}\right)\left(\frac{1}{1+\tau/\tau_D}\right)\left(\frac{1}{1+\tau/S^2\tau_D}\right)^{\frac{1}{2}} \qquad (3\text{-}1).$$

The average number of fluorescent molecules counted in the laser focus is N and τ_D is the diffusion time of the molecules. The fraction of fluorophores in the triplet state is T, the triplet lifetime is τ_{Tr} and the structural parameter, S, is the ratio of the radial to axial distances of the center of the laser beam to the edge of the focus volume. The triplet fraction of the FITC-labeled peptide is ~0.7 and the triplet lifetime is ~3.5 μs. From Rhodamine 6G calibration measurements, we determine S=5.5.

In our experiments, both bound and free peptide diffuse within the laser focus volume, so the autocorrelation function is described as a weighted sum of the contributions from the CAV-SOL peptide in solution (P) and the CAV-SOL peptide bound to LUVs (V):

$$G(\tau) = A_P g_P(\tau) + A_V g_V(\tau) \qquad (3\text{-}2).$$

We fit each correlation function with independently-measured diffusion times for CAV-SOL peptide ($\tau_{D,P}$ = 40 μs) and fluorescently-labeled LUVs ($\tau_{D,V}$ ~ 5000 μs). The amplitudes for the summed correlation functions are determined by fitting the autocorrelated data with the diffusion times for the free peptide and the bare LUVs to Equation 3-3.

The molar partition coefficient of the peptide K is a proportionality constant between the fraction of peptide bound to the membrane $[P]_{mem}$ and the molar concentrations of peptide *[P]* and lipids *[L]* in solution and is described by $[P]_{mem} = K[P][L]$ [84]. K is computed from a material balance on the free *[P]* and membrane-bound peptide $[P]_{mem}$ [84]:

$$\frac{[P]_{mem}}{[P]_{tot}} = \frac{K[L]_{acc}}{1 + K[L]_{acc}} = 1 - A_P N_0 \qquad (3\text{-}3),$$

where $[P]_{total}$ is the sum of $[P]_{mem}$ and *[P]*, $[L]_{acc}$ is 50 % of the total lipid concentration, or the approximate concentration of lipids in the outer leaflet of the LUVs that is accessible to the peptide, A_P is determined from fitting Equation 3-3 and N_0 is the number of peptides in the focus volume counted in the absence of LUVs.

3.4 Results

3.4.1 Caveolin-1 Peptide Phase Partitioning

All of the caveolin-1 peptides we study partition into the liquid-disordered (L_d) or cholesterol-poor phase over a range of cholesterol concentrations. The evidence for this partitioning is twofold, demonstrated by (1) the binding of peptides to the majority phase and (2) the colocalization of peptides with the liquid-disordered phase marker, TR-DPPE.

Figure 3-2 demonstrates that the water soluble CAV-SOL peptide at concentration 50 nM added to GUVs in solution binds the majority phase, or the L_d phase of GUVs containing 15 mol % cholesterol, 37.5 mol % DOPC and 37.5 mol % BSM (Figure 3-2, *I* and *II*) and 20 mol % (Figure 3-2 *III a*). We also verify that the lipid raft marker, TR-DPPE, does not affect the partitioning of CAV-SOL into the L_d phase (Figure 3-2, *I* and *II*). The binding of the water-soluble CAV-SOL protein to the L_d phase is further indicated by the colocalization of CAV-SOL and TR-DPPE, which partitions into the less-dense phase of GUVs containing 20 mol % cholesterol, 40 mol % DOPC, 40 mol % and 0.1 mol % TR-DPPE (Figure 3-2 *III*). The equatorial fluorescence confocal micrographs in Figure 3-2 *III* indicate that the CAV-SOL peptide is evenly distributed throughout L_d phase. Figure 3-3 illustrates how both CAV-INSOL (Figure 3-3, *a* and *c*) and CAV-CSD (Figure 3-3, *b* and *d*) added to lipid mixtures at concentration of 1 mol % similarly partition into the L_d phase marked by TR-DPPE. The control experiment in which TR-DPPE is omitted from the lipid mixture is also performed with the CAV-INSOL and CAV-CSD peptides.

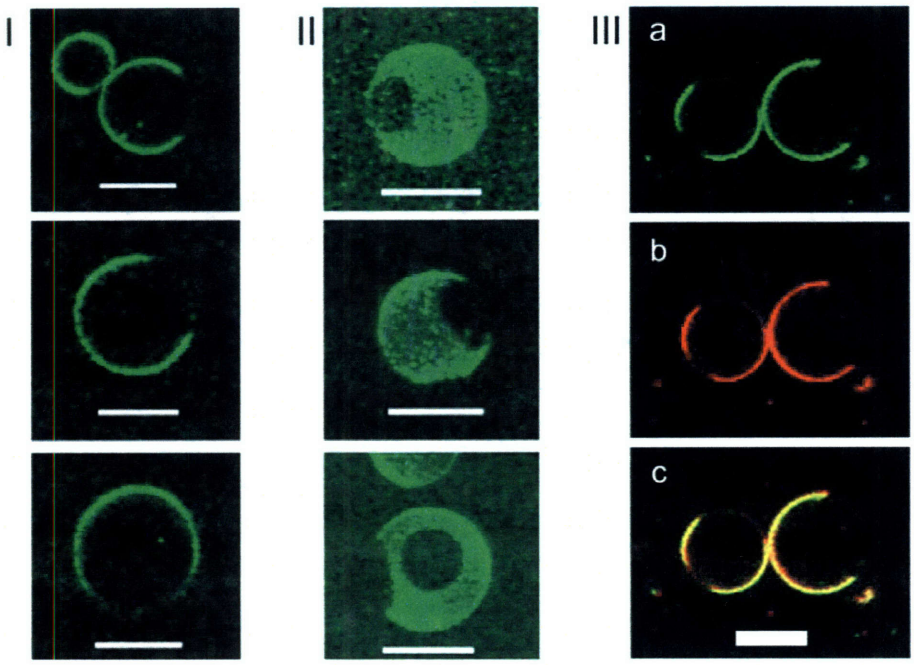

Figure 3-2. Confocal micrographs of CAV-SOL binding to the liquid-disordered phase. Equatorial (*column I*) and three-dimensional reconstruction (*column II*) micrographs of different GUVs containing 15 mol % cholesterol, 1:1 DOPC/BSM. (*Column III*) Equatorial micrographs of GUVs composed of 20 mol % cholesterol and 0.1 mol % TR-DPPE. (*a, green*) 488 nm wavelength laser excitation channel showing CAV-SOL peptide, (*b, red*) 543 nm laser excitation showing TR-DPPE and (*c*) merged images. Scale bars are 20 μm.

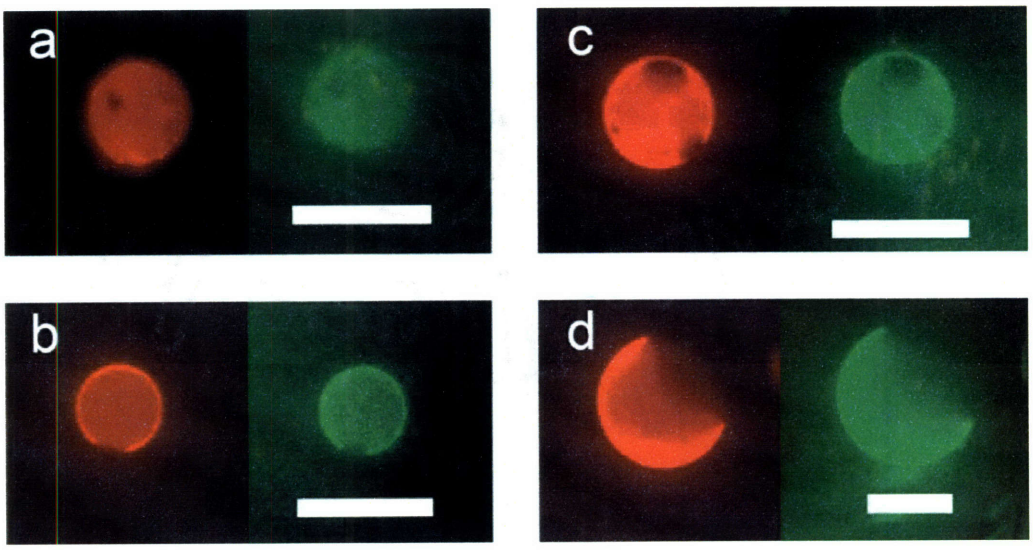

Figure 3-3. Fluorescence micrographs of CAV-INSOL (*a,c*) and CAV-CSD (*b,d*) binding liquid-disordered phase in GUVs containing 10 (*a,b*) and 20 (*c,d*) mol% cholesterol, 1:1 DOPC/BSM. Scale bars are 20 μm.

3.4.2 Caveolin-1 Binding

We further investigate the binding of CAV-SOL to lipid bilayers with the fluorescence correlation spectroscopy-peptide binding assay. Lipid bilayers with varying cholesterol concentration and a fixed 1:1 DOPC/BSM ratio are formed as extruded large unilamellar vesicles (LUVs). There is an approximately two order of magnitude difference between the measured diffusion time of CAV-SOL (40 μs) and the average diffusion time of the LUVs (5000 μs), allowing us to fit the data as a sum of two autocorrelation functions. Increasing the cholesterol concentration decreases the diameter of LUVs extruded from mixtures of cholesterol, DOPC and BSM. The hydrodynamic radii (R_h) measured for DiD-labeled LUVs composed of cholesterol and an equimolar

DOPC/BSM ratio are shown in Table 3-1. An increase in cholesterol concentration corresponds to a decrease in R_h.

Lipid Composition	R_h of LUVs	K [M^{-1}]	Area% of L_d phase
20% chol + 1:1 DOPC/BSM	91 ± 4 nm	~6×10^4	43 ± 16
30% chol + 1:1 DOPC/BSM	89 ± 4 nm	~3×10^4	22 ± 13
40% chol + 1:1 DOPC/BSM	78 ± 3 nm	~1×10^3	no phase separation
50% chol + 1:1 DOPC/BSM	75 ± 3 nm	~7×10^2	no phase separation

Table 3-1. Molar partition coefficients calculated from FCS data.

To systematically investigate the effects of phase separation and cholesterol concentration on CAV-SOL-membrane interaction, we use FCS to study the binding of 50 nM CAV-SOL to membranes in solution. The autocorrelation curves in Figure 3-4 demonstrate the binding of CAV-SOL to LUVs. CAV-SOL binds more strongly to vesicles that have phase-separating lipid mixtures (Figure 3-4, *c* and *d*) and lower cholesterol concentrations than those in a single phase region with higher cholesterol concentrations (Figure 3-4, *e* and *f*). We calculate molar partition coefficients from FCS data (Table 3-1) and show how lower cholesterol concentrations and phase separation increase the membrane-peptide interaction.

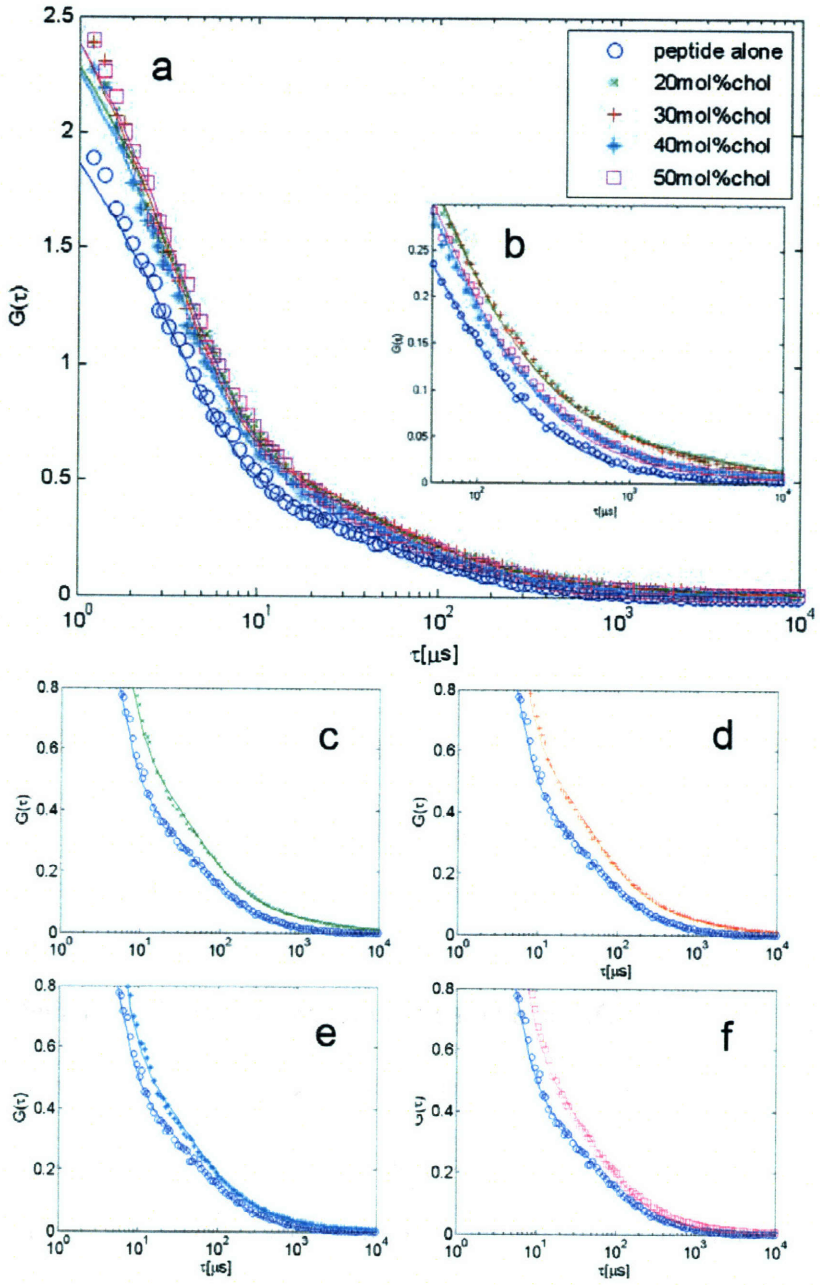

Figure 3-4. FCS data of CAV-SOL peptide binding to LUVs. (*a,b*) FCS data measured for CAV-SOL in solution with and without four compositions of LUVs at accessible lipid concentration of 100 μM containing cholesterol and an equimolar ratio of DOPC and BSM. The FCS data for peptides in the presence of LUVs containing 20 mol (*c*), 30 (*d*), 40 (*e*) and 50 (*f*) mol % cholesterol, 1:1 DOPC/BSM, fitted with 2-component autocorrelation functions.

3.4.3 Caveolin-1 Peptide Phase Diagram

The pseudo-ternary lipid phase diagrams for the DOPC/BSM/cholesterol system with and without the addition of the caveolin-1 peptides are presented in Figure 3-5. The ratio of DOPC to BSM is fixed at 1:1. The miscibility transition temperature, T_m, is measured over a range of cholesterol concentrations with and without added peptides. Both liquid-liquid and liquid-solid phase coexistence are observed. Solid-liquid coexistence is observed only in GUVs with cholesterol concentrations of 10 mol % or less and solid domains are identified by their non-circular morphology, rigid body rotation and inability to ripen into larger domains [44]. In contrast, liquid domains have round, fluctuating edges and can coalesce and form larger domains.

The nearly identical miscibility transition temperatures measured over a range of concentrations with and without CAV-SOL peptide indicate that the addition of CAV-SOL does not affect the phase diagram (Figure 3-5 *a*). By contrast, inclusion of the insoluble caveolin-1 peptides in the GUV membrane does depress T_m for the liquid-liquid transition. As illustrated in Figure 3-5 *b*, the addition of 1 mol % CAV-INSOL and CAV-CSD to GUVs containing 25 and 30 mol % cholesterol causes a significant decrease (>5°C) in T_m. At a composition of 30 mol % cholesterol, not all of the GUVs in the observation slide are phase separated after reaching the lower limit of the microscope cooling stage. The addition of the CAV-INSOL and CAV-CSD to GUVs containing 10 mol % cholesterol does not cause significant change in T_m at the solid-liquid to liquid-liquid phase transition.

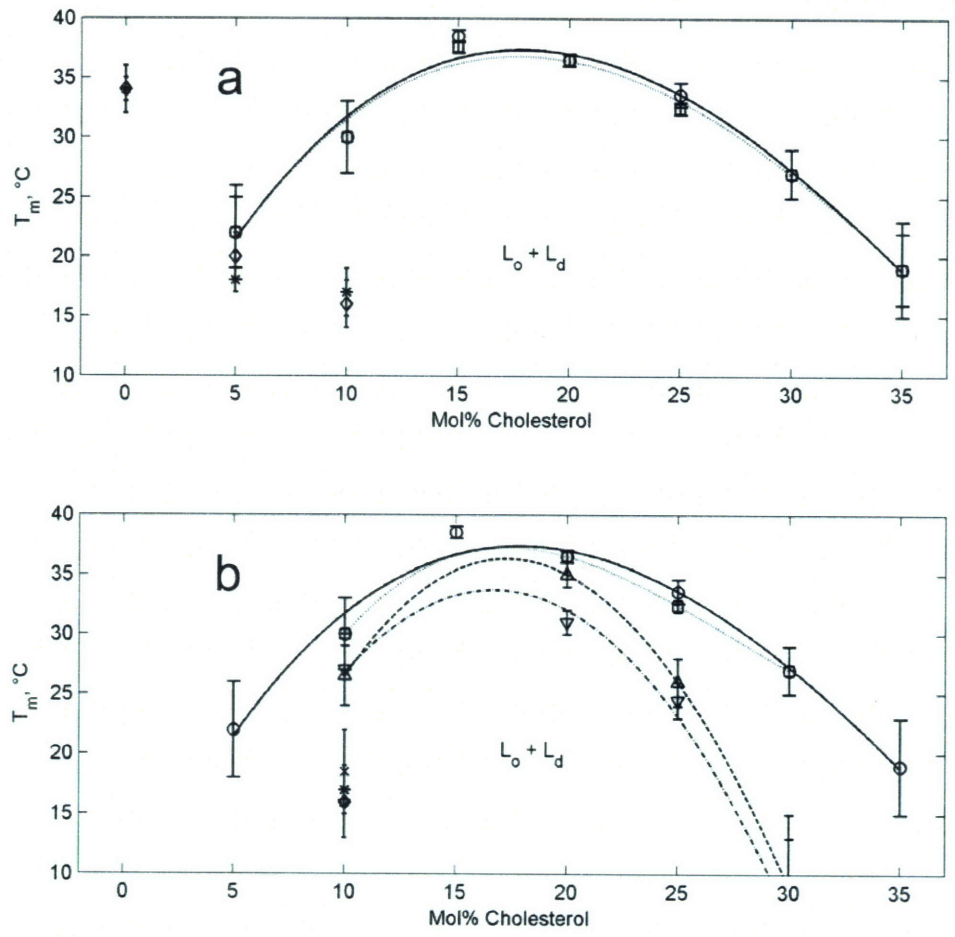

Figure 3-5. Influence of caveolin peptides on partial lipid phase diagrams of GUVs of different cholesterol concentrations and fixed 1:1 DOPC/BSM ratio; $L_o + L_d$ liquid-liquid phase coexistence region shown. (*a*) CAV-SOL does not impact on phase diagram. T_m plotted for for GUVs lacking peptide at transitions from liquid-solid phase coexistence (*diamonds*) and liquid-liquid phase coexistence (*circles, solid curve*) to single liquid phase. Tm measured for liquid-solid (*) and liquid-liquid (*squares, dotted curve*) transitions after addition of 50 nM of CAV-SOL. (*b*) Insoluble peptides influence the liquid-liquid. melting transition T_m for solid-liquid transition at 10 mol % cholesterol with no peptide (*diamonds*), 1 mol % CAV-INSOL (+), 1 mol % CAV-CSD (*star*) and 50 nM CAV-SOL (*) added to GUVs. The liquid-liquid T_m was measured at 20, 25 and 30 mol % cholesterol with 1 mol % CAV-INSOL (*triangle point up, dashed curve*), 1 mol % CAV-CSD (*triangle point down, dash-dotted curve*) and 50 nM CAV-SOL (*squares*) added to GUVs.

Figure 3-6 illustrates how the size and shape of the liquid-ordered domains are qualitatively the same with or without peptides present. The bright cholesterol-poor L_d phase is labeled with TR-DPPE, which is excluded from the cholesterol-rich phase [4, 44]. The circular shape of the cholesterol-rich domains indicates liquid-liquid phase coexistence with high line tension [44] both with and without peptides.

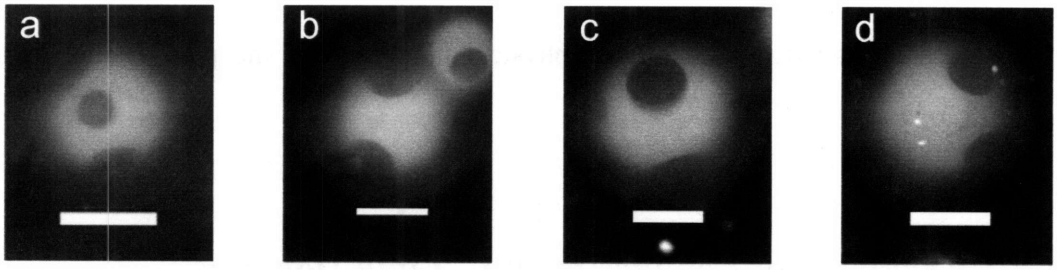

Figure 3-6. Fluorescence micrographs of GUVs containing 20 mol % cholesterol, viewed for TR-DPPE marking the Ld phase with no peptide added (*a*), 50 nM CAV-SOL added to GUVs in solution (*b*), 1 mol % CAV-INSOL (*c*) and CAV-CSD (*d*) included in lipid mixture. Scale bars are 20 μm.

3.5 Discussion

We study the phase partitioning behavior of peptides derived from caveolin-1, a protein known to reside in membrane fractions resembling lipid rafts, but whose exact lipid raft targeting mechanism is not well understood. We investigate the phase partitioning of caveolin-1 peptides in a model membrane system with defined lipid

domains of differing compositions and densities. Cholesterol-rich liquid-ordered (L_o) phases formed from ternary mixtures of BSM, DOPC and cholesterol provide a model system for studying lipid rafts. The composition and morphology of model lipid domains can be studied through lipid phase diagrams [45], which may give insight into the physical properties of lipid rafts in cell membranes. Lipid domains in cells may serve as platforms to locally concentrate molecules such as proteins to enable cell signaling. The preference of a protein for either the L_o domain or the DOPC-enriched liquid-disordered (L_d) domain is dictated both by the physical properties of the protein and the lipid domain.

3.5.1 Exclusion of Peptides from L_0 Lipid Domains

We find that both the soluble and insoluble caveolin-1 peptides partition into the L_d phase at all studied lipid compositions. The fact that caveolin-1 peptides prefer the fluid L_d domains to the dense L_o domains may be due to their exclusion from the tightly-packed L_o domains. L_o domains are more densely packed than L_d domains due to the alignment of the long and saturated fatty acid tails of the sphingolipid molecules and the intercalating cholesterol. The packing of the liquid-ordered phase may be due to hydrogen bonding between the cholesterol and saturated phospholipids or sphingomyelin [42]. Recently, Radhakrishnan and McConnell proposed a model accounting for cholesterol and lipid interactions using cholesterol-saturated lipid complexation and predicted the tie lines of a three-phase lipid diagram [43]. The tight molecular packing and acyl chain alignment within L_o domains may create a local ordered environment that

does not readily accommodate additional molecules. This phenomenon of model peptide exclusion from L_o domains has been previously studied experimentally. The linker for activation of T cells protein is believed to associate with rafts *in vivo*, but it prefers the L_d phases in model membranes studied both using fluorescence microscopy and detergent resistance [97]. Detergent assays demonstrate that model peptides, including hydrophobic transmembrane peptides [98, 99] and palmitoylated peptides [98], are excluded from detergent-insoluble fractions due to tight lipid packing in the detergent-resistant phase.

The exclusion of our caveolin-1 peptides from the L_o phase may also be due to our peptides' lack of lipid anchor moieties and their inability to form oligomers. There are some general trends associated with proteins and peptides that have been shown to partition into L_o lipid phases [47]. In model phase-separated membranes, the cholesterol-binding protein NAP-22 is only targeted to L_o domains in its myristoylated form [100]. In detergent resistance studies, lipidated peptides with multiple acyl chains partition into detergent-insoluble L_o membrane phases [101, 102]. While the C-terminus of caveolin-1 contains three palmitoylated residues, the scaffolding domain we studied does not contain such lipid anchors. An additional important feature of proteins and complexes that have been shown to partition into L_o phases is their ability to oligomerize or form higher-order assemblies. A well-studied example of this effect is the B subunit of the protein cholera toxin (CTB), which binds the ganglioside GM1 with pentameric symmetry and is localized in L_o domains [7]. A recent study suggests that the CTB-GM1 complex localizes to L_o domains only upon complex formation [9]. Using antibodies to cross-link saturated phospholipid analogs causes the lipids to show increased affinity for L_o phases

in model lipid membranes [7]. Human placental alkaline phosphatase (PLAP) has a glycosylphosphatidylinositol anchor and researchers have shown that cross-linking PLAP favors its partitioning into L_o domains [82]. The scaffolding domain of caveolin-1 alone is insufficient for oligomerization; in addition to the CSD, residues 61-101 of the N terminus [103] and residues 168-178 in the C-terminal domain are necessary for oligomerization of caveolin-1 constructs *in vivo* [104]. Recent work in live cells suggests that the oligomerization of caveolin-1 is important for the protein to exit the Golgi complex, to acquire detergent insolubility and to associate with the plasma membrane [105]. The oligomerization of caveolin-1 and the formation of caveolin filaments that are anchored into the membrane are responsible for the invaginated morphology of cellular caveolae [19, 28, 106, 107]. We do not observe measurable changes in lipid curvature or domain morphology when we included caveolin-1 peptides in our lipid membranes. Our peptides' inability to form oligomers and their lack of lipid anchor moieties also precludes the deformation of the membrane into highly-curved invaginations.

The result that our caveolin-1 peptides are excluded from the L_o phase is less surprising for the shorter peptides CAV-SOL and CAV-INSOL, which lack the full-length CSD that is necessary to target caveolin-1 constructs to caveolae *in vivo* [48]. We also demonstrate, however, that CAV-CSD does not partition into L_o domains in our model membrane system. In the *in vivo* investigation of CSD constructs targeting to detergent-assayed raft domains, the CSD was targeted to rafts only 20% as efficiently as full-length caveolin-1 [48]. While detergent extraction is the standard assay for determining whether proteins prefer the L_d or L_o phase in cells [108], some question

whether detergent resistance can be used to determine whether a protein resided in a domain prior to detergent extraction [109]. Another concern in comparing the live cell membranes and their detergent extracts to model membrane systems is bilayer asymmetry. The two leaflets of the cell plasma membrane have asymmetric lipid compositions and densities, which are not preserved in the detergent extraction process [110]. Model membranes approximating the lipid composition inner leaflet of the plasma membrane, where caveolin-1 is thought to bind, do not phase separate into L_d and L_o phases [111]. Previous model membrane experiments demonstrate that CSD peptides can reside in membranes regions enriched in cholesterol, PIP_2 and acidic lipids [91], yet our model membrane system is substantially different. The defined immiscible L_o and L_d lipid domains studied here differ in molecular density and contain sphingomyelin, a known component of cellular caveolae [87]. The tight molecular packing in the L_o domains excludes CAV-CSD from the L_o domains. Our results may also suggest limitations associated with using model lipid rafts to approximate cholesterol-rich domains in cellular membranes. Recent reviews highlight the gaps in our understanding of lipid rafts in controlled model systems and rafts in cellular membranes [109, 110, 112].

The tendency of our caveolin-1 peptides to associate with less-dense membrane domains is further demonstrated by FCS experiments with CAV-SOL. The water solubility of CAV-SOL allowed us to quantify the binding of this peptide to membranes with varying cholesterol concentrations using FCS. In our assay, the peptide is added to LUVs in solution and binds more strongly to LUVs with phase-separating lipid compositions (20 and 30 mol % cholesterol, 1:1 DOPC/BSM) than non-phase-separating

lipid compositions (40 and 50 mol % cholesterol, 1:1 DOPC/BSM) (Table 3-1). The peptide's enhanced binding to membranes containing the L_d phase over homogeneous membranes with high cholesterol content (40, 50 mol %) is consistent with the preference of CAV-SOL for less-dense and more fluid membranes. Our measured molar partition coefficients for CAV-SOL binding to LUVs are $\sim 10^4$ M^{-1} for phase-separated lipid mixtures and $\sim 10^3$ M^{-1} for non-phase-separating lipid mixtures. We measure the relative area fraction of the L_d phase in GUVs (Table 3-1) and doubling the area fraction of the L_d phase to which CAV-SOL binds approximately doubles the molar partition coefficient. Our measured molar partition coefficients are similar to those measured with a shorter caveolin-1 peptide containing residues 92-101 bound to vesicles with low (1-10 mol %) acidic lipid compositions measured by sucrose gradients and radiolabeling of peptides [93].

The observation of lipid phase separation in mixtures of cholesterol, sphingomyelin and DOPC can give insight into the fluidity and ordering of membranes. In these model studies domains are defined as microscopic immiscible phases with simple morphologies [113]. The lipid miscibility transition temperatures of lipid phases can be influenced by the length of lipid acyl chains [79] and clustering of protein molecules [17]. We study the miscibility transition of membranes containing cholesterol, BSM and DOPC and caveolin-1 peptides to study how the peptides influence T_m and the morphology of the lipid phases. We show that the water-soluble peptide has negligible impact on the phase diagram and the insoluble peptides depress T_m at cholesterol concentrations above 20 mol %.

3.5.2 Changes to Lipid Phase Diagram Induced by Peptides

We demonstrate that the phase diagram and phase morphology of membranes with 1:1 DOPC/BSM ratio and different cholesterol compositions are unaffected by the addition of CAV-SOL peptide (Figs. 3-5 and 3-6). The identical miscibility transition temperatures measured over a range of lipid compositions with and without CAV-SOL (Figure 3-5 *a*) indicate that CAV-SOL does not moderate the relative amounts of cholesterol nor does it redistribute the lipid concentrations in the two phases and that CAV-SOL is unable to induce the formation of cholesterol-rich phase-separated domains in non-phase-separated lipid bilayers. We attribute this lack of impact on the partial phase diagram to the weak-to-moderate binding of the CAV-SOL peptide to membranes. We do not expect CAV-SOL to penetrate deeply into lipid bilayer membranes. The interaction of similar caveolin-1 peptides and lipid bilayer membranes has been previously studied both with model membrane systems and *in vivo*. The membrane attachment sequence of caveolin-1 is KYWFYR and was identified through mutagenesis experiments and posited to insert into inner membrane leaflet of cells [90]. The same sequence KYWFYR was subsequently investigated with NMR was less inserted into model membranes composed of cholesterol in SOPC membranes than a peptide comprising the well-characterized cholesterol-binding sequence LWYIK [33]. These same authors also demonstrate that longer caveolin-1 peptides with sequence VTKYWFYR and the full CSD do not penetrate into SOPC and cholesterol membranes as deeply as LWYIK [92].

Unlike CAV-SOL, the insoluble peptides CAV-INSOL and CAV-CSD decrease T_m at cholesterol concentrations greater than 20 mol % (Figure 3-5 *b*). CAV-INSOL and CAV-CSD incorporated into cholesterol/BSM/DOPC membranes prevents the formation of L_o phases at miscibility transition temperatures observed without the peptides. We expect that the mechanism of the insoluble peptides interacting with membranes in our experiments to be different than how the water-soluble peptide binds membranes. Unlike CAV-SOL experiments where peptides were added to pre-existing lipid membranes in solution, CAV-INSOL and CAV-CSD are included in the lipid mixture prior to forming membranes and were therefore able to access the full depth of the membranes and interact with all molecules in the lipid mixture. Phase separation is thought to be driven by the tendency of sphingolipids to interact with cholesterol and form ordered domains [3, 43, 114] and our results suggest that CAV-SOL and CAV-INSOL disrupt this phase separation process. The decrease in T_m that we observed at the liquid-liquid to single liquid phase transition suggests that the addition of the insoluble peptides to the membranes also increases the fluidity of the membrane by promoting a single homogeneous phase.

3.6 Conclusions

The widely-used model lipid raft system of cholesterol, DOPC and a saturated lipid or sphingolipid may give insight into lipid rafts in cells and the formation of liquid-ordered phases enriched in cholesterol. Studying the temperature- and composition-dependence of lipid phase separation may improve our understanding of how proteins affect lipid packing and mobility. The insoluble caveolin-1 peptides CAV-INSOL and CAV-CSD depressed the melting temperature of liquid lipid phases, suggesting that the insoluble caveolin-1 peptides prevent the lateral organization of lipids at certain temperatures and therefore promote membrane fluidity. This effect contrasts the result that CAV-SOL added to membranes in solution did not impact the partial phase diagram. Model liquid-ordered domains have a dense molecular environment that is unfavorable to caveolin-1 peptide insertion. The insoluble scaffolding domain is excluded from the liquid-ordered phase, despite its earlier demonstrated preference for cholesterol in model membranes [91] and its localization to detergent-insoluble fractions of cell membranes [48]. We attribute the partitioning of our caveolin-1 peptides into liquid-disordered domains to their exclusion from the tightly-packed liquid-ordered domains and their preference for more fluid membranes. Overcoming the exclusion of molecules from the tightly-packed liquid-ordered domains may be achieved by lipid anchor moieties or oligomerization. While the full-length protein both oligomerizes and has palmitoylation sites, our peptides lack these features.

CHAPTER 4. PROTEIN ORDERING ON LIPID BILAYER VESICLES

4.1 Introduction

Proteins are often required to guide and direct the deformation of cell membranes and induce structural transformations important for biological processes including endocytosis [19, 22]. One such protein is clathrin, which assembles on the cellular membrane surface into a well-defined lattice to form invaginations termed clathrin-coated pits that eventually produce internal buds that are part of the endocytotic pathway [23-25]. This physical process is driven by the fact that the curvature of the clathrin protein lattice exceeds that of the membrane and is believed to influence the size of the clathrin-coated vesicles that are formed [24, 25]. In addition to their role in biological processes, protein arrays on lipid bilayers also have potential application in biosensing and drug delivery, where a well-defined template of proteins can be immobilized on vesicles [55].

Model systems of proteins on lipid bilayer membranes allow for systematic study of how protein arrays self assemble and influence lipid membrane shape and curvature. The tetrameric protein streptavidin also forms two-dimensional crystalline domains when bound to the surface of biotin-functionalized giant unilamellar vesicles (GUVs) [56, 115].

Previous studies of streptavidin ordering on GUVs demonstrate that streptavidin-coated GUVs can deform into football-like prolate shapes when the streptavidin protein domains are aligned and form a continuous envelope (Figure 4-1) [115]. Micropipet aspiration of streptavidin-coated GUVs shows that the protein-coated bilayer plastically deforms and GUVs crumple as they deflate [56]. However, the physical mechanisms for how the streptavidin domains align and determine membrane shape have not been systematically explored.

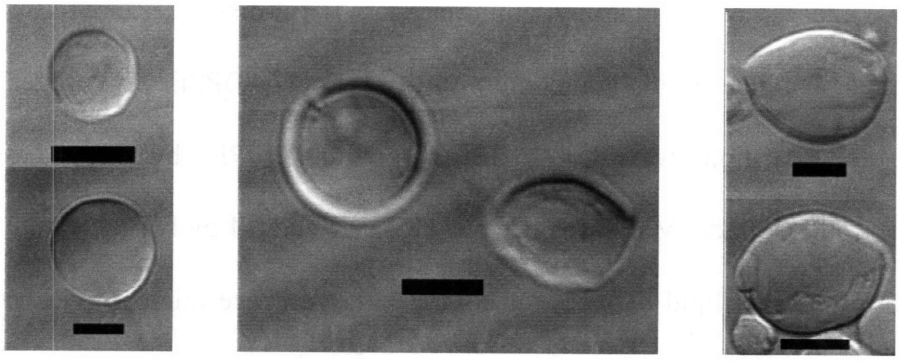

Figure 4-1. DIC micrographs of GUVs coated with streptavidin with spherical (*left*) and spheroidal (*right*) morphology. 10 μm scale bars.

We investigate the relationship between the configuration of crystalline streptavidin domains and vesicle morphology. The streptavidin-coated membrane system contrasts clathrin-coated membranes, because rather than inducing curvature, we find that streptavidin domains flatten membranes and resist membrane bending. We develop a simple model based on domain growth and jamming to account for the shape

transformations of the GUVs. We osmotically stress streptavidin-coated GUVs to study how protein-coated bilayers respond to deflation and to qualitatively examine how rigid protein domains influence GUV morphology and stability.

4.2 Materials and Methods

GUVs are prepared by the electroformation method [116] described in Chapter 2 from a mixture of 1-stearoyl-2-oleoyl-*sn*-glycero-3-phosphocholine (SOPC, Avanti Polar Lipids) and *N*-((6-(biotinoyl)amino)hexanoyl)-1,2-dihexadecanoyl-*sn*-glycero-3-phosphoethanolamine, triethylammonium salt (biotin-X-DPPE, Invitrogen). Lipid mixtures are 10:1 lipid weight ratio (SOPC/biotin-X-DPPE) by mass dissolved in chloroform (HPLC grade, Mallinckrodt) [56, 115]. We add 0.1 mol % of TR-DPPE to the lipid mixture to label lipid bilayers for confocal fluorescence microscopy experiments. GUVs are formed in 608 mOsm glucose solution and suspended in sucrose in order to provide optical and density contrast [117]. To osmotically stress the GUVs, we suspend glucose-filled GUVs in hyperosmotic sucrose solutions. In order to achieve higher osmotic stress gradients, we also form vesicles in 300 mOsm glucose.

Electroformed GUVs are incubated in 20 μg/mL protein solution for at least 3 h to allow crystals to grow and equilibrate on the bilayer surface. Protein solutions are prepared containing streptavidin (Invitrogen), egg white avidin (Sigma-Aldrich) and Alexa488-avidin (Invitrogen) dissolved in glucose solutions of the same osmolarity as those we use to form GUVs. The pH of the GUV and protein solution is adjusted from

pH 5.3 to pH 6 using a 500 mM Tris base solution. GUVs are imaged within 12 h of synthesis, but remain stable up to 48 h.

Differential interference contrast (DIC) and fluorescence microscopy images are obtained with 40× and 100× objectives. Glucose-filled vesicles are diluted 5-fold with 660 mOsm sucrose for microscopy. To measure size distributions of the GUVs, we analyze DIC micrographs using ImageJ software. GUVs are classified as either spherical or spheroidal; spheroidal GUVs have an aspect ratio greater than 1.1. We determine the minimum curvature of the spheroidal GUVs by fitting a circle to the major vesicle curvature.

To study the retention of solutes within the membrane, GUVs are formed in a glucose solution containing fluorescently-labeled dyes. Either 10 μg/mL of 10,000MW Texas Red-Dextran or 100μg/mL of flourescein sodium salt (both Invitrogen) are added to the sugar swelling solution. GUVs are diluted in sucrose 10-20 fold for fluorescence microscopy visualization of the concentrated dye inside the vesicles to indicate whether GUVs leak or rupture.

4.3 Results and Discussion

4.3.1 Shape Transformation

When streptavidin binds to a GUV containing biotinylated lipid, it interacts with neighboring streptavidin proteins to form two-dimensional crystalline protein arrays on the surface of the GUV [115]. When the streptavidin crystals are aligned, GUVs exhibit spheroidal morphology (Figure 4-2). We visualize the streptavidin crystal morphologies on the surface of fluorescently-labeled GUVs by incubating them in a 10:1 wt ratio of streptavidin and Alexa488-Avidin. Avidin binds biotin with an affinity near that of streptavidin but does not crystallize. The fluorescent avidin provides a bright background to visualize streptavidin domains on the GUV surface approximately 5 μm in length. When streptavidin domains are randomly oriented (Figure 4-2, *left*), GUVs have a spherical morphology. When streptavidin domains align approximately parallel and span the length of the GUV (Figure 4-2, *right*), GUVs have football-like shapes which we approximate as prolate spheroid.

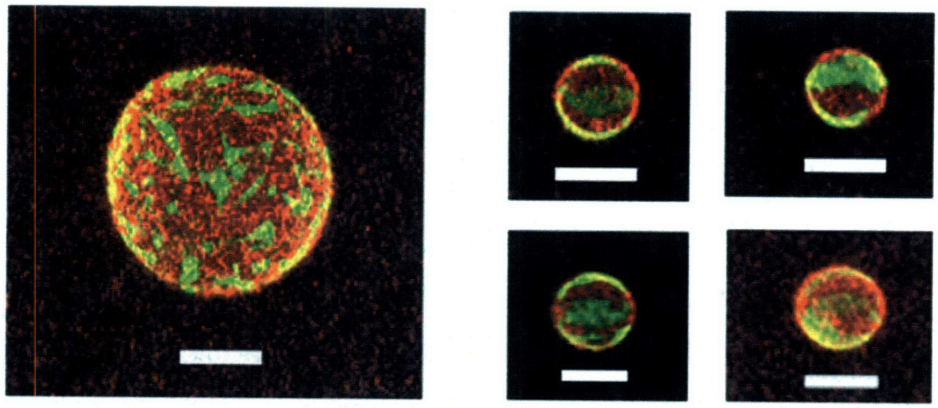

Figure 4-2. Confocal fluorescence micrographs of protein-coated GUVs incubated in 90 wt % streptavidin and 10 wt % Alexa488-avidin solution. Fluorescently-labeled avidin (*green*) is used to visualize crystalline streptavidin domains on (*red*) fluorescently-labeled bilayer. (*Left*): spherical GUV and (*right*): spheroidal-shaped GUVs with aligned streptavidin crystalline domains. Scale bars are 10 μm.

Viewing the protein-coated membrane as a composite material, we can qualitatively understand how protein domain alignment influences GUV curvature. If the crystalline domains are a rigid, continuous material, then bending along the major axis of the spheroidal GUVs is similar to bending parallel beams. This physical model is supported by the observation that curvatures along the major axes of the spheroidal GUVs in Figure 4-2, where streptavidin protein domains are aligned, are lower than the curvatures of spherical GUVs. Along the minor axis of the spheroidal GUVs, however, there is not continuous rigid crystalline material, but rather defects between crystalline domains where we expect the membrane to bend more easily. The preference of streptavidin crystals to grow in a planar fashion is consistent with the previous

observation of large streptavidin crystals that readily grow up to 100 μm in size on flat bilayer and monolayer surfaces [62].

4.3.2 Size Trend

An additional observation from Figure 4-2 is that the spherical GUV (*left*) is larger in size than the spheroidal GUVs (*right*). We verify and quantify this trend through analysis of the size and geometry of a population of 250 GUVs coated only with streptavidin and imaged with DIC microscopy. Spheroidal GUVs are defined by having an aspect ratio greater than 1.1. We plot the percent of spheroidal and spherical GUVs at each diameter in Figure 4-3 to show that smaller GUVs tend to have spheroidal morphology while larger GUVs tend to have spherical morphology. We define the diameter of the spheroidal GUVs as the length of the major axis. Although spheroidal GUVs are observed with a range of sizes, their proportions remain approximately constant with aspect ratio defined as the length of the major axis over the length of the minor axis of 1.18 ± 0.08. This suggests that the curvature of the surface on which the streptavidin crystals grow influences the preferred curvature of the crystals that are formed. Smaller GUVs have higher curvature than larger GUVs; thus, streptavidin crystals growing on smaller GUVs must conform to a higher membrane curvature than crystals grown on larger GUVs or planar bilayers.

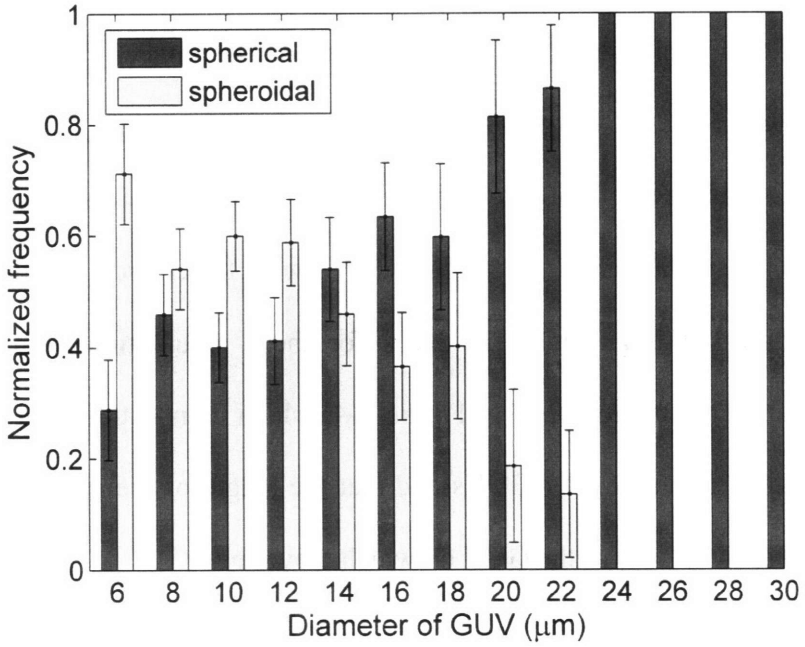

Figure 4-3. Normalized size distributions of spherical and spheroidal GUVs. Spheroidal GUVs tend to be smaller in size than the spherical GUVs. The GUV diameter of the spheroidal GUVs is defined as length of the major axis. Error estimated from binomial distribution statistics from N=250 GUV micrographs analyzed.

We propose a crystal growth and jamming model to account for the observation that spheroidal GUVs tend to be smaller. We assume that the number of nucleation sites per unit area is constant for all lipid bilayer surfaces, as illustrated by the schematic in Figure 4-4 (*left*) showing the early nucleation of protein domains on both a large and small GUV at time t_1. At a later time t_2 the protein domains have grown and begin to contact adjacent domains. We define jamming as the state at which protein domains are in contact with one another and are no longer able to grow. For simplicity, we assume that for a given GUV, the growth rate of the domains is the same on all surfaces of that

GUV. If the protein domains have random orientations as they begin to grow, then the probability of having aligned domains is increased on the smaller GUVs because there are fewer protein domains. In other words, the fractional probability of N objects with random orientations on a grid of size N having the same orientation scales exponentially as $\sim N$; therefore, smaller grids, or smaller GUVs with fewer protein domains, have a higher probability of alignment. The basis for these assumptions is confirmed by fluorescence and DIC micrographs in Figure 4-4, which demonstrate that larger GUVs have more domains than smaller GUVs and that the length of the streptavidin domains does not depend on the size of the GUV on which they grow.

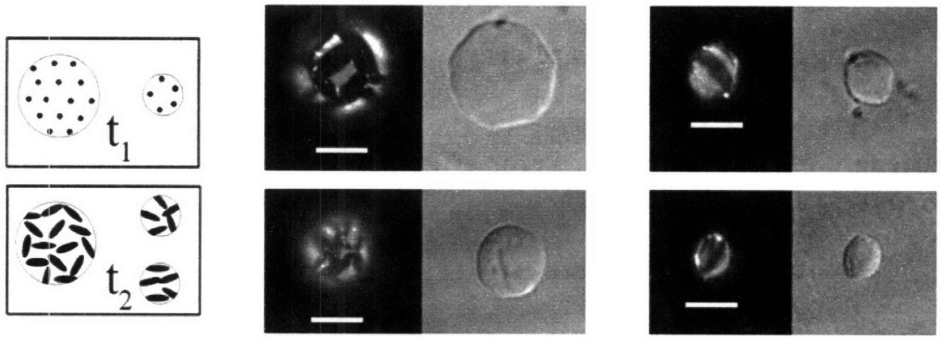

Figure 4-4. Model for crystalline domain growth and size trend. (*Left*): Illustration of domains at early (t_1) and late (t_2) time scales. (*Middle* and *right*): Fluorescence and DIC micrographs of GUVs incubated in 90 wt % streptavidin and 10 wt % Alexa488-avidin protein solution. Spherical GUVs (*middle*) are larger and have more randomly-oriented domains than spheroidal GUVs (*right*), which have aligned domains. All scale bars are 10 μm.

To verify the consistency of this physical picture, we estimate the time scales for the protein domains to grow and diffuse. Streptavidin crystals have a preferred growth direction on biotinylated GUVs, with C222 crystal lattice structure [62]. The rate of streptavidin domain growth along the preferred growth direction measured on monolayers is 1-50 μm/min [64]. We take the lower value of 1 μm/min because our low ionic strength solution conditions should slow protein crystalline growth [62]. Based on this growth rate, crystals reach their 5 μm length within 5 min. We compare this time scale to the approximate time scale for the protein domains to rotate in the membrane. The rotational diffusion, D_R, of a molecule of length ℓ rotating in a membrane with viscosity μ can be calculated from the equation

$$D_R = \frac{k_B T}{8\pi\mu\ell^3} \qquad (4\text{-}1),$$

where k_B is Boltzmann's constant and T is temperature. We calculate the membrane viscosity, $\mu = 9\times10^{-2}$ Pa·s, using the Stokes-Einstein equation and the estimated diffusivity of monomolecular streptavidin [64], $D_T = 5\times10^{-9}$ cm^2/s. We can use this to calculate the rotational diffusion coefficient D_R and the characteristic time scale for domain rotation [118], $t_R \sim 1/D_R$, over a range of streptavidin domain sizes. We find that $t_R \sim 0.5$ s when domains are 0.1 μm in size and we estimate $t_R \sim 70$ min when domains are 2 μm in size. Comparison of the rotational diffusion time scales with our estimated time scale for crystal growth indicates that the domains grow much faster than they rotate. As the

domains grow quickly on the GUV surface, they are not free to rotate and they approach a jammed configuration.

4.3.3 Effect of Streptavidin/Avidin Ratio on Vesicle Shape Transformation

An important consideration in understanding how the arrangement of jammed streptavidin domains on the GUV surface influences vesicle shape is the surface coverage of crystalline streptavidin. By adjusting the relative amounts of avidin and streptavidin in the protein incubation solution, we can control the surface coverage of crystalline streptavidin relative to non-crystalline avidin. The fraction of GUVs transformed into a spheroidal shape increases as the concentration of streptavidin in the protein solution increases, as shown in Figure 4-5. The minimum amount of streptavidin in the protein solution required to observe spheroidal GUVs is 74-78 mol % streptavidin. Micrographs (Figure 4-5, *b-d*) illustrate that the surface coverage of streptavidin crystals increases as the concentration of streptavidin in the GUV incubation solution increases. The approximate amount of streptavidin required to observe microscopic crystals with optical microscopy is 25 mol % streptavidin (Figure 4-5, *b*). This minimum concentration threshold is comparable to streptavidin crystallization threshold observed on monolayers [64] of 15 mol %.

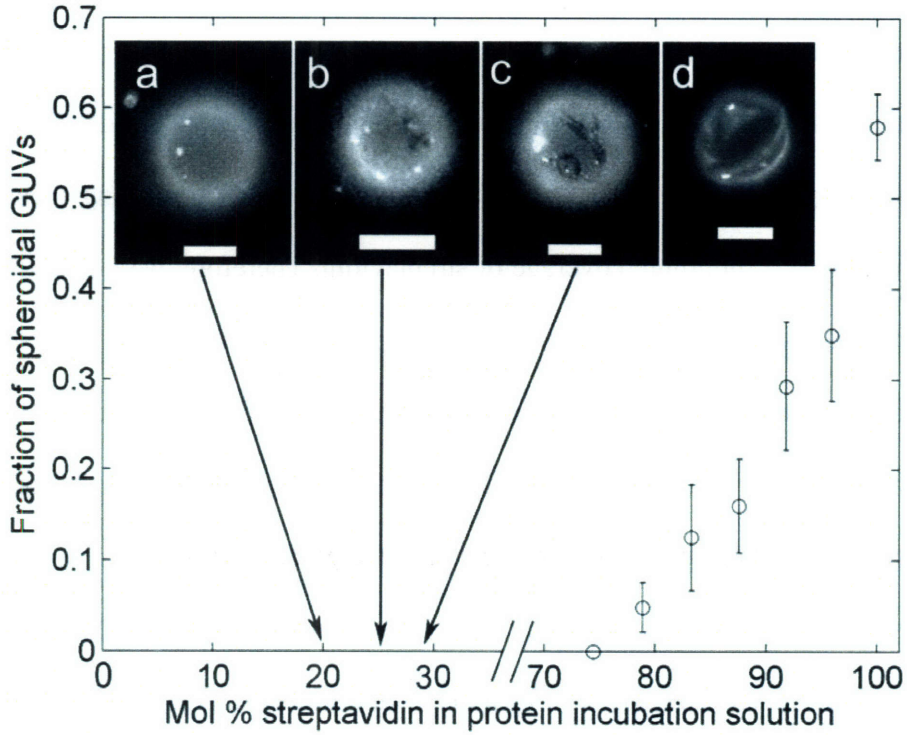

Figure 4-5. Graph of measured relationship between the fraction of GUVs observed with spheroidal morphology and amount of streptavidin used to coat GUVs. Error estimated from binomial distribution statistics of N=411 micrographs analyzed. Fluorescence micrographs of protein-coated GUVs with varied concentrations of streptavidin: (*a*) 20 mol %, (*b*) 25 mol %, (*c*) 29 mol % and (*d*) 90 mol %. The remaining protein incubation solution contains 10 mol % Alexa488-avidin and the balance egg white avidin. (*a*): No microscopic protein domains are observed on GUVs. All scale bars are 10 μm.

Consideration of the geometry and coverage of protein crystals near the sphere-to-spheroid shape transformation threshold allows us to qualitatively describe the mechanism for spheroidal GUV formation. We observe that spheroidal GUVs require an aligned continuous network of crystalline streptavidin domains along their major axes, which requires a minimum coverage of streptavidin. Therefore, we qualitatively describe the onset of the sphere-to-spheroid GUV shape transformation as an aligned percolation process, where microscopic streptavidin domains are the percolating material. Once protein domain coverage enables the formation a continuous network spanning the GUV length, a percolation threshold is reached and the percolated protein network can deform GUVs into a spheroidal geometry. In our system, we observe spheroidal GUVs beginning at streptavidin concentrations of ~75 mol %; fluorescent micrographs suggest that below this streptavidin concentration, the coverage of protein crystals is insufficient to form a continuous material spanning the membrane dimension (Figure 4-5, *b* and *c*). At streptavidin concentrations above the shape transition threshold, we observe an approximately linear dependence of the amount of shape-transformed GUVs on the concentration of streptavidin in the protein incubation solution (Figure 4-5).

Our observations are qualitatively similar to other studies of two-dimensional percolation of objects with elongated geometry. Studies of randomly-oriented sticks and their two-dimensional percolation in an aligned direction as a function of stick concentration and stick alignment show a similar trend, where the probability of percolation increases approximately linearly as the concentration of sticks increases [119]. We estimate the surface coverage of streptavidin crystals at percolation using

results for 2-D randomly-oriented overlapping ellipses. If we approximate the streptavidin crystalline domains as ellipses with aspect ratio of 2-3, then the approximate coverage of the ellipsoidal domains in a 2D system at percolation, p, can be calculated as $1-p_c$, where p_c is the area fraction of the surface not covered with overlapping ellipses. The formula to estimate p_c as a function of the ellipses' aspect ratio b/a is [120] $p_c=(1+4y)/(19+4y)$ and $y=b/a+a/b$. We estimate the net area covered by overlapping ellipses, or the streptavidin crystalline domains, at the percolation threshold to be 0.56–0.62. In our system, the approximate fraction of the GUV surface covered by streptavidin domains when GUVs are coated with 90 mol % streptavidin is ~0.5. This measurement is only an approximation, as we are limited by using 2D images to approximate a 3D surface; however, it suggests that the coverage of streptavidin domains when GUVs incubate in a solution containing 90 mol % streptavidin is sufficient to span the surface of the GUVs and thus enable observation of spheroidal GUVs.

4.3.4 Osmotic Stress Response of GUVs

Osmotically stressing our protein-coated vesicles allows us to more thoroughly investigate how the streptavidin domains resist bending and determine the GUV shape and stability. Osmotic deflation of lipid bilayer vesicles can be used to characterize membrane topology [121] and vesicle shape transformations [122]. We osmotically deflate the glucose-filled GUVs by placing them in a concentrated sucrose medium; the resulting hyperosmotic environment causes the vesicles to lose part of their internal water volume to equilibrate the osmolarity of the external and internal solutions [123].

Streptavidin-coated GUVs viewed in a hyperosmotic sugar environment have two distinct morphologies: roughened spherical or spheroidal, with a ridge along the vesicle major axis [115]. Interestingly, under increasing osmotic stress spheroidal GUVs maintain their major axes and proportions. Figure 4-6 shows the measured curvatures of different populations of spheroidal GUVs subjected to osmotic stress gradients ΔOsm=50-400 mOsm (Figure 4-6). Though we vary the osmotic gradient used to stress the GUVs, the ratio of major curvature to GUV diameter remains approximately constant. DIC micrographs illustrate how the spheroidal GUVs maintain their morphology even under high osmotic stress (Figure 4-6, *a-d*).

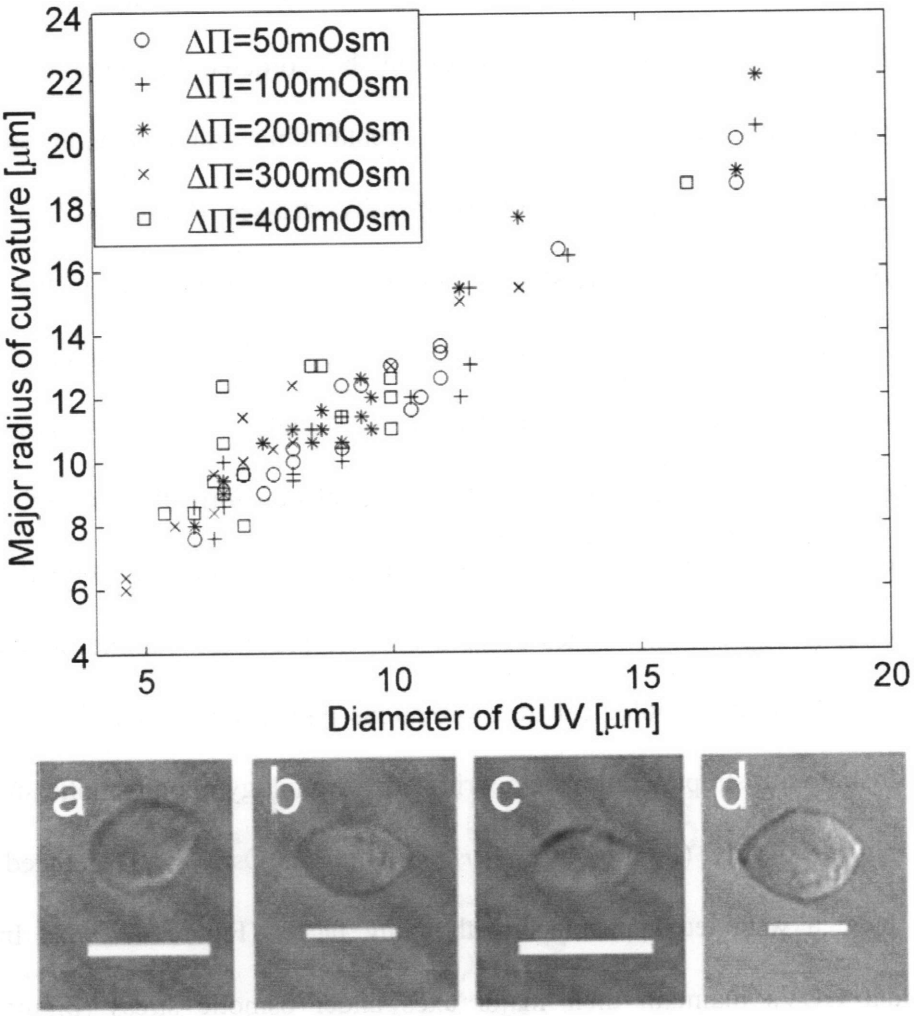

Figure 4-6. Spheroidal GUVs maintain their shape under osmotic stress. (*Above*): Minimum curvature of spheroidal GUVs at different osmotic stress gradients for N=68 GUVs. The ratio of the minimum curvature to the GUV diameter is approximately constant. (*Below*): DIC micrographs of streptavidin-coated GUVs deflated with osmotic stress gradients of (*a*) *ΔOsm*=100 mOsm, (*b*) 200 mOsm, (*c*) 300 mOsm and (*d*) 400 mOsm. Scale bars are 10 μm.

We compare the osmotic stress responses of bare GUVs and GUVs coated with crystalline vs. non-crystalline protein to examine how ordered protein domains affect the bending properties of the lipid bilayer. Bare, streptavidin/avidin and avidin-coated GUVs remain spherical when they are not osmotically stressed (Figure 4-7, *left column*). Streptavidin domains, however, slightly deform the membrane even in the absence of osmotic stress (Figure 4-7, *b, left column*). Upon application of an osmotic stress, bare, uncoated vesicles can produce internal daughter vesicles (Figure 4-7, *i*) and become flaccid (Figure 4-7, *ii*). These shape and topological transformations resulting from the decrease in vesicle volume have been observed [121-125] and characterized in terms of the bending energy and mechanics of lipid bilayers [126]. Crystalline protein domains prevent the shape and topological transformations typically observed for lipid bilayers. GUVs coated with streptavidin have a wrinkled morphology upon osmotic stressing and shrink anisotropically (Figure 4-7, *b, right column*). Osmotically-deflated spherical GUVs have a wrinkled appearance with many facets (Figure 4-7, *iii*). In contrast, spheroidal GUVs maintain their major axes under osmotic stress (Figure 4-7, *iv*). Comparing crystalline and non-crystalline protein coatings further reveals the impact of the crystalline domains on the osmotic deflation response of the GUVs. When coated with a mixture of avidin and streptavidin, osmotically-stressed GUVs have a wrinkled morphology similar to GUVs incubated in only streptavidin (Figure 4-7, *c, right column*). This contrasts the behavior the avidin-coated vesicles (Figure 4-7, *d*), which maintain a smooth, spherical morphology when stressed but resist budding of the formation of daughter vesicles. Avidin-coated vesicles often rupture even in the absence of osmotic

stress gradients and few GUVs are present at osmotic gradients above *ΔOsm*=250 mOsm. This effect may be due to the affinity of the avidin-coated GUVs for the glass surfaces that has been previously observed [56].

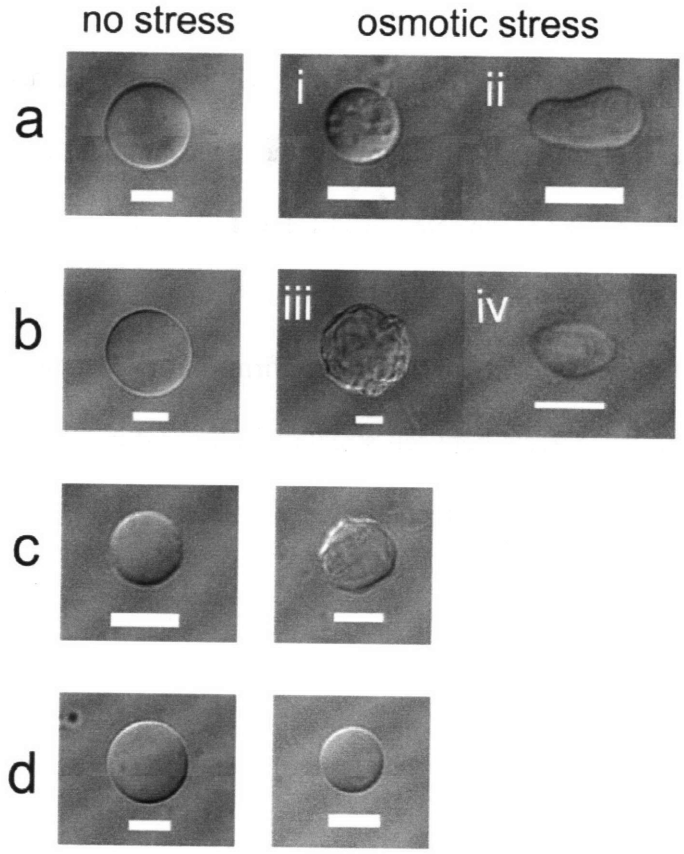

Figure 4-7. DIC micrographs of GUVs with and without applied osmotic stress. (*a*): Bare GUVs unstressed (*left column*) and with *ΔOsm*=250 mOsm osmotic stress (*right column*). Bare osmotically-stressed GUVs produce daughter vesicles (*i*) or become flaccid (*ii*). (*b*): GUVs coated with streptavidin unstressed (*left*) and osmotically stressed (*right*) with roughened spherical geometry at *ΔOsm*=250 mOsm (*iii*) and spheroidal geometry at *ΔOsm*=200 mOsm (*iv*). (*c*): GUV incubated in 50 wt % streptavidin/50 wt % avidin protein solution unstressed (*left*) and with *ΔOsm*=250 mOsm (*right*). (*d*): GUV incubated in avidin protein solution unstressed (*left*) and with *ΔOsm*=250 mOsm (*right*). Scale bars are 10 μm.

We visualize the wrinkles and facets of osmotically-stressed streptavidin-coated vesicles in more detail with confocal fluorescence microscopy and fluorescently-labeled lipid in Figure 4-8. Equatorial micrographs of spherical GUVs (Figure 4-8, *a-c*) illustrate the wrinkled or folded regions of the fluorescently-labeled lipid bilayer that form when the protein-coated membrane is deflated by osmotic stress. Folded features become deeper and have higher local curvature as the concentration gradient is increased. Spheroidal GUVs exhibit concentrated lipid folding along their major axes (Figure 4-8, *d*). The lipid fold in Figure 4-8, *d* penetrates the GUV to a depth of approximately 33% of the total depth of the spheroidal GUV. This confirms our expectation that the membrane should yield along the defects between streptavidin crystalline domains, which are at a higher density in this minor axis direction.

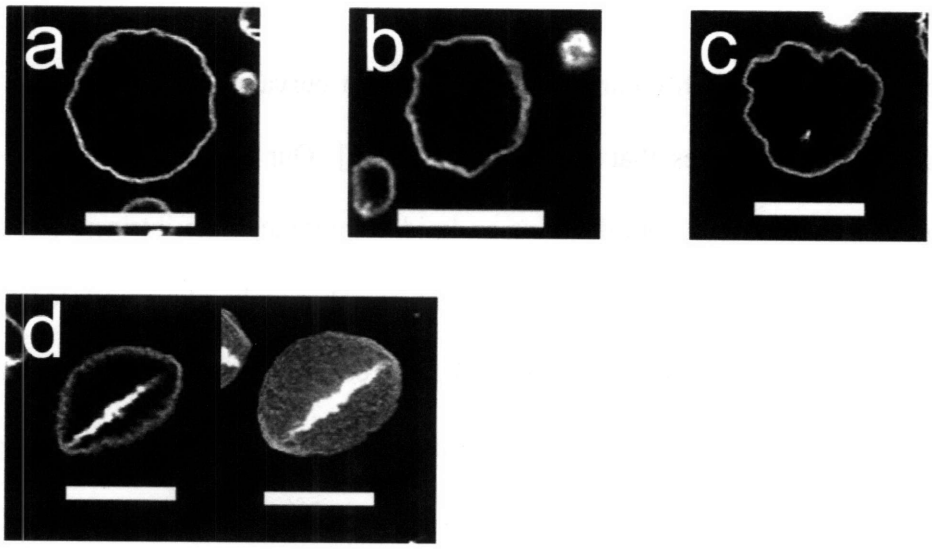

Figure 4-8. Confocal fluorescence micrographs of streptavidin-coated GUVs labeled with 0.1 mol % TR-DPPE subjected to osmotic stress gradients. (*a-c*): Equatorial sections of GUVs at (*a*) *ΔOsm*=100 mOsm, (*b*) 200 mOsm and (*c*) 300 mOsm, illustrating the highly curved wrinkles in the vesicle lipid bilayer. (*d*): Equatorial section (*left*) and projection image (*right*) of a GUV with *ΔOsm*=200 mOsm. The equatorial image is taken at a depth of 2.5 μm into the GUV with approximate dimensions 14 μm × 12 μm, length × z-depth. The fold extends 4 μm into GUV. Scale bars are 10 μm.

Osmotic deflation experiments also allow us to investigate how protein coatings on lipid bilayers influence topological membrane transformations such as budding. Our microscopy data suggest that the overall surface area of the protein-coated membrane is conserved despite osmotic deflation and that membrane budding at high osmotic stress is suppressed by the streptavidin crystals. In contrast, proteins with high intrinsic curvature

that coat lipid membranes can assist in membrane budding [19, 22]. Clathrin protein assembles in pits that form detaching buds for cell endocytosis. The lattice formed by the clathrin proteins is highly curved and this protein curvature determines the size of the budded internal vesicles that are formed [24, 25]. Our osmotic deflation experiments suggest that tethered protein domains on lipid membranes with intrinsic curvature lower than the membrane curvature can prevent membrane budding and locally increase membrane rigidity. A third category of disordered protein coatings is avidin, which we show prevents budding under moderate osmotic stress of ΔOsm=250 mOsm (Figure 4-7, *d, right column*). The mechanism of how non-crystalline avidin suppresses budding is unclear. The general question of how disordered protein coatings affect lipid curvature is important in cells, however, as diverse protein species reside in the membrane.

Osmotically-stressed streptavidin-coated vesicles present a crumpled shape, with small regions of very high membrane curvature that may be expected to affect the integrity of the lipid bilayer. To investigate this, we study the retention of a small molecule chromophore encapsulated in the vesicles. The retention or leakage of an encapsulated dye indicates whether the bilayer is porous, ruptured or torn. Figure demonstrates how the protein-coated lipid bilayer resists rupture and leakage under osmotic stress. The retention of fluorescein sodium salt (hydrodynamic radius R_H~0.5 nm) within the vesicles coated with protein (Figure 4-9, *a-c*) indicate that no nanometer-sized holes form in the bilayer even under significant osmotic stress of ΔOsm=500 mOsm (Figure 4-9, *c*). Even after 12 h, the protein-coated GUVs retain the dye with no leakage measured by fluorescence. Bare vesicles (Figure 4-9, *d* and *e*) retain the dye and resist

rupture upon osmotic stressing of ΔOsm= 250 mOsm (Figure 4-9, *e*). Interestingly, at osmotic stress gradients greater than 300 mOsm, no bare GUVs remain in the sample due to membrane collapse and rupture. We verify this effect in experiments with GUVs containing fluorescently-labeled lipid subjected to osmotic stress gradients. The stability of protein-coated GUVs compared to bare unstable GUVs at ΔOsm=500 mOsm indicates that the crystalline protein layer protects the membrane. Crystalline proteins on bilayers in nature may protect primitive organisms. S-layers on the surface of archea and bacteria are crystalline protein coatings that are linked to the plasma membrane [30]. A possible function attributed to S-layers is protection of the archea. Our findings are consistent with previous studies suggesting that S-layers stabilize model membranes subjected to mechanical stress [55].

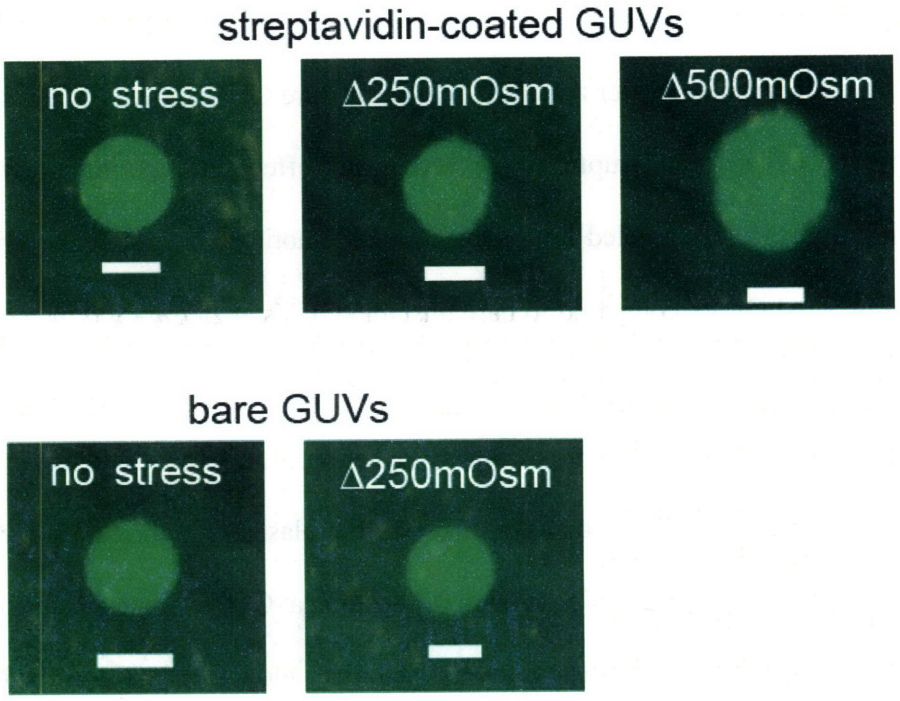

Figure 4-9. Fluorescence micrographs of GUVs encapsulating fluorescein. *Top row*: GUVs incubated in streptavidin protein solution. *Bottom*: GUVs lacking protein coating. No bare GUVs are observed at ΔOsm=500 mOsm. Scale bars are 10 μm.

We also study the retention and leakage of 10,000 MW Texas Red-Dextran, which has a hydrodynamic radius (R_h) of ~2 nm and is therefore approximately four times larger than fluorescein (R_h ~0.5 nm). We observe, however, after diluting the Dextran-filled GUVs and coating them with streptavidin, that excess Dextran adsorbs to the streptavidin layer on the outside of the GUVs. The adsorbing effect is seen in fluorescence micrographs after 12 h under osmotic stress in Figure 4-10. The adsorption of Dextran to the streptavidin coating prevents us from determining if Dextran remains inside of the GUVs or leaks from the GUVs. Because Dextran is larger than fluorescein

and would require larger tears or holes to leak from the GUVs, we do not expect leakage of Dextran from osmotically-stressed GUVs. Interestingly, without the streptavidin coating and this adsorption effect, we observe that Dextran has a stabilizing effect on bare membranes. Uncoated GUVs filled with Dextran resist rupture up to osmotic stress gradients of ΔOsm=500 mOsm (Figure 4-10, *bottom, right*), indicating that the Dextran-filled GUVs are more stable than bare GUVs, which rupture at ΔOsm= 300 mOsm.

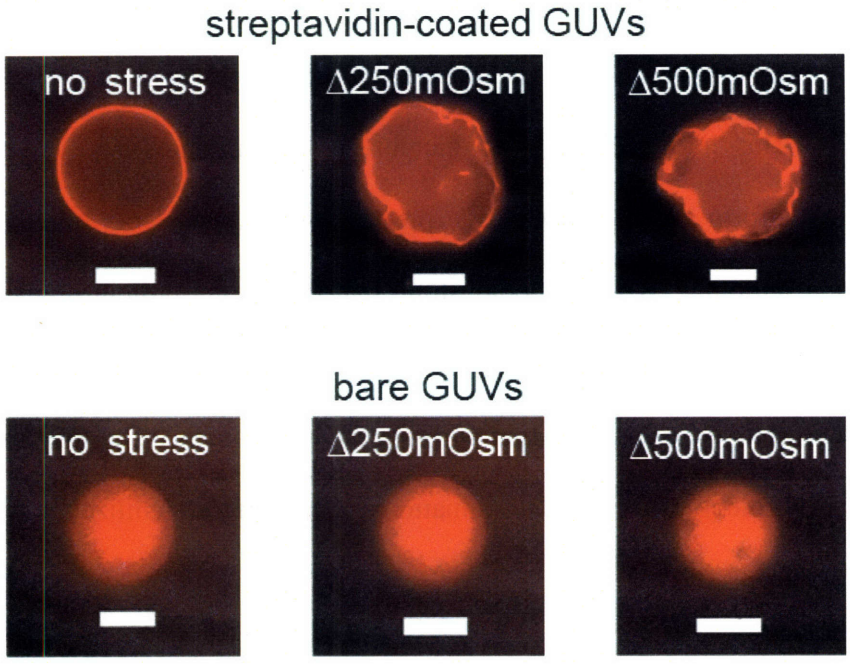

Figure 4-10. Fluorescence micrographs of GUVs encapsulating 10,000MW Texas Red-Dextran. *Top row*: GUVs incubated in streptavidin solution; Dextran adsorbs to streptavidin coating, *Bottom*: GUVs without protein coating; Dextran stablizes GUVs at ΔOsm=500 mOsm (*bottom, right*). Scale bars are 10 μm.

4.4 Conclusions

Understanding the physical mechanism of the assembly and ordering of proteins on the lipid bilayer and their effect on the membrane curvature gives insight into the biophysical processes of membrane bending and cell shape changes. Our system of streptavidin crystallized on GUVs containing biotinylated lipid illustrates how a coating of ordered protein domains can change the physical properties of the membrane. We demonstrate that the configuration of the proteins on the lipid membrane surface determines the shape of the GUVs, as aligned domains resist bending preferentially in one direction. This model biological membrane system provides an interesting experimental platform for studying the physical phenomena of two-dimensional percolation and jamming. We also demonstrate that crystalline protein domains on the GUV surface prevent vesicle budding and protect the lipid bilayer from rupture or leakage upon osmotic deflation. Our findings suggest that proteins on cellular membranes play an important role in cell shape determination and membrane stabilization.

CHAPTER 5. PROTEIN ORDERING ON SUPPORTED LIPID BILAYERS

5.1 Introduction

Self-assembled protein complexes in cell membranes have diverse functions, including structural membrane deformation [19, 20] and transduction of external signals [21]. These complexes can be peripherally attached to the membrane or imbedded in the lipid bilayer; the nature of this physical arrangement can impact overall membrane structure and fluidity. An important biological function attributed to membrane-associated proteins and protein complexes is to directly influence the membrane structure and fluidity through lipid bilayer modification or rearrangement. To better understand the biological activity of proteins in cell membranes, it is therefore essential to study proteins interacting with lipid membranes.

Microscopic and nanoscopic structural studies of protein complexes at membrane surfaces of lipid membranes offer complementary insight into protein-lipid interactions. Fluorescence microscopy can be used to measure the mobility of lipids and demonstrates that proteins bound to lipid bilayers can moderate lipid fluidity [18]. Lipid mobility likewise influences protein complex formation; microscopy investigation of the growth of

two-dimensional crystals of the tetrameric protein streptavidin suggests that immobile lipids hinder formation of protein crystals [61]. At the nanoscale, measurement techniques employing X-ray and neutron sources provide detailed structural information that can elucidate the role of proteins in the modification and rearrangement of biological interfaces. For example, reflectivity measurements reveal that the membrane-targeting domain of the peripheral protein cPLA-αC2 displaces water molecules around lipid headgroups to facilitate membrane attachment and ligand binding [60]. Other studies show that single layers of crystalline protein intercalate lipids, resulting in lipid headgroup rearrangement [58, 59, 127]. In these X-ray and neutron reflectivity examples, monolayers provide the model interface for studying surface proteins.

Experimental accessibility traditionally guides the choice of biomimetic lipid interface used to study protein-lipid interactions at micro- and nanoscales. While monolayers at the air/water interface are the most common biomimetic interface used for X-ray and neutron reflectivity studies, they are not as representative of cell membranes as a single lipid bilayer in the liquid phase. Stacks of multilamellar lipid membranes mimic the fluidity of cellular membranes and provide signal amplification for X-ray analysis [128]; however, the stacked geometry complicates study of membrane surface-associated protein complexes. The base structure for all cell membranes is a single lipid bilayer, often mechanically coupled to a cytoskeletal matrix, which can be approximated experimentally by a supported lipid bilayer (SLB) [36]. Reflectivity characterization of a single SLB requires a sufficiently flat substrate, optimized contrast and minimal beam damage. Neutron reflectivity offers the advantage of high contrast and little beam

damage; however, X-ray reflectivity at lipid interfaces offers superior resolution [38]. We extend recent developments to resolve single SLBs with X-ray reflectivity [37, 38, 68, 129] to study the more complex system of proteins interacting with single SLBs at both microscopic and nanoscopic scales.

We study the proteins streptavidin and avidin bound to biotinylated lipids to model peripheral membrane proteins at cell membranes. We prepare large (~cm^2) symmetric biotinylated SLBs and study them in a microfluidic device [37] that enables simultaneous *in-situ* investigation with X-ray reflectivity and fluorescence microscopy. Streptavidin forms 2D crystals visualized among fluorescent Alexa488-conjugated avidin, which binds to the membrane but does not crystallize [61]. By using different ratios of streptavidin to avidin, we tune the amount of crystalline vs. non-crystalline protein to examine the influence of protein ordering on the mobility of the underlying lipid membrane. Previous X-ray and neutron reflectivity characterization of the structure of streptavidin bound to lipid monolayers [127] allows us to compare bilayer and monolayer interfaces and, in particular, the structural effect of the protein on the underlying lipid interface. In addition to structural study, stable SLBs at the solid interface have potential biosensing and lab-on-a-chip applications, where a single membrane directly coupled to a surface can be used for measurement and analysis.

5.2 Materials and Methods

We purchase SOPC from Avanti Polar Lipids. The lipids biotin-X-DPPE and TR-DPPE and the proteins Alexa488-avidin, streptavidin and egg white avidin are obtained from Invitrogen (Karlsruhe, Germany). We purchase from phosphate buffered saline (0.01 M PBS; pH=7.4; 138 mM NaCl, 2.7 mM KCl, 10 mM Na_2HPO_4, 2 mM KH_2PO_4) from Sigma. We prepare the buffer in de-ionized (DI) water from Millipore Corp. (Billerica, MA). HPLC-grade chloroform, acetone, isopropanol and ethanol are from Carl Roth (Karlsruhe, Germany). We purchase reagent-grade NH_4OH, 37% HCl and H_2O_2 from Sigma.

Silicon substrates are cleaned as described in Chapter 2. We prepare the lipid mixture 89.5 mol % SOPC, 10 mol % biotin-X-DPPE and 0.5 mol % TR-DPPE in chloroform. We evaporate the chloroform and re-dissolve it in isopropanol for spin-coating. We spin-coat the lipids onto the substrate, dry the film, secure the substrate into a microfluidic device and hydrate the SLB according to our protocol outlined in Chapter 2. We rinse the SLBs in microfluidic chambers five times with PBS buffer, then pipette 1 mL of protein solution in PBS at concentration 40 μg/mL into channels to allow protein layers to form on the SLBs. The SLBs are left undisturbed to incubate in protein mixtures at least 12 h at 30°C. After forming the protein layer, the chambers are rinsed out to remove excess proteins.

Both fluorescence microscopy and X-ray reflectivity measurements are performed at the undulator beamline ID01 at the European Synchrotron Radiation Facility (ESRF) in Grenoble, France. The X-ray geometry and setup and the microscope apparatus are described in Chapter 2.

5.3 Results

5.3.1 Fluorescence Microscopy

After incubating the SLBs in protein and flushing the chambers to remove proteins in solution, fluorescence microscopy provides direct evidence of protein layer formation. Dark crystalline streptavidin domains are visualized among fluorescently-labeled avidin in Figure 5-1. Qualitative observation of the protein crystals in Figure 5-1 gives insight into the overall quality and fluidity of the SLBs. The surface coverage of the streptavidin clearly increases as the amount of streptavidin in the incubation solution is increased. Streptavidin crystals in Fig 5-1, *II* and *III* exhibit the characteristic X- and H-shapes of crystals with C222 symmetry observed on monolayers formed in the presence of bound avidin at similar solution conditions [63, 130, 131]. The nucleation of microscopic protein crystals requires mobile lipids and a smooth substrate [61] and the uniform size and random orientations of the streptavidin crystalline domains at each protein composition suggest that SLBs have uniform fluidity. At low microscopic resolution (Figure 5-1, *left column*), the density of the crystals on the SLB is spatially

uniform, suggesting that the nucleation density and crystal domain growth rates are constant across the SLB.

Crystalline domains at lower streptavidin surface coverages (Figure 5-1, *II* and *III*) have an average length of ~15 μm and an average length to width aspect ratio of ~2. Characterizing the shapes of the streptavidin domains formed from 90 wt % streptavidin solution is more difficult, as the domains grow to near confluence (Figure 5-1, *I*). Previous experiments in monolayers [131, 132] and bilayers [61] also suggest that high surface coverage of streptavidin enables dendritic growth of crystals, resulting in morphologically-indistinguishable domains.

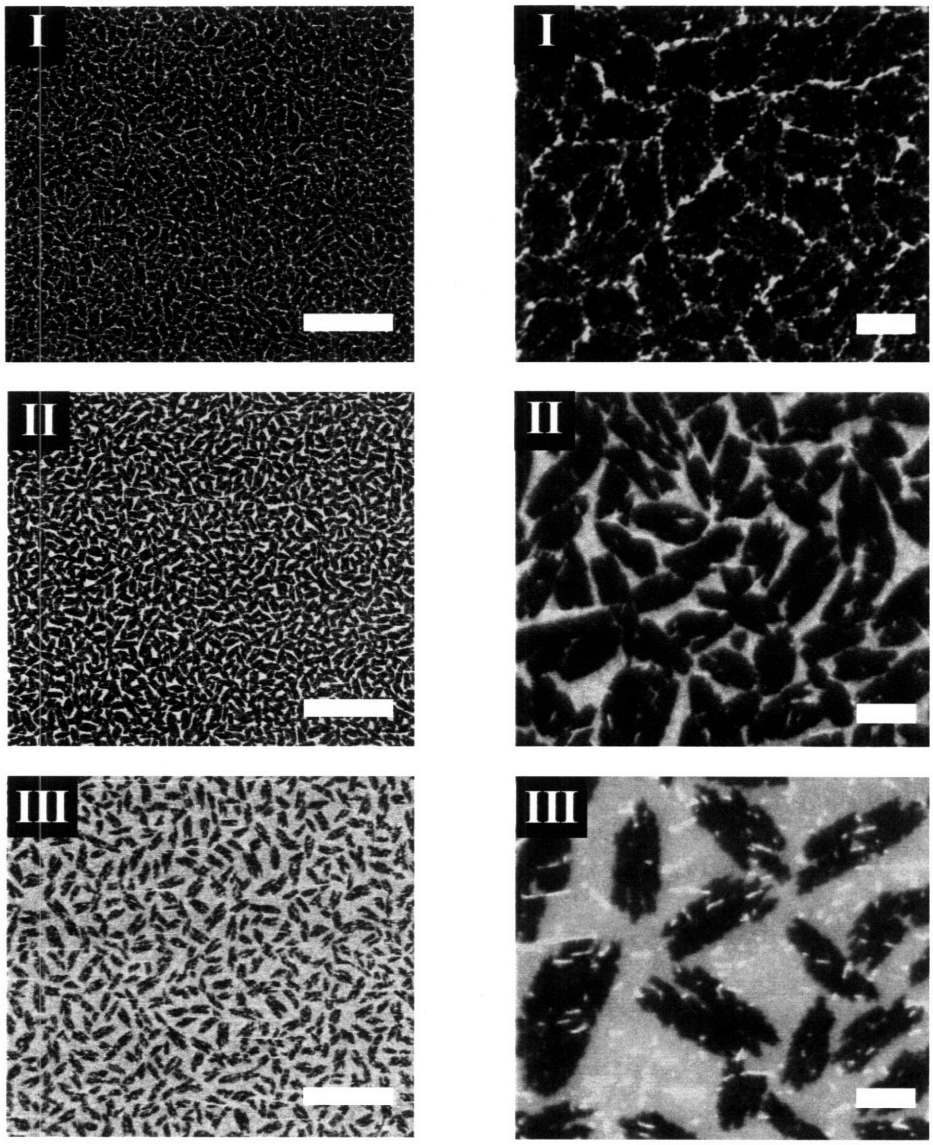

Figure 5-1. Dark crystalline streptavidin domains bound to SLBs imaged with 10× (*left column*) and 63× (*right column)* objectives. SLBs are incubated in protein mixtures of molar ratios (streptavidin/avidin/Alexa488-avidin) of (*I*) 92/0/8, (*II*) 56/36/9, and (*III*) 12/78/10. Scale bars are 100 μm in the left column, 10 μm in the right column.

5.3.2 Continuous Bleaching

While the formation of microscopic crystalline domains indicates that our membranes are fluid, we also quantitatively measure the diffusion constants of lipid bilayers with and without protein. We use the continuous bleaching method [67, 81], which is particularly convenient because it employs the same setup we use for fluorescence microscopy. According to the theory of continuous bleaching, the spatial intensity of fluorescently-labeled membrane subjected to constant and even illumination is described by simultaneous photobleaching and replenishment of fluorescent molecules via two-dimensional diffusion.

We illuminate a defined region of the SLB ~180 μm in diameter (d) at 63× magnification (Fig 5-2, *a, right*). This area is continuously illuminated and, as the fluorescent lipid molecule TR-DPPE is photobleached, the fluorescence intensity, $I_{d/2}$, of the SLB in the center of the illuminated area ($d/2$), decays exponentially as a function of exposure time (t) according to the equation:

$$I_{d/2}(t) = I_{t0}e^{-B_0 t} = I_{t0}e^{-\tau} \qquad (5\text{-}1).$$

I_{t0} is the initial fluorescence intensity at the center of the illuminated area, B_0 is the bleaching rate and τ is dimensionless time, $\tau = B_0 t$. We calculate I_{t0} from the average intensity of an area of ~10 μm in diameter in the center of the sample, represented by circles in the SLB micrographs of Figure 5-2, *a*. The total fluorescence intensity

measured in the center of the sample, $I_{total,d/2}$, is the sum of $I_{d/2}$ and the background fluorescence measured in the non-illuminated part of the membrane, A_1, and $I_{total,d/2} = I_{d/2} - A_1$. We calculate B_0, which depends on the fluorescent dye, solution conditions and illumination energy, by fitting Equation 5-1 to the time-resolved intensity in the center of the sample for each continuous bleaching measurement. The plot of $I_{d/2}$ as a function of time is presented in Figure 5-2, *b* and the dashed line calculated from Equation 5-1 illustrates that the first-order behavior described by Equation 5-1 persists up to ~1000 s. At longer times, the fluorescence intensity measured at the center of the membrane approaches the background fluorescence A_1, indicating that the center of the membrane is fully bleached.

As the sample is bleached, a bright rim appears at the edge of the image (Figure 5-2, *a, bottom right*), as TR-DPPE molecules diffuse into the illuminated area. Once the center of the sample approaches the background fluorescence and remains constant, at approximately $\tau > 20$, we fit the fluorescence intensity line profile through the sample as a function of distance, x, according to the equation [81]:

$$I(x) = I_{x0} \cosh\left(\sqrt{B_0/D}(x - d/2)\right) + A_2 \qquad (5\text{-}2).$$

The fluorescence intensity at the edge of the rim is I_{x0}, D is the diffusion constant and A_2 is a constant we use to fit Equation 5-2 [81]. Diffusion constants extracted by fitting Equation 5-2 to the line profiles at 5 s intervals are plotted in Figure 5-2, *c*. The fit of Equation 5-2 to a line profile is shown in Figure 5-2, *a*. According to the original

development of continuous bleaching theory, Equation 5-2 can only be used to accurately calculate D at longer times, when the center of the sample is completely bleached [81]. This time regime is indicated in Figure 5-2, *c* and is represented qualitatively by the plateau of extracted D values at $\tau > 20$. For data suitable for robust quantitative analysis, extra care must be taken to ensure even sample illumination and a flat initial line profile (Figure 5-2, *a*) and the center of the sample must be completely bleached to the background level to calculate the diffusion constant D.

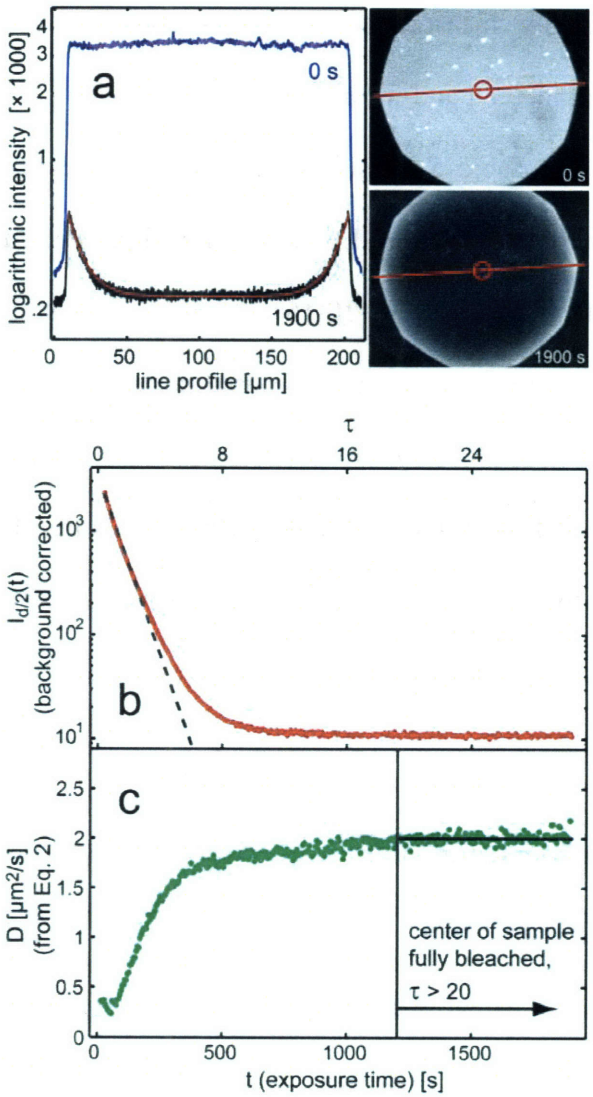

Figure 5-2. Continuous bleaching of TR-DPPE to measure lipid diffusion in a SLB coated with protein layer of 92/8 molar ratio (streptavidin/Alexa488-avidin). (*a*): Line intensity profiles and corresponding micrographs at the onset of bleaching (0 s) and end of the experiment (1900 s). The fit to the line profile at 1900 s from Equation 5-2 is shown in red. (*b*): The plot of background-corrected fluorescence intensity in the center of sample as a function of time is used to determine the bleaching rate B_0; the dashed line is calculated from Equation 5-1. (*c*): Diffusion constant *D* extracted from fitting line intensity profiles at 5 s time intervals to Equation 5-2. The longer time regime ($\tau > 20$) is indicated when the center of the sample is fully bleached and Equation 5-2 is valid for calculating *D*.

We reproducibly measure the diffusion constants of our SLBs using the continuous bleaching method and we investigate whether the protein layer influences the fluidity of the bilayer. Table 5-1 lists the lipid diffusion constants of the SLBs. We measure that protein binding to the SLB results in a slight decrease in lipid mobility, as lipid diffusion constants are reduced ~10-15% when a protein layer is present. Neither the composition of the protein mixture nor the area coverage of crystalline protein has a measurable effect on lipid mobility. Previous studies of multivalent polymers adsorbed to lipid bilayers at complete surface coverage also show little effect on measured lipid diffusion compared to bare bilayers [133]. After bleaching, the SLBs recover to their full original fluorescence overnight and we are unable to detect an immobile fraction of lipids.

Composition of protein solution	Diffusion constant, D ($\mu m^2/s$)
no protein (bare SLB)	2.3 ± 0.4
90 wt % streptavidin, 10 wt % avidin	2.0 ± 0.1
50 wt % streptavidin, 50 wt % avidin	1.9 ± 0.1
10 wt % streptavidin, 90 wt % avidin	1.9 ± 0.1
100% avidin	2.0 ± 0.1

Table 5-1. Diffusion constants calculated by fitting Eqs. 5-1 and 5-2 to continuous bleaching data. SLBs are incubated in protein solutions with compositions listed; total mol % avidin comprises ~5 mol % Alexa488-avidin and the balance egg white avidin. Three different time-resolved line profiles are measured for every sample, each corresponding to N > 20 calculations of *D*. Error is estimated as the experimental standard deviation.

We also investigate whether the protein molecules within the protein layers attached to the SLBs are mobile by using fluorescently-labeled avidin as a tracer molecule. When we continuously illuminate protein-coated SLBs at 488 nm, corresponding to the Alexa488-avidin, we do not observe the bright rim at the sample edge characteristic of a fluid membrane. Instead, the illuminated area, viewed at 10× after 1 h of bleaching and shown in Figure 5-3, has a sharp outline and a flat fluorescence intensity profile, indicating no diffusion of the Alexa488-avidin. Note that due to the high photostability of the Alexa dye, there is only minimal bleaching of the protein layer. This immobility is observed at all protein layer compositions and time-resolved images show that the streptavidin domains remain fixed, further indicating the immobility of the protein layer.

We expect the diffusion constant of the bound protein to be lower than that of the underlying lipids, by comparison of the relative molecular sizes of a lipid molecule (~7 Å) and a single protein molecule (~50 Å) [134]. The molecular size-scaling of the diffusion constant in a SLB is not accurately described by the hydrodynamic model of diffusion [118] that we use to describe protein complexes in fluid lipid bilayer vesicles [135] due to frictional contact between the lipids and the solid substrate [136]. Due to the bivalent attachment of the protein molecules to the lipids, each protein molecule must diffuse with two lipid molecules separated by a fixed distance; as multivalent streptavidin crystalline complexes form, an increased number of bound lipids must diffuse with fixed spacing. The mobility of the non-crystalline protein molecules can also hindered by collisions with adjacent proteins at our experimental condition of high protein surface

coverage. Previous observations show that proteins attached to membranes at high surface coverages can diffuse 20-100 times slower than lipids [131]. We can therefore expect the streptavidin and avidin to be fixed and immobilized relative to the underlying lipids not attached to the protein at our experimental conditions of high protein surface coverage.

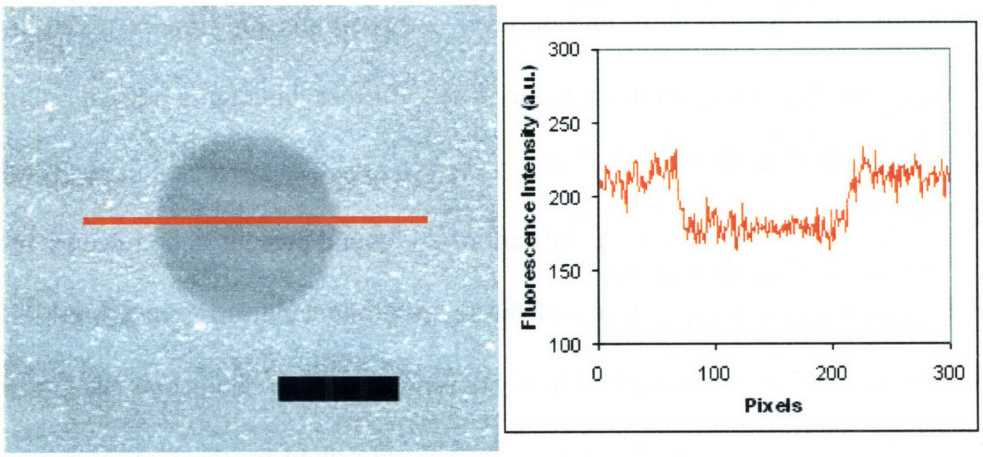

Figure 5-3. After continuous fluorescence illumination of SLB coated with 92 mol % avidin, 8 mol % Alexa488-avidin at 488 nm for 1 h, no diffusion of Alexa488-avidin is detected. The bleached region is clearly outlined (*left*) and the line intensity profile indicates uniform fluorescence across the bleached region. Scale bar is 100 μm.

5.3.3 X-ray Reflectivity

X-Ray reflectivity enables us to determine the structure of the protein and underlying bilayer in nanoscopic detail. In Figure 5-4, we compare the reflectivity of bare and protein-coated membranes. The main signature of the protein layers in Figure 5-4, *I-III* is the dip in the reflectivity curve at $q_z = 0.1$ Å^{-1}, indicating an additional layer on the lipid bilayer membrane, which is not present in scans of the bare membrane (Figure 5-4, *IV*). From initial observation, the reflectivity scans from the different protein layer compositions shown in Figure 5-4, *I-III* are nearly indistinguishable. The similar reflectivity from different ratios of avidin and streptavidin are not surprising, as avidin and streptavidin have similar structures [137]; 33% of the residues are the same [65] and their biotin-binding sites are nearly identical. This structural similarity, combined with the fact that our reflectivity scans are measured with an incident beam on the membrane of size ~1 mm^2, make avidin and streptavidin indistinguishable by our measurements. Thus, our X-ray reflectivity fits do not take into account the segregation of the proteins once crystals are formed.

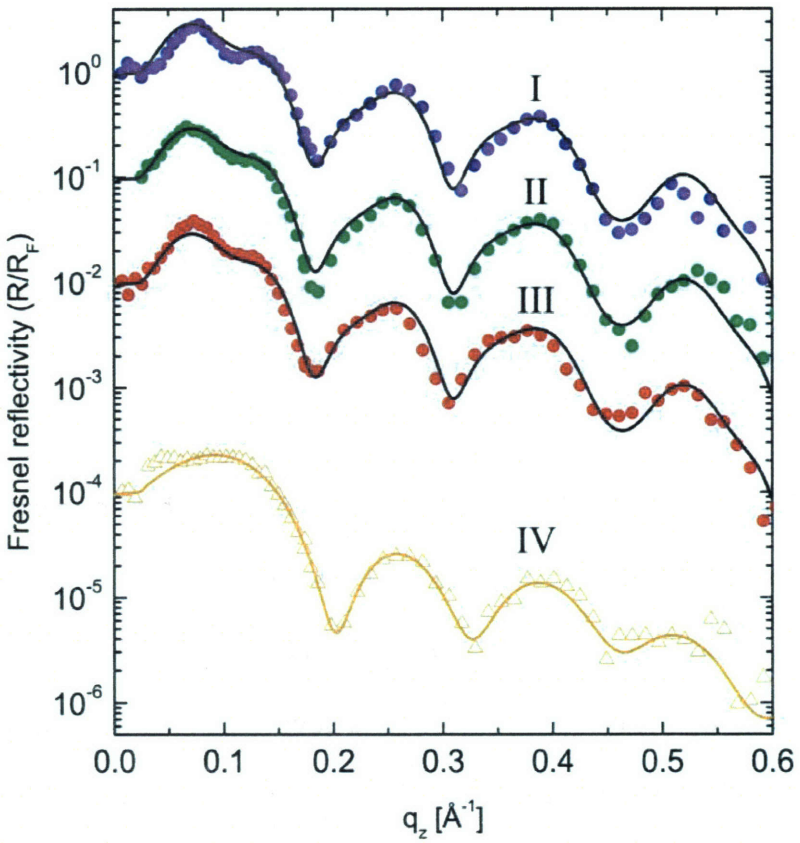

Figure 5-4. Normalized reflectivity scans of protein-coated (*I-III*) and bare (*IV*) SLBs. Protein-coated SLBs (*I-III*) have a signature dip at q_z = 0.1 Å^{-1}. SLBs coated with protein mixtures with molar ratios (streptavidin/avidin/Alexa488-avidin) of (*I, blue*) 92/0/8, (*II, green*) 56/36/9, and (*III, red*) 12/78/10. The common depth profile is plotted with the data sets in *I-III* to illustrate the similarity of the streptavidin and avidin-protein layers. The reflectivity of a bare SLB lacking protein (*IV*) is shown with its fit (*orange curve*). Plots are shifted vertically for clarity; all data are background corrected and normalized by the Fresnel reflectivity, R_F.

To extract structural details of the protein layer and underlying SLB, we fit the X-ray reflectivity data using a least-squares fitting routine. We use an 11 slab model for the protein-coated SLBs; the thickness and electron density for each slab is varied to fit the raw data [85]. We model the underlying SLB with 7 slabs: 2 slabs for each headgroup

layer, one slab for each acyl chain layer and one slab for the space between leaflets. The region between the bottom of the peripheral protein layer and the upper surface of the SLB is one slab and we use 3 slabs to model the protein layer. This slab model profile is smoothed by an overall roughness of 3 Å, as described in Chapter 2. We test the structural similarity of protein-coated SLBs formed from different compositions of streptavidin and avidin by fitting the data to a single depth profile. The fit to this common profile is plotted with the data at each protein composition in Figure 5-4, *I-III*.

In Figure 5-5 we present the electron density profiles of protein-coated and bare SLBs, with a corresponding sketch of the peripherally-bound protein. The common depth profile of the protein-coated SLB is shown; thus, this profile represents both streptavidin and avidin in the protein layer (Figure 5-5, *black curve*). The protein layer attached to the bilayers is indicated by the characteristic increase in electron density, at distance of 55-95 Å from the substrate. In contrast, the electron density profile of the bare SOPC/biotin-X-DPPE SLB is flat in this region (Figure 5-5, *orange curve*). We measure a ~40 Å-thick protein layer on the SLB. This thickness is comparable to previous X-ray and neutron reflectivity studies of streptavidin crystallized on monolayers, where thicknesses of 40-44 Å [57, 127, 138] are reported, which is near the thickness of avidin measured by X-ray crystallography of ~40 Å [137]. Our dynamical range extends up to $q_{max} = 0.6$ Å^{-1} and the spatial resolution of the electron density profile, d_{min}, is estimated by the sampling theorem as $d_{min} \sim \frac{\pi}{q_{max}}$ [129]. According to this relation, our resolution is d_{min}~5 Å. We are therefore able to resolve the space between the protein and SLB, which is ~8 Å in

thickness. This hydrated layer is structurally distinct from the headgroups and protein because the electron density in this space approaches the bulk water density. To verify the structural similarity of protein layers with different amounts of avidin and streptavidin, we also independently fit the scans for each protein composition, allowing the thickness and density of each slab to vary. As expected, the individual profiles extracted from the reflectivity of different streptavidin and avidin protein layers are identical within the precision of our measurements.

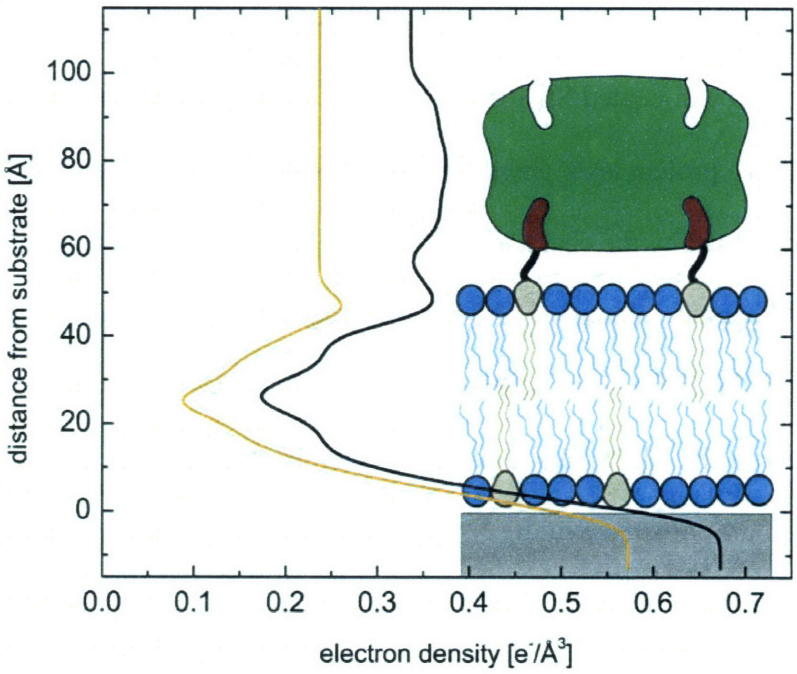

Figure 5-5. Electron density profiles of SLBs with a protein layer (*black, common profile*) and without protein (*orange*) extracted from fitting the reflectivity. The protein layer is identified by a plateau of increased electron density not seen on the bare SLB (*orange*). The thickness of the protein layer is ~ 40 Å; the water layer separating the protein from the SLB is ~ 8 Å thick. The electron density axis is correctly aligned for the protein-coated SLB (*black*); the profile of the bare SLB (*orange*) is shifted left for clarity.

5.4 Discussion

We create large stable arrays of protein crystals on single supported lipid bilayers suitable for simultaneous microscopy and reflectivity characterization. Our protein-coated SLBs remain stable for characterization over 48 h. In developing a biomimetic interface for studying protein complexes, we require bilayer stability for time-resolved investigation of biological self-assembly at interfaces. Also, large surface coverage of the bilayer becomes important, as both reflectivity and microscopy require homogeneous samples of dimension ~100 μm^2. Fluorescence microscopy micrographs (Figure 5-1) provide direct evidence of protein layer formation and high surface coverage.

Using the complementary insight from our combined microscopic and nanoscopic characterization of protein-coated membranes we can describe how the protein layer interacts with the lipid in greater detail. The high resolution that we accomplish with X-ray reflectivity allows us to examine the structure of a single layer of protein on a SLB. Since streptavidin and avidin irreversibly bind the headgroups of biotin-X-DPPE lipids and are immobile relative to the lipid molecules, we expect the lipids bound to the tethered protein layer to be immobilized. We approximate the number of pinned lipids in the bilayer by estimating the number of lipid molecules per protein molecule. If the approximate area per lipid headgroup is 50 $Å^2$ and the protein molecules are $\approx 50 \times 50$ $Å^2$ in area, then the footprint of the protein is ~50 lipids. Bivalent binding of the protein then suggests that 4 mol % of the lipids are pinned. The slight decrease in the lipid diffusion

constants determined by continuous bleaching experiments, where binding of the protein reduces the diffusion constant of the lipid probe by ~10-15%, suggests that pinning of biotinylated headgroups due to protein layer binding and the presence of a solid protein layer above the membrane can influence membrane fluidity.

Despite the immobilization of the biotinylated lipids, the SLB is fluid and is viscously decoupled from the protein layer. We attribute this to the space between the SLB and protein layer that we measure with X-ray reflectivity. The molecular contents of this layer are water and the portion of the biotin-X-DPPE separating the biotin from the headgroup. The main protein-lipid interaction that we resolve in our structural study of streptavidin and avidin binding to SLBs is therefore immobilization of biotinylated lipids bound to protein. These observations contrast the effects observed upon streptavidin layer formation on monolayers at the air/water interface. The lipids show major tilting, and rearrangement, resulting in overall reduced monolayer thickness [127]. Stable lipid bilayers resist leaflet collapse and, unlike lipid monolayers, cannot easily adjust surface pressure and density in response to ligand binding. We suggest that lipid bilayers are more representative of cell membranes and more appropriate for studying protein-lipid interactions than monolayers, as we expect the lipid spacing in cells to also be somewhat fixed.

Interestingly, the fluidity and structure of lipid bilayers with non-crystalline avidin and microscopic crystalline streptavidin domains are similar. Both protein coatings are qualitatively immobile or frozen and cause the same slight decrease in the fluidity of the underlying lipids. While we would expect non-crystalline avidin to be more mobile

than streptavidin molecules confined to crystalline domains, in our model of lipid pinning, all bound protein molecules are immobilized relative to the viscously decoupled underlying SLB.

5.5 Conclusions

We concomitantly characterize a single protein layer bound to a single SLB with fluorescence microscopy and X-ray reflectivity. In this protein template, streptavidin and avidin are specifically bound to a fluid interface with defined orientation, which may be superior to simple solid-supported protein interfaces for biosensing applications. We demonstrate a method of characterizing proteins interacting with single lipid bilayers at the solid interface; this biomimetic membrane is more representative of cell membranes than monolayers and can be extended to study more complex protein-lipid interaction systems. By resolving the space separating the streptavidin and avidin layers from the SLBs, we demonstrate that the lipid-protein interaction is peripheral, contrasting the leaflet collapse effects observed from similar molecules in lipid monolayers. Our study suggests that proteins in general can have different effects at monolayers and bilayers.

CHAPTER 6. GM1 GANGLIOSIDE AND MODEL LIPID RAFTS IN SUPPORTED LIPID BILAYERS

6.1 Introduction

The monosialoganglioside receptor GM1 is the entry point for the protein cholera toxin at the cell membrane surface. The B subunit of cholera toxin (CTB) binds sugar oligosaccharide groups of GM1 that extend out from the surface of the membrane [139]. Once CTB is bound, five GM1 molecules per CTB form a pentagonal complex [140] that allows the toxin to cross the membrane into the cell to induce disease [16]. The lateral diffusion of GM1 in the membrane and its co-localization with other GM1 molecules to form the CTB-GM1 complex is therefore a vital step in the delivery of cholera toxin to cells. A possible mechanism for concentrating GM1 molecules is the preferential partitioning of GM1 into different lipid environments of the cell. CTB entry into the cells can be facilitated by binding GM1 receptors concentrated in cell membrane domains that are enriched in sphingolipids, cholesterol and the protein caveolin-1 [16]. In model biological membranes, GM1 localizes to liquid-ordered lipid phases [4, 141], though other studies suggest that GM1 localization to model lipid rafts requires CTB binding [9, 17]. A better understanding of the influence of GM1 and the GM1-CTB complex on the

local lipid packing of the cell membrane could clarify why GM1 prefers certain lipid phases.

Surface-sensitive techniques for characterizing lipid interfaces suggest that GM1 can moderate lipid packing. GM1 itself diffuses more slowly than the surrounding lipids and the mobility of GM1 is further reduced when it binds to CTB [18, 49]; in cells, the GM1-CTB complex is immobile [142]. Fluorescence microscopy experiments demonstrate that GM1 decreases the mobility of surrounding lipids [143, 144], particularly if the surrounding lipids are near a gel phase transition [18]. One possible cause of the reduced mobility of GM1 imbedded in lipid membranes is GM1 aggregation, which is observed in lipid bilayers [145, 146], and is facilitated by CTB binding. GM1 in an aggregated form can then translocate to liquid-ordered lipid phases [9], thus relocating to a denser lipid environment. Other examples of lipid-bound molecules similarly move into denser lipid phases upon complexation [7, 8]. Additional possible mechanisms of lipid fluidity moderation by GM1 are disruption of lipid headgroup packing [147] and lateral condensation of lipid molecules [145].

Improving our understanding of this well-observed effect that GM1 is able to influence lipid fluidity in membranes requires molecular-level structural information. X-ray and neutron reflectivity studies offer the advantage of nanoscale-resolution insight into the structure of the membrane. Previous measurements of lipid monolayers with neutron reflectivity demonstrate how reflectivity can be used to gain structural information about the GM1-CTB complex interacting with lipids; complex formation may decrease the lipid density and perturbing lipid packing [147]. We aim to investigate

whether these lipid packing perturbations observed in monolayer systems persist in more biologically-relevant bilayers. We also want to compare lipid bilayers containing GM1 to those lacking the receptor to understand how GM1 alone may influence lipid packing before binding CTB. Using the experimental platform of X-ray reflectivity and fluorescence microscopy of single lipid bilayer membranes [37], we incorporate GM1 asymmetrically into fluid supported lipid bilayers (SLBs). X-ray reflectivity allows us to verify this asymmetry and to study in detail the lipid packing modification caused by GM1 insertion. We first present our studies of GM1 in homogeneous membranes, followed by investigation of GM1 in cholesterol-enriched lipid bilayers.

6.2 Materials and Methods

DOPC, cholesterol, BSM and the ovine brain ganglioside GM1 are purchased from Avanti Polar Lipids. TR-DPPE and the Alexa Fluor 488-labeled cholera toxin B subunit (CTB) are purchased from Invitrogen. All lipids are prepared in HPLC-grade chloroform, except for TR-DPPE and GM1 when dissolved in organic solution, which we prepare in 1:1 mixtures by volume of chloroform and methanol. We use the extrusion method described in Chapter 2 to prepare LUVs for experiments. When preparing LUVs with model lipid raft compositions of cholesterol/BSM/DOPC, we extrude lipids at a temperature above the lipid phase transition temperature, T_m, using the GUV lipid phase diagram for these lipid compositions as a reference to determine T_m [148]. The LUVs are used to form SLBs on SiO_2 substrates in microfluidic chambers via vesicle fusion

assisted by osmotic rupture (Chapter 2). We also use spin-coating technique to form symmetric SLBs containing GM1. The chloroform/methanol lipid solution is completely dried, re-dissolved in isopropanol, then applied to substrates with spin-coating as described in Chapter 2.

Because GM1 is an amphiphilic molecule, it can spontaneously partition into lipid vesicles in aqueous solutions [149]. We extend this technique to incorporate GM1 into pre-formed solid-supported lipid bilayers incubating SLBs for 4 h in solutions of GM1 in DI water at a concentration of 1 mg/mL. GM1 in aqueous solutions can aggregate and form micelles [150]. To investigate if there is a concentration-dependence of GM1 on SLB structure, we also incubate SLBs with GM1-enriched LUVs for 4 h. We use LUVs that have the same lipid concentration as the SLBs; to prepare GM1-enriched LUVs, we incubate LUVs with aqueous GM1. As we are unable to determine the partitioning of the GM1 into the LUVs, we calculate the stoichiometry of the combined LUV and GM1 solution; we use 1, 5 or 20 mol % GM1. We prepared and measured our samples at the ESRF ID1 beamline, with the beam characteristics described in Chapter 5, at two separate beamtimes to verify the reproducibility of our observations. For X-ray reflectivity measurements, we use the microfluidic chamber and reflectivity setup described in Chapter 2.

6.3 Results and Discussion

6.3.1 GM1 in Homogeneous Membranes

We first characterize GM1 insertion into a homogeneous fluid lipid bilayer. The fluid SOPC lipid bilayer provides a well-defined interface for understanding the structural influence of GM1 on lipid bilayer membranes. The transition temperature of SOPC is ~5°C, ensuring that it is at a stable, fluid liquid state at room temperature. We first examine GM1 insertion into fluid lipid bilayers of 99.5 mol % SOPC and 0.5 mol % TR-DPPE with X-ray reflectivity. The reflectivity scan of the SOPC membrane is shown in Figure 6-1, *a*. The oscillations are characteristic of a single fluid lipid bilayer above a solid support [37, 38]. After incubation for 4 h with excess GM1, the membrane changes significantly. Figure 6-1, *b* presents the reflectivity scans of the SOPC membrane after GM1 insertion. The most prominent effect of GM1 incorporation into the membrane is a shift in the positions of the minima. The first minimum shifts from $q_z \sim 0.2$ to 0.18 $Å^{-1}$, the second from 0.34 to 0.3 $Å^{-1}$. These shifts of the minima to a lower momentum transfer (q_z) qualitatively indicate a thickening of the bilayer.

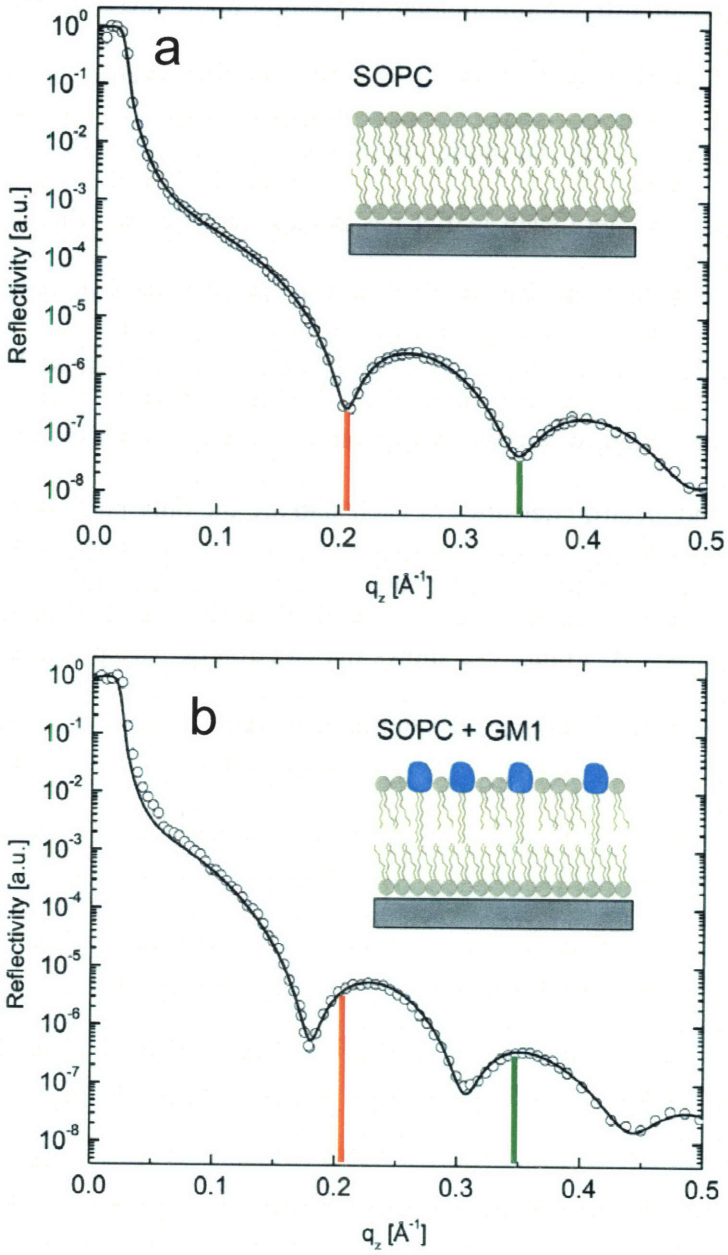

Figure 6-1. Reflectivity scans with fits for single SOPC bilayer before (*a*) and after (*b*) incubation with excess GM1. The vertical lines illustrate the shifts of the minima at $q_z \sim 0.2$ Å^{-1} (*red*) and $q_z \sim 0.35$ Å^{-1} (*green*) after GM1 insertion into the membrane.

In order to further investigate this bilayer thickening upon GM1 insertion and to determine how the leaflet dimensions are changed, we fit the reflectivity scans in Figure 6-1 using a 7 or 9 slab model [85]. To model the SOPC layer without GM1, we follow the procedure in Chapter 5, where each leaflet has 2 slabs representing the headgroups and one slab for the acyl chains; the interleaflet space is an additional slab. To account for the large oligosaccharide headgroup of the GM1, we use a 9 slab model to fit the SOPC layer after GM1 insertion, where the headgroup region of GM1 has two additional slabs. The thicknesses and electron densities of each slab are the only parameters that are varied in the fitting process, outlined in Chapter 2. The roughness of each slab for smoothing the overall fit is 3 Å. Figure 6-2 shows the electron density profiles extracted from fitting the reflectivity scans in Figure 6-1 with this model.

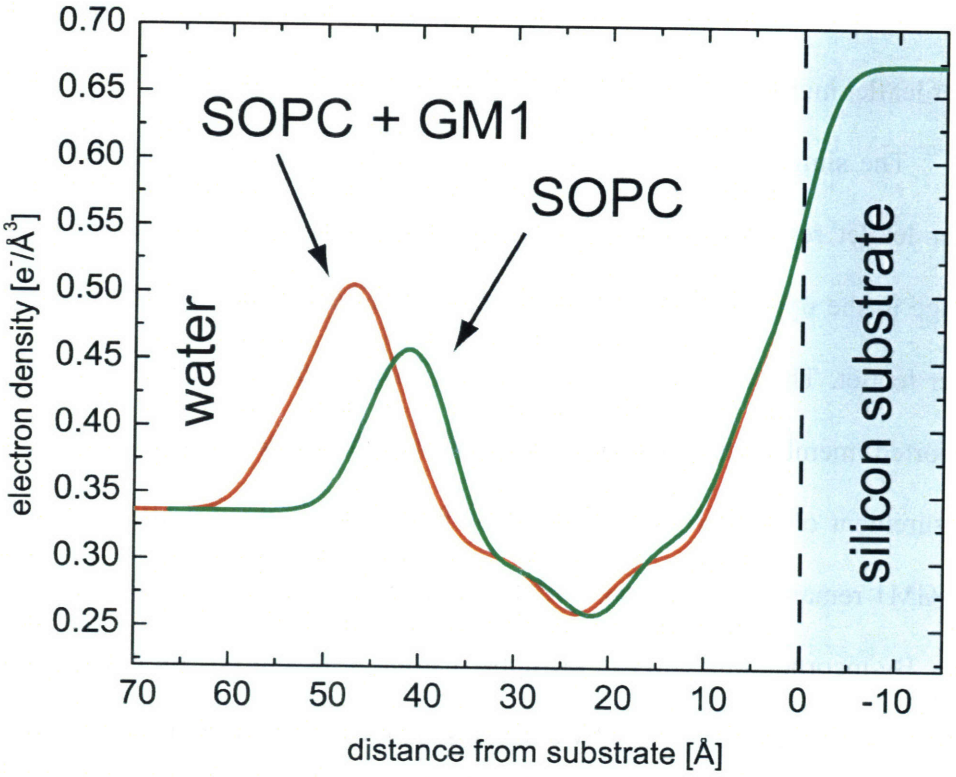

Figure 6-2. Electron density profiles extracted from the reflectivity of a SLB of SOPC before (*green curve*) and after (*red*) GM1 incorporated into the upper leaflet of the membrane.

Near the solid substrate, the electron density profiles in Figure 6-2 are nearly identical up to a distance of 20 Å. This region describes the headgroups and acyl chains of the lower leaflet of the SLB and the water layer separating the membrane from the substrate. A thickening of the upper leaflet of the membrane is clearly demonstrated by the shift of the peak corresponding to the electron-dense headgroup region of the upper

leaflet, from ~ 42 to 48 Å. Also, the overall electron density of the headgroups in the upper leaflet increases upon SOPC insertion from 0.45 to 0.5 $e^-/Å^3$.

The similarity of the profiles from Figure 6-2 of SOPC and SOPC/GM1 in the lower leaflet region of the SLB, contrasting the headgroup repositioning and density change in the upper leaflet, shows that GM1 does not affect the electron density of the lower leaflet. This result suggests that GM1 inserts only into the upper leaflet of these supported membranes and does not flip into the bottom leaflet. By repeating our measurement of the reflectivity of the SOPC/GM1 membranes after 3 days, we verify that GM1 remains in the upper leaflet, as the reflectivity does not change over this time scale. By incorporating GM1 in the upper leaflet of the bilayer, we mimic the orientation of GM1 in cell membranes and we can systematically observe the effect of GM1 on the structure of a single leaflet coupled to a supported leaflet. This method of inducing asymmetry in a symmetrical SLB may also be useful for creating layered structures on SLBs.

We have also used the spin-coating method described in Chapter 2 to prepare symmetric SLBs containing 1-2 mol % GM1 in both leaflets. Fluorescence microscopy characterization shows, however, that these SLBs are inhomogeneous, and non-uniform. This may be due to a repulsive interaction between the negatively-charged sialic acid of the GM1 headgroup and the SiO_2 substrate. It has been suggested that GM1 asymmetrically distributed in the outer leaflet of lipid bilayers may confer stability to the overall membrane [151].

The electron density profiles before and after GM1 insertion are consistent with protrusion of the GM1 headgroups above the bilayer surface, which is reported both with X-ray diffraction [152] and AFM [146]. The hydrophobic tail structure of GM1 is different than the tail structure of SOPC; both of the chains of SOPC have 18 carbon atoms, though one chain is unsaturated. The ceramide chains of GM1 are saturated; one chain is 18 carbons in length and the other chain has 15 carbons. Previous measurements indicate that GM1 can protrude above lipid headgroups at a distance of ~12 Å [152].

We observe this stretching effect of GM1 on the upper membrane leaflet of SOPC after incubating the SLBs in excess GM1 in solution. We also investigate whether these structural membrane changes depend on the amount of GM1 available in solution. To control the amount of GM1 we add to SLBs for incubation, we first prepare LUVs of SOPC enriched in GM1 by incubating the LUVs in aqueous GM1. These GM1-enriched LUVs are then used for incubating the bilayers, thus diluting the concentration of GM1 available to the membrane. In Figure 6-3, *b*, the reflectivity of an SLB after incubation with LUVs of composition 99 mol % lipid and 1 mol % GM1 is presented. There is little difference between the reflectivity of this scan and that of the SLB incubated in excess GM1 (Figure 6-3, *a*). The slab model fits to the data are nearly identical and show the same increase in the headgroup density ~ 8 Å. Since the effect of GM1 insertion is essentially the same at low and excess GM1 concentrations, we believe that GM1 incorporation reaches a saturated concentration at all of the incubation concentrations that we use.

When CTB binds five GM1 receptors, the resulting complex becomes the entry point for the entire cholera toxin protein to cross the membrane [16]. A recent study of CTB bound to GM1 in monolayers suggests that the density of the lipid leaflet is slightly decreased upon CTB binding [147]. To investigate whether this effect is observable in lipid bilayers, we measure the binding of fluorescently-labeled CTB to SOPC/GM1 membranes. CTB binding to the membrane is evidenced by fluorescence microscopy, as the membrane after incubation with CTB is bright and non-specific binding of CTB was not observed in a control experiment. Figure 6-3, *c* presents the reflectivity of a SLB with GM1 after incubation in CTB, which is nearly identical to the reflectivity from SLBs lacking CTB (Figure 6-3, *a* and *b*). Unlike the distinct increase in reflectivity that we observe in SLBs coated with streptavidin and avidin in Chapter. 5, we do not detect the bound CTB in the reflectivity. Thus, CTB does not provide enough electron density contrast to be resolved with our measurements. The low electron density contrast of CTB, compared to our SLBs, may be due to its relatively hollow ring structure and height above the membrane of ~20 Å [139]. We also do not detect a modification of membrane structure upon CTB binding, in contrast to reports of CTB-GM1 interaction in monolayers [147]. Studying ligand-receptor binding events in lipid bilayers is more biologically relevant than monolayers; in stable cellular membranes, we do not expect the lipid spacing to readily adjust to ligand binding. In future experiments, gold-conjugated CTB or using both the A and B subunits of cholera toxin may enhance the electron density contrast between CTB and the SLB for measurement with X-ray reflectivity.

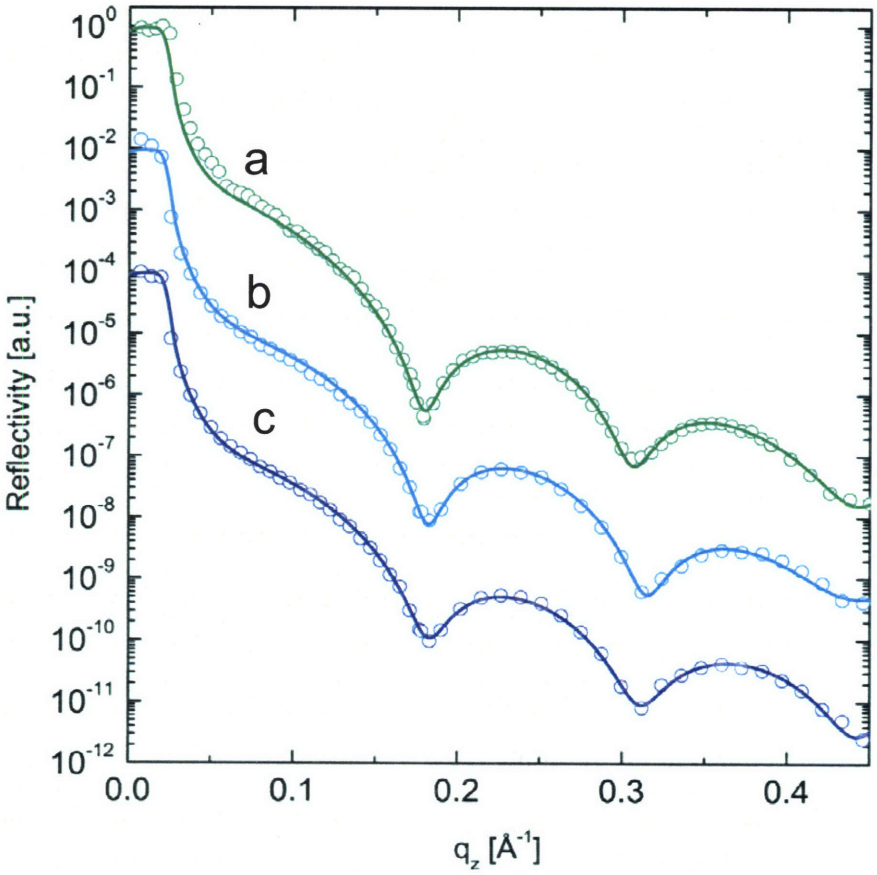

Figure 6-3. Reflectivity of SOPC membranes incubated in GM1 at excess concentrations (*a,c*) and in a LUV solution with SOPC/GM1 stoichiometry of 99/1 (*b*). The SLB in *c* is measured after incubation with CTB; there is no detected change in the reflectivity due to CTB binding GM1.

6.3.2 Model Lipid Rafts at Solid Interfaces

We expect the effect of GM1 on membrane structure in lipid membranes of cholesterol, brain sphingomyelin (BSM) and DOPC to be more complex than GM1 in homogeneous SLBs of SOPC because mixtures of cholesterol/BSM/DOPC phase separate into liquid-disordered and liquid-ordered phases, modeling lipid rafts in cell membranes [4]. This phase separation is readily observed with fluorescence microscopy in fluid lipid bilayer vesicles [4, 45]. On solid-supported interfaces, however, lipid domains lack the reversible phase behavior characteristic of fluid membranes and the domains can be pinned to the substrate [50].

When we prepare SLBs from cholesterol/BSM/DOPC lipid mixtures on the SiO_2 substrates that we use for reflectivity, we do not observe microscopic lipid rafts. Interestingly, when we use a slightly rougher substrate with a 600-nm thick thermal SiO_2 layer and surface roughness ~4-5 Å, we observe microscopic domains. Figure 6-4 compares SLBs with the same lipid composition of 20 mol % cholesterol, 40 mol % BSM and 40 mol % DOPC on a smooth SiO_2 substrate of roughness ~3 Å (Figure 6-4, *a*) and a rough SiO_2 substrate with roughness ~4-5 Å (Figure 6-4, *b*). Only on the rougher SiO_2 substrate are microscopic phases observed: a dark background phase excluding the TR-DPPE dye, and a bright minority phase with relatively round edges. We confirm the fluidity of the SLB in Figure 6-4, *b* by fluorescence bleaching and recovery.

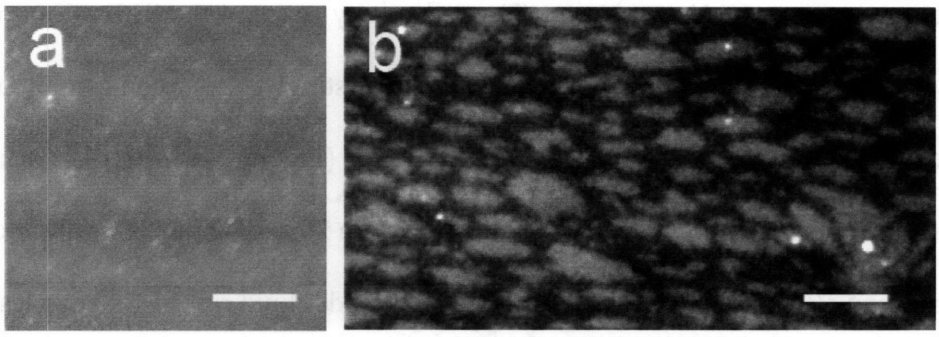

Figure 6-4. SLBs of 20 mol % cholesterol, 40 mol % BSM and 40 mol % DOPC deposited SiO_2 substrates with surface roughness of (*a*) σ = 3 Å and (*b*) σ = 4-5 Å. The thicknesses of the oxide layer are 100 nm in (*a*) and 600 nm in (*b*). Microscopic lipid rafts are only observed on the rougher substrate (*b*). Scale bars are 10 μm.

The rougher SiO_2 substrates that support microscopic lipid phases (Figure 6-4, *b*) do not produce a high-quality X-ray reflectivity signal. Our X-ray reflectivity measurement setup requires molecularly flat SiO_2 substrates with maximum surface roughness 3-3.5 Å; consequently, all of the model lipid raft lipid mixtures that we measure with X-ray reflectivity do not have microscopic lipid phases. Our large incidental X-ray footprint of ~1 mm^2 also precludes measurement of discrete and segregated microscopic phases; thus, our X-ray fitting methods indirectly assume lateral homogeneity in the membrane. It is possible that our model lipid rafts with homogeneous fluorescence (Figure 6-4, *a*) have nanoscopic phases. Lipid phases measured in cells [52, 109] and seen in similar mixtures on flat supported substrates [145, 153] are ~10 nm in size.

We examine the structure of membranes of cholesterol, BSM and DOPC with reflectivity prior to GM1 incubation. The reflectivity scans of the SLBs from our model lipid raft mixtures are shown in Figure 6-5. Interestingly, the second minimum of the reflectivity of the SLB with 30 mol % cholesterol (Figure 6-5, *a*, *II*) is not as clearly defined as the second minima of the membranes with 20 and 40 mol% cholesterol (Figure 6-5, *a*, *I* and *III*). The reflectivity from all of the model lipid raft SLBs have less-defined second minima compared to the reflectivity of homogeneous SOPC (Figure 6-1, *a*). Since the overall quality and resolution of the model raft and SOPC scans are the same, this smearing effect at the second minima may be due to destructive interference, or heterogeneous structures in the membrane of different dimension. This may also be an effect of lipid phase separation, which introduces heterogeneity into the membrane. The electron density profiles extracted from the fits to the reflectivity are shown in Figure 6-5, *b*. The profiles of the cholesterol/BSM/DOPC membranes reveal in more detail the structure of cholesterol-enriched membranes. The most prominent membrane structural changes with increasing cholesterol content are (1) a decrease in the electron density of the lipid headgroups away from the substrate and (2) a concomitant thickening of the lipid bilayer. These trends are summarized in Table 6-1.

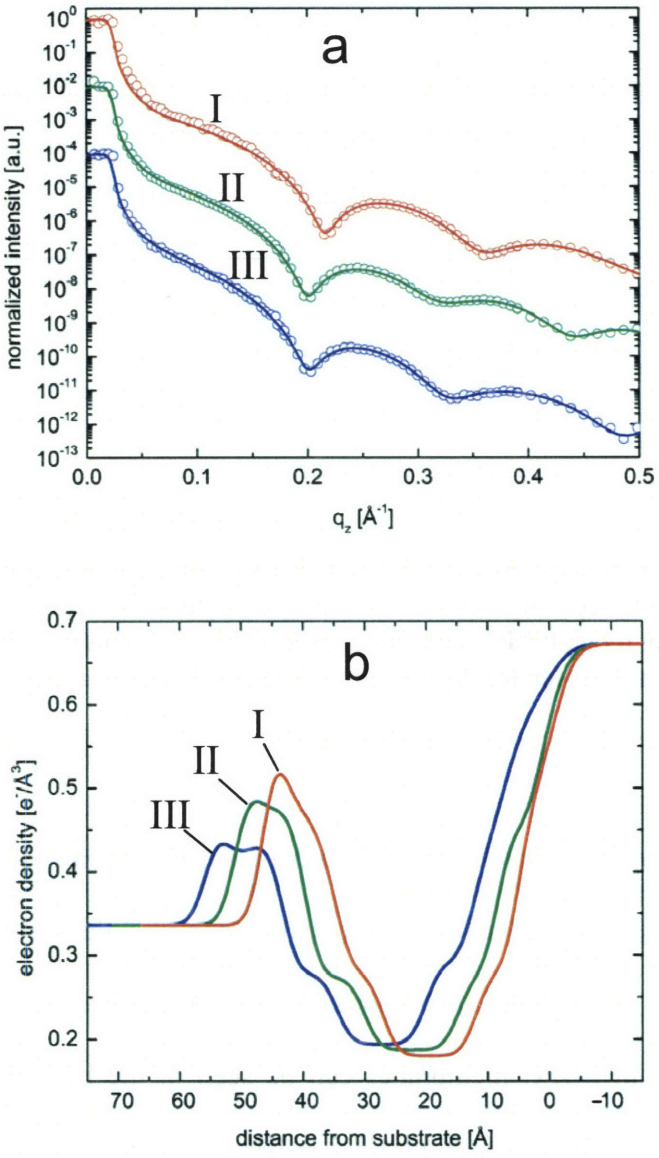

Figure 6-5. Reflectivity (*a*) and electron density profiles (*b*) of SLBs containing cholesterol, BSM and DOPC with fixed 1:1 BSM/DOPC molar ratio and cholesterol concentrations of (*I, red*) 20, (*II, green*) 30, and (*III, blue*) 40 mol %.

Lipid composition	Thickness of the bilayer	Electron density of the headgroup
20 mol % cholesterol 40 mol % BSM 40 mol % DOPC	46 Å	~0.52 $e^-/Å^3$
30 mol % cholesterol 35 mol % BSM 35 mol % DOPC	51 Å	~0.48 $e^-/Å^3$
40 mol % cholesterol 20 mol % BSM 20 mol % DOPC	56 Å	~0.43 $e^-/Å^3$

Table 6-1. Summary parameters from the electron density profiles extracted from reflectivity fits of SLBs with model lipid rafts compositions. The overall bilayer thickness and the electron density of the headgroup of the outer leaflet for each composition are listed.

Our result that cholesterol thickens the bilayer is consistent with previous NMR studies [154]. Lipid rafts enriched in cholesterol are reportedly thicker than typical homogeneous membranes by ~5 Å [153]. An additional feature of these model lipid raft membranes not observed in SOPC membranes can be seen in the hydrophobic chain region of the electron density profiles in Figure 6-5, *b*. The hydrophobic chains appear to have discrete layers of different electron density, indicated by the step-like feature in the profiles at a distance of 30-40 Å. The feature is also noticeable in the lipid chain region near the interface. This may be due to cholesterol arranging in a layer near the lipid headgroups or two different modes of hydrophobic packing in the acyl chain region.

6.3.3 GM1 in Model Lipid Rafts

Using the same method of excess GM1 incubation that we use to prepare GM1-enriched SOPC membranes, we also incorporate GM1 into SLBs of cholesterol/BSM/DOPC. We prepare these SLBs with model lipid rafts by varying the cholesterol concentration and using an equimolar ratio of BSM and DOPC. After incubating the SLBs in GM1 for 4 h, we observe dark spots that exclude TR-DPPE that are not present before GM1 incubation. Figure 6-6 compares a homogenous SLB before incubation (*a*) with SLBs of different cholesterol concentrations after GM1 incubation, after the dark spots form (*b-d*).

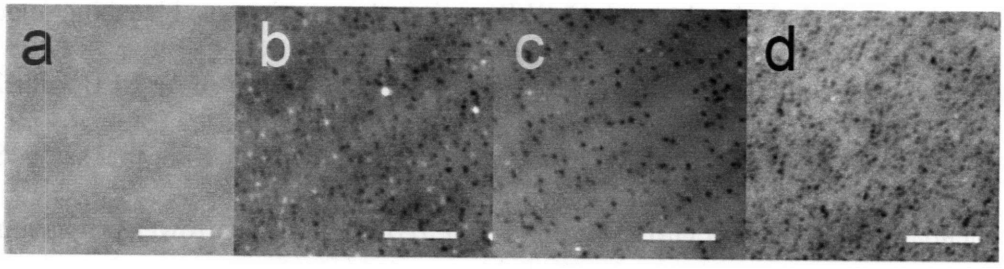

Figure 6-6. Dark defects in membranes (*b-d*) appear after 4 h incubation with excess GM1. (*a*): Before GM1 addition, the SLB of 30 mol % cholesterol, 1:1 DOPC/BSM shows no microsopic features. (*b-d*): SLBs after GM1 incubation with 1:1 DOPC/BSM molar ratio and (*b*) 20, (*c*) 30, and (*d*) 40 mol % cholesterol. Scale bars are 10 μm.

The dark spots remain upon heating to above 70°C, though fluid membranes of these lipid mixtures do not exhibit lipid phase coexistence separation above ~50°C [148]. The stability of the dark spots, combined with their strong exclusion of the dye, suggests that they are membrane defects. Previous experiments show that defects in lipid bilayers at the solid interface can be induced by increasing the tension in the membrane, or reducing the lateral pressure [155]. A defect-inducing mechanism of GM1 could be condensation, whereby the GM1 has an attractive interaction with adjacent lipids; and to accommodate the local packing of lipids due to this interaction, pinholes in the membrane are formed. An attractive electrostatic interaction observed previously in cholesterol/DOPC/BSM mixtures containing GM1 occurs between the sialic acid of GM1 and the positively-charged choline headgroups of DOPC and BSM [145].

We explore this possibility of membrane condensation due to GM1 in model lipid raft membrane mixtures with fluorescence microscopy and we measure the diffusion constants of cholesterol-enriched SLBs using the continuous bleaching method [81]. Figure 6-7 compares the fluorescence intensity line profiles of an SLB with 20 mol % cholesterol, 1:1 (DOPC/BSM) (Figure 6-7, *a, blue line*) with the same SLB after incubation with excess GM1 (Figure 6-7, *b, red line*). The narrower bright rim outlining the illuminated region of the SLB after GM1 incubation (Figure 6-7, *b*) compared to the rim before GM1 incubation (Figure 6-7, *a*) shows the reduction of diffusion of TR-DPPE after GM1 incubation.

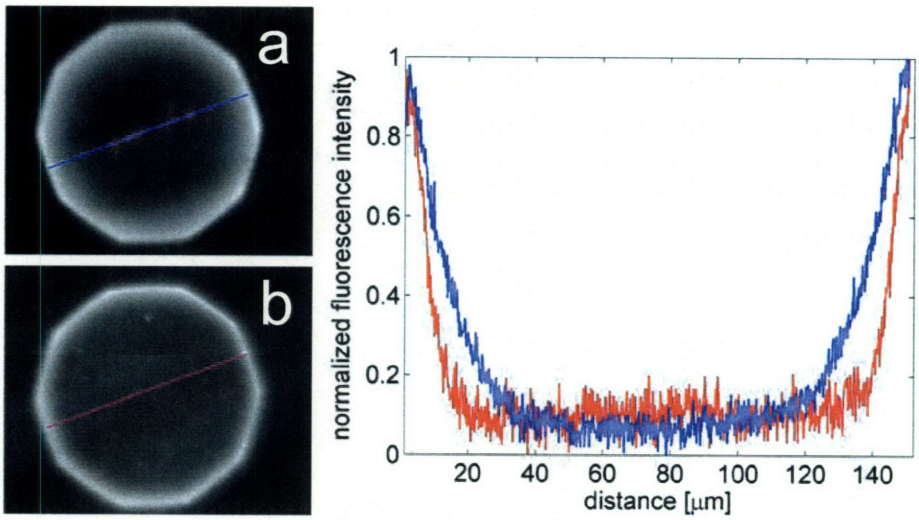

Figure 6-7. Incubation with excess GM1 reduces membrane fluidity. Line profiles after 25 min of continuous bleaching of SLBs from 30 mol % cholesterol, 1:1 DOPC/BSM before (*a, blue*) and after incubation with excess GM1 (*b, red*).

We use the continuous bleaching method outlined in Chapter 5 to measure the diffusion of TR-DPPE in SLBs with model lipid rafts before and after GM1 incubation at three different lipid compositions. Figure 6-8 presents our diffusion measurements for SLBs with an equimolar ratio of DOPC and BSM and 20, 30 and 40 mol% cholesterol. The diffusion constants we measure for cholesterol/DOPC/BSM membranes show the general trend that diffusion is reduced as the concentration of cholesterol is increased. Upon addition of GM1, the lipid diffusion constants are reduced by ~50 %, suggesting that the SLBs enriched in GM1 are more tightly packed than those lacking GM1.

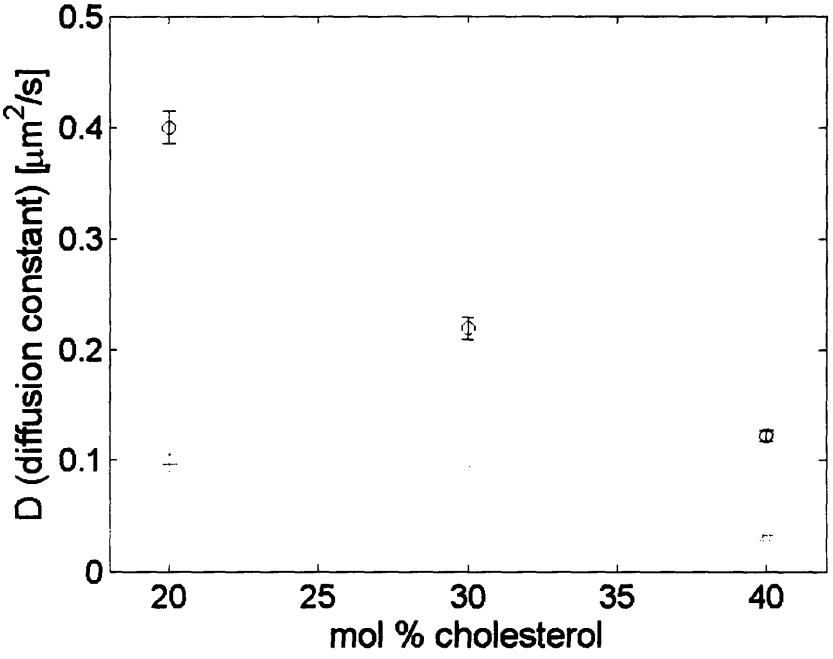

Figure 6-8. Diffusion constants of SLBs with varying cholesterol concentration and 1:1 molar ration BSM/DOPC measured by continuous bleaching without (*black, circles*) and with (*red, triangles*) GM1.

The reduction in the mobility of homogeneous membranes after addition of GM1 is well-established [18, 143, 144]; however, in heterogeneous membranes, where GM1 may influence lipid phase separation [17, 18], lipid diffusion is more complicated. If nanoscopic lipid domains are present, we expect the diffusion to be different between these two domains [4]. And if GM1 changes the lipid phase transitions, then the quantity of the lipid domains and the lipid packing within the domains would also be affected. Gel-phase domains in lipid membranes reduce the fluidity of the surrounding liquid domains as a function of area coverage by creating obstacles for lipid movement [49].

The interplay of these different effects can contribute to the reduction of mobility caused by GM1 in the cholesterol-enriched SLBs.

X-Ray reflectivity allows us to investigate the effect of GM1 on lipid membranes containing model lipid rafts at the molecular level. When we incorporate GM1 into the membrane, we see behavior that is qualitatively similar to the SOPC/GM1 system, as the first minima is shifted towards a lower q_z, indicating a thickening of the layer. Figure 6-9 shows the reflectivity and electron density profiles of the same cholesterol/BSM/DOPC membranes in Figure 6-5 after they have been incubated with excess GM1. The asymmetry of the effect of GM1 is apparent, as only the upper leaflet away from the substrate shows major modifications. At each composition, the outer headgroups are shifted away from the membrane. The outer headgroup density profile of the 20 mol % cholesterol SLB is only partially shifted (Figure 6-9, *b*, *II*), as part of the headgroup profile is centered near its pre-GM1 position of ~45 Å from the substrate. The reflectivity indicates a smearing effect of the second minima (Figure 6-9, *a*), which may be due to destructive interference from heterogeneous structures within the membrane.

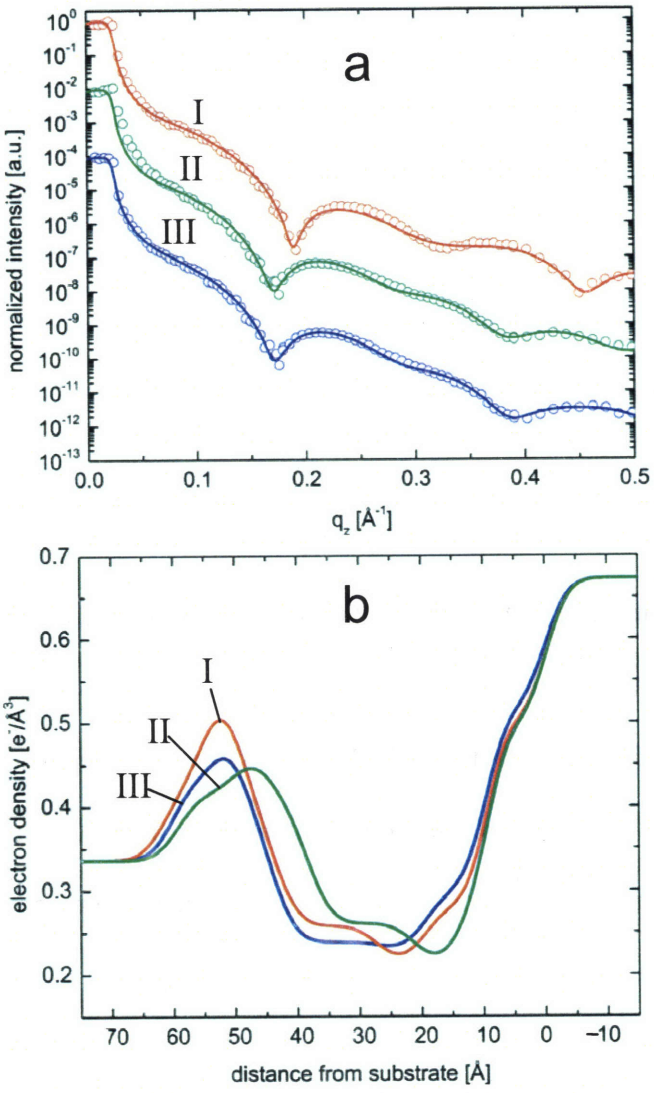

Figure 6-9. Reflectivity (*a*) and electron density profiles (*b*) of SLBs after GM1 incubation. SLBs composed of fixed 1:1 BSM/DOPC molar ratio and cholesterol concentrations of (*I, red*) 20, (*II, green*) 30, and (*III, blue*) 40 mol %.

6.4 Conclusions

The incorporation of GM1 into supported lipid membranes stretches the outer membrane leaflet and increases the lipid headgroup density, consistent with a structural effect of the GM1 headgroup protruding out from the membrane surface. By observing this stretching effect in a homogeneous fluid membrane, we clearly demonstrate the asymmetric insertion of GM1. Heterogeneous lipid bilayers that are able to phase separate into ordered and disordered liquid phases are, however, more representative of cell membranes than homogeneous bilayers. Therefore, we examine SLBs of cholesterol, BSM and DOPC at a solid support. We show that the onset of microscopic phase separation can be influenced by the substrate roughness and that cholesterol has a thickening effect on the membrane. The inclusion of GM1 reduces the lipid diffusion of cholesterol-enriched membranes and introduces defects, suggesting membrane condensation due to GM1 interactions with other lipids. Reflectivity offers an opportunity to systematically study how receptor molecules influence lipid packing and arrangement within membranes.

REFERENCES

(1) Singer, S. J.; Nicolson, G. L. The fluid mosaic model of the stucture of cell membranes. *Science* **1972,** *175*, 720-731.

(2) Edidin, M. Lipids on the frontier: A century of cell-membrane bilayers. *Nature Reviews Molecular Cell Biology* **2003,** *4*, 414-418.

(3) Brown, D. A. Seeing is believing: Visualization of rafts in model membranes. *Proceedings of the National Academy of Sciences of the United States of America* **2001,** *98*, 10517-10518.

(4) Dietrich, C.; Bagatolli, L. A.; Volovyk, Z. N.; Thompson, N. L.; Levi, M.; Jacobson, K.; Gratton, E. Lipid rafts reconstituted in model membranes. *Biophysical Journal* **2001,** *80*, 1417-1428.

(5) Simons, K.; Ikonen, E. Functional rafts in cell membranes. *Nature* **1997,** *387*, 569-572.

(6) Schroeder, R.; London, E.; Brown, D. A. Interactions between saturated acyl chains confer detergent resistance on lipids and glycosylphosphatidylinosital (GPI)-anchored protiens: GPI-anchored proteins in liposomes and cells show similar behavior. *Proceedings of the National Academy of Sciences of the United States of America* **1994,** *91*, 12130-12134.

(7) Dietrich, C.; Volovyk, Z. N.; Levi, M.; Thompson, N. L.; Jacobson, K. Partitioning of Thy-1, GM1 and cross-linked phospholipid analogs into model lipid rafts reconstituted in supported model membrane monolayers. *Proceedings of the National Academy of Sciences of the United States of America* **2001,** *98*, 10642-10647.

(8) Manley, S.; Horton, M. R.; Lecszynski, S.; Gast, A. P. Entropic sorting: Protein crystals on phase-separating model membranes. **2006,** *Submitted for publication.*

(9) Bacia, K.; Schwille, P.; Kurzchalia, T. Sterol structure determines the separation of phases and the curvature of the liquid-ordered phase in model membranes. *Proceedings of the National Academy of Sciences of the United States of America* **2005,** *102*, 3272-3277.

(10) Anderson, R. G. W.; Jacobson, K. A role for lipid shells in targeting proteins to caveolae, rafts and other lipid domains. *Science* **2002,** *296*, 1821-1825.

(11) Kurzchalia, T.; Dupree, P.; Parton, R. G.; Kellner, R.; Virta, H.; Lehnert, M.; Simons, K. VIP21, a 21-kD membrane protein is an integral component of trans-golgi-network-derived transport vesicles. *J. Cell Biol.* **1992,** *118*, 1003-1014.

(12) Palade, G. E. Fine structures of blood capillaries. *Journal of Applied Physics* **1953,** *24*, 424.

(13) Yamada, E. The fine structures of the gall bladder epithelium of the mouse. *Journal of Biophysical and Biochemical Cytology* **1955,** *1*, 445-458.

(14) Rothberg, K. G.; Heuser, J. E.; Donzell, W. C.; Ying, Y.-S.; Glenney, J. R.; Anderson, R. G. W. Caveolin, a protein component of caveolae membrane coats. *Cell* **1992,** *68*, 673-682.

(15) Couet, J.; Belanger, M. M.; Roussel, E.; Drolet, M. C. Cell biology of caveolae and caveolin. *Adv. Drug Delivery. Rev.* **2001,** *49*, 223-235.

(16) Lencer, W. I.; Hirst, T. R.; Holmes, R. Membrane traffic and the cellular uptake of cholera toxin. *Biochimica et Biophysica Acta* **1999,** *1450*, 177-190.

(17) Hammond, A. T.; Heberle, F. A.; Baumgart, T.; Holowka, D.; Baird, B.; Feigenson, G. W. Crosslinking of a lipid raft component triggers liquid ordered-liquid disordered phase separation in model plasma membranes. *Proceedings of the National Academy of Sciences of the United States of America* **2005,** *102*, 6320-6325.

(18) Yamazaki, V.; Sirenko, O.; Schafer, R. J.; Groves, J. T. Lipid mobility and molecular binding in fluid lipid membranes. *Journal of the American Chemical Society* **2005,** *127*, 2826-2827.

(19) Farsad, K.; De Camilli, P. Mechanisms of membrane deformation. *Current Opinion in Cell Biology* **2003,** *15*, 372-381.

(20) Antonny, B. Membrane deformation by protein coats. *Current Opinion in Cell Biology* **2006,** *18*, 386-394.

(21) Bray, D. Signaling complexes: Biophysical constraints on intracellular communication. *Annual Review of Biophysics and Biomolecular Structure* **1998,** *27*, 59-75.

(22) McMahon, H. T.; Gallop, J. L. Membrane curvature and mechanisms of dynamic cell membrane remodelling. *Nature* **2005,** *438*, 590-596.

(23) Heuser, J. E.; Keen, J. Deep-etch visualization of proteins involved in clathrin assembly. *J. Cell Biol.* **1988,** *107*, 877-886.

(24) Mashl, R. J.; Bruinsma, R. F. Spontaneous-curvature theory of clathin-coated membranes. *Biophys. J.* **1998,** *74*, 2862-2875.

(25) Nossal, R. Energetics of clathrin basket assembly. *Traffic* **2001,** *2*, 138-147.

(26) Bielli, A.; Haney, C. J.; Gabreski, G.; Watkins, S. C.; Bannyk, S. I.; Aridor, M. Regulation of Sar1 NH_2 terminus by GTP binding and hydrolysis promotes membrane deformation to control COPII vesicle fission. *Journal of Cell Biology* **2005,** *171*, 919-924.

(27) Lee, M. C. S.; Orci, L.; Hamamoto, S.; Futai, E.; Ravazzola, M.; Schekman, R. Sar1p N-terminal helix initiates membrane curvature and completes the fission of a COPII vesicle. *Cell* **2005,** *122*, 605-617.

(28) Fernandez, I.; Ying, Y.; Albanesi, J.; Anderson, R. G. W. Mechanism of caveolin filament assembly. *Proc. Natl. Acad. Sci. USA* **2002,** *99*, 11193-11198.

(29) Frank, P. G.; Woodman, S. E.; Park, D. S.; Lisanti, M. P. Caveolin, caveolae, and endothelial cell function. *Arteriosclerosis Thrombosis and Vascular Biology* **2003,** *23*, 1161-1168.

(30) Sleytr, U. B.; Sára, M.; Pum, D.; Schuster, B. Characterization and use of crystalline bacterial cell surface layers. *Progress in Surface Science* **2001,** *68*, 231-278.

(31) Mouritsen, O. G.; Andresen, T. L.; Halperin, A.; Hansen, P. L.; Jakobsen, A. F.; Jensen, U. B.; Jensen, M. Ø.; Jørgensen, K.; Kaasgaard, T.; Leidy, C.; Simonsen, A. C.; Peters, G. H.; Weiss, M. Activation of interfacial enzymes at membrane surfaces. *Journal of Physics: Condensed Matter* **2006,** *18*, S1293-S1304.

(32) Adamson, A. W.; Gast, A. P., Surface Films on Liquid Substrates. In *Physical Chemistry of Surfaces, 6th Edition*, John Wiley & Sons, Inc.: 1997; pp 101-158.

(33) Epand, R. M.; Sayer, B. G.; Epand, R. F. Peptide-induced formation of cholesterol-rich domains. *Biochemistry* **2003,** *42*, 14677-14689.

(34) Salditt, T. Structure and fluctuations of highly oriented phospholipid membranes. *Current Opinion in Colloid & Interface Science* **2000,** *5*, 19-26.

(35) Salditt, T.; Li, C.; Spaar, A.; Mennicke, U. X-ray reflectivity of solid-supported, multilamellar membranes. *The European Physical Journal E* **2002,** *7*, 105-116.

(36) Sackmann, E. Supported membranes: Scientific and practical applications. *Science* **1996,** *271*, 43-48.

(37) Reich, C.; Hochrein, M.; Krause, B.; Nickel, B. A microfluidic setup for studies of solid-liquid interfaces using x-ray reflectivity and fluorescence microscopy. *Rev. Sci. Instrum.* **2005,** *76*, 095103.

(38) Miller, C. E.; Majewski, J.; Gog, T.; Kuhl, T. L. Characterization of biological thin films at the solid-liquid interface by X-ray reflectivity. *Physical Review Letters* **2005,** *94*, 238104.

(39) Wagner, M. L.; Tamm, L. K. Tethered polymer-supported planar lipid bilayers for reconstitution of integral membrane proteins: Silane-polyethyleneglycol-lipid as a cushion and covalent linker. *Biophysical Journal* **2000,** *79*, 1400-1414.

(40) Seitz, M.; Park, C. K.; Wong, J. Y.; Israelachvili, J. N. Long-range interaction forces between polymer-supported lipid bilayer membranes. *Langmuir* **2001,** *17*, 4616-4626.

(41) Menger, F. M.; Keiper, J. S. Chemistry and physics of giant vesicles as biomembrane models. *Current Opinion in Chemical Biology* **1998,** *2*, 726-732.

(42) Sankaram, M. B.; Thompson, T. E. Cholesterol-induced fluid-phase immiscibility in membranes. *Proc. Natl. Acad. Sci. USA* **1991,** *88*, 8686-8690.

(43) Radhakrishnan, A.; McConnell, H. Condensed complexes in vesicles containing cholesterol and phospholipids. *Proc. Natl. Acad. Sci. USA* **2005,** *102*, 12662-12666.

(44) Veatch, S. L.; Keller, S. L. Separation of liquid phases in giant vesicles of ternary mixtures of phospholipids and cholesterol. *Biophys. J.* **2003,** *85*, 3074-3083.

(45) Veatch, S. L.; Keller, S. L. Miscibility phase diagrams of giant vesicles containing sphingomyelin. *Physical Review Letters* **2005,** *94*, 148101.

(46) Fantini, J. How sphingolipids bind and shape proteins: Molecular basis of lipid-protein interactions in lipid shells, rafts and related biomembrane domains. *CMLS Cell. Mol. Life Sci.* **2003,** *60*, 1027-1032.

(47) Silvius, J. R. Partitioning of membrane molecules between raft and non-raft domains: Insights from model-membrane studies. *Biochim. Biophys. Acta* **2005,** *1746*, 193-202.

(48) Schlegel, A.; Schwab, R. B.; Scherer, P. E.; Lisanti, M. P. A role for the caveolin scaffolding domain in mediating the membrane attachment of caveolin-1 - The caveolin scaffolding domain is both necessary and sufficient for membrane binding in vitro. *J. Biol. Chem.* **1999,** *274*, 22660-22667.

(49) Ratto, T. V.; Longo, M. L. Obstructed diffusion in phase-separated supported lipid bilayers: A combined atomic force microscopy and fluorescence recovery after photobleaching approach. *Biophysical Journal* **2002,** *83*, 3380-3392.

(50) Stottrup, B. L.; Veatch, S. L.; Keller, S. L. Nonequilibrium behavior in supported lipid membranes containing cholesterol. *Biophysical Journal* **2004,** *86*, 2942-2950.

(51) Chiantia, S.; Kahya, N.; Schwille, P. Dehydration damage of domain-exhibiting supported bilayers: An AFM study on the protective effects of disaccharides and other stabilizing substances. *Langmuir* **2005,** *21*, 6317-6323.

(52) Jacobson, K.; Dietrich, C. Looking at lipid rafts? *Trends in Cell Biology* **1999,** *9*, 87-91.

(53) Edidin, M. Shrinking patches and slippery rafts: Scales of domains in the plasma membrane. *Trends in Cell Biology* **2001,** *11*, 492-496.

(54) Paul, A.; Engelhardt, H.; Jakubowski, U.; Baumeister, W. Two-dimensional crystallization of a bacterial surface protein on lipid vesicles under controlled conditions. *Biophys. J.* **1992,** *61*, 172-188.

(55) Mader, C.; Küpcü, S.; Sára, M.; Sleytr, U. B. Stabilizing effect of an S-layer on liposomes towards thermal or mechanical stress. *Biochimica et Biophysica Acta* **1999,** *1418*, 106-116.

(56) Ratanabanangkoon, P.; Gropper, M.; Merkel, R.; Sackmann, E.; Gast, A. P. Mechanics of streptavidin-coated giant lipid bilayer vesicles: A micropipet study. *Langmuir* **2003,** *19*, 1054-1062.

(57) Vaknin, D.; Als-Nielsen, J.; Piepenstock, M.; Lösche, M. Recognition processes at a functionalized lipid surface observed with molecular resolution. *Biophysical Journal* **1991,** *60*.

(58) Weygand, M.; Kjaer, K.; Howes, P. B.; Wetzer, B.; Pum, D.; Sleytr, U. B.; Lösche, M. Structural reorganization of phospholipid headgroups upon recrystallization of an S-layer lattice. *Journal of Physical Chemistry: B* **2002,** *106*, 5793-5799.

(59) Weygand, M.; Wetzer, B.; Pum, D.; Sleytr, U. B.; Cuvillier, N.; Kjaer, K.; Howes, P. B.; Lösche, M. Bacterial S-layer protein coupling to lipids: X-ray reflectivity and grazing incidence diffraction studies. *Biophysical Journal* **1999,** *76*, 458-468.

(60) Málková, Š.; Long, F.; Stahelin, R. V.; Pingali, S. V.; Murray, D.; Cho, W.; Schlossman, M. L. X-ray reflectivity studies of $cPLA_2\alpha$-C2 domains adsorbed onto Langmuir monolayers of SOPC. *Biophysical Journal* **2005,** *89*, 1861-1873.

(61) Calvert, T. L.; Leckband, D. Two-dimensional protein crystallization at solid-liquid interfaces. *Langmuir* **1997,** *13*, 6737-6745.

(62) Ratanabanangkoon, P.; Gast, A. P. Effect of ionic strength on two-dimensional streptavidin crystallization. *Langmuir* **2003,** *19*, 1794-1801.

(63) Wang, S.-W.; Robertson, C. R.; Gast, A. P. Molecular arrangement in two-dimensional streptavidin crystals. *Langmuir* **1999,** *15*, 1541-1548.

(64) Ku, A. C.; Darst, S. A.; Kornberg, R. D.; Robertson, C. R.; Gast, A. P. Dendritic growth of two-dimensional protein crystals. *Langmuir* **1992,** *8*, 2357-2360.

(65) Green, N. M. Avidin and streptavidin. *Methods in Enzymology* **1990,** *184*, 51-67.

(66) Krueger, S. Neutron reflection from interfaces with biological and biomimetic materials. *Current Opinion in Colloid & Interface Science* **2001,** *6*, 111-117.

(67) Hochrein, M.; Reich, C.; Krause, B.; Rädler, J.; Nickel, B. Structure and mobility of lipid membranes on a thermoplastic substrate. *Langmuir* **2006,** *22*, 538-545.

(68) Vogel, M.; Münster, C.; Fenzl, W.; Salditt, T. Thermal unbinding of highly oriented phospholipid membranes. *Phys. Rev. Lett.* **2000,** *84*, 390-393.

(69) Fang, Y.; Hong, Y.; Webb, B.; Lahiri, J. Applications of biomembranes in drug discovery. *Materials Research Society Bulletin* **2006,** *31*, 541-545.

(70) Menger, F.; Keiper, J. S. Chemistry and physics of giant vesicles as biomembrane models. *Current Opinion in Chemical Biology* **1998,** *2*, 726-732.

(71) Angelova, M. I.; Dimitrov, D. S. Liposome Electroformation. *Faraday Discussions* **1986**, 303-311.

(72) Angelova, M. I.; Soleau, S.; Meleard, P.; Faucon, J. F.; Bothorel, P. Preparation of giant vesicles by external AC electric fields. Kinetics and applications. *Progress in Colloid and Polymer Science* **1992,** *89*, 127-131.

(73) Hope, M. J.; Bally, M. B.; Webb, G.; Cullis, P. R. Production of large unilamellar vesicles by a rapid extrusion procedure: Characterization of size distribution, trapped volume and ability to maintain a membrane potential. *Biochimica et Biophysica Acta* **1985,** *812*, 55-65.

(74) Nollert, P.; Kiefer, H.; Jähnig, F. Lipid vesicle adsorption versus formation of planar bilayers on solid surfaces. *Biophysical Journal* **1995,** *69*, 1447-1455.

(75) Reviakine, I.; Brisson, A. Formation of supported phosholipid bilayers from unilamellar vesicles investigated by atomic force microscopy. *Langmuir* **2000,** *16*, 1806-1815.

(76) Muresan, A. S.; Lee, K. Y. C. Shape evolution of lipid bilayer patches adsorbed on mica: An atomic force microscopy study. *Journal of Physical Chemistry B* **2001,** *105*, 852-855.

(77) Mennicke, U.; Salditt, T. Preparation of solid-supported lipid bilayers by spin-coating. *Langmuir* **2002,** *18*, 8172-8177.

(78) Simonsen, A. C.; Bagatolli, L. A. Structure of spin-coated lipid films and domain formation in supported membranes formed by hydration. *Langmuir* **2004,** *20*, 9720-9728.

(79) Veatch, S. L.; Keller, S. L. Organization in lipid membranes containing cholesterol. *Physical Review Letters* **2002,** *89*, 268101.

(80) Veatch, S. L.; Polozov, I. V.; Gawrisch, K.; Keller, S. L. Liquid domains in vesicles investigated by NMR and fluorescence microscopy. *Biophys. J.* **2004,** *86*, 2910-2922.

(81) Dietrich, C.; Merkel, R.; Tampé, R. Diffusion measurement of fluorescence-labeled amphiphilic molecules with a standard fluorescence microscope. *Biophysical Journal* **1997,** *72*, 1701-1710.

(82) Kahya, N.; Brown, D. A.; Schwille, P. Raft partitioning and dynamic behavior of human placental alkaline phosphatase in giant unilamellar vesicles. *Biochemistry* **2005,** *44*, 7479-7489.

(83) Kahya, N.; Scherfield, D.; Bacia, K.; Poolman, B.; Schwille, P. Probing lipid mobility of raft-exhibiting model membranes by fluorescence correlation spectroscopy. *Journal of Biological Chemistry* **2003,** *278*, 28109-28115.

(84) Rusu, L.; Gambhir, A.; McLaughlin, S.; Rädler, J. Fluorescence correlation spectroscopy studies of peptide and protein binding to phospholipid vesicles. *Biophys. J.* **2004,** *87*, 1044-1053.

(85) Parratt, I. G. Surface studies of solids by total reflection of X-rays. *Physical Review* **1954,** *95*, 359-369.

(86) Murata, M.; Peranen, J.; Schreiner, R.; Weiland, F.; Kurzchalia, T.; Simons, K. VIP21/caveolin is a cholesterol-binding protein. *Proc. Natl. Acad. Sci. USA* **1995,** *92*, 10339-10343.

(87) Ortegren, U.; Karlsson, M.; Blazic, N.; Blomqvist, M.; Nystrom, F. H.; Gustavsson, J.; Fredman, P.; Stralfors, P. Lipids and glycosphingolipids in caveolae and surrounding plasma membrane of primary rat adipocytes. *Eur. J. Biochem.* **2004,** *271*, 2028-2036.

(88) Quest, A. F. G.; Leyton, L.; Parraga, M. Caveolins, caveolae and lipid rafts in cellular transport, signaling and disease. *Biochem. Cell Biol.* **2004,** *82*, 129-144.

(89) Epand, R. M. Do proteins facilitate the formation of cholesterol-rich domains? *Biochim. Biophys. Acta* **2004,** *1666*, 227-238.

(90) Woodman, S. E.; Schlegel, A.; Cohen, A. W.; Lisanti, M. P. Mutational analysis identifies a short atypical membrane attachment sequence (KYWFYR) within caveolin-1. *Biochemistry* **2002,** *41*, 3790-3795.

(91) Wanaski, S. P.; Ng, B. K.; Glaser, M. Caveolin scaffolding region and the membrane binding region of Src form lateral membrane domains. *Biochemistry* **2003,** *42*, 42-56.

(92) Epand, R. M.; Sayer, B. G.; Epand, R. F. Caveolin scaffolding region and cholesterol-rich domains in membranes. *J. Mol. Biol.* **2005,** *345*, 339-350.

(93) Arbuzova, A.; Wang, L.; Wang, J.; Hangyas-Mihalyne, G.; Murray, D.; Honig, B.; McLaughlin, S. Membrane binding of peptides containing both basic and aromatic residues. Experimental studies with peptides corresponding to the scaffolding region of caveolin and the effector region of MARCKS. *Biochemistry* **2000,** *39*, 10330-10339.

(94) Bjellqvist, B.; Basse, B.; Olsen, E.; Celis, J. E. Reference points for comparisons of two-dimensional maps of proteins from different human cell types defined in a pH scale where isoelectric points correlate the polypeptide compositions. *Electrophoresis* **1994,** *15*, 529-539.

(95) Angelova, M. I.; Soleau, S.; Meleard, P.; Faucon, J. F.; Bothorel, P. Preparation of giant vesicles by external AC electric fields. Kinetics and applications. *Progress in Colloid & Polymer Science* **1992,** *89*, 127-131.

(96) Hess, S. T.; Huang, S.; Heikal, A. A.; Webb, W. W. Biological and chemical applications of fluorescence correlation spectroscopy: A review. *Biochemistry* **2002,** *41*, 697-705.

(97) Shogomori, H.; Hammond, A. T.; Ostermeyer, A. G.; Barr, D. G.; Feigenson, G. W.; London, E.; Brown, D. A. Palmitoylation and intracellular domain interactions both contribute to raft targeting of linker for activation of T cells. *J. Biol. Chem.* **2005,** *280*, 18931-18942.

(98) van Duyl, B. Y.; Rijkers, D. T. S.; de Kruijff, B.; Killian, A. Influence of the hydrophobic mismatch and palmitoylation on the association of transmembrane alpha-helical peptides with detergent-resistant membranes. *FEBS Lett.* **2002,** *523*, 79-84.

(99) McIntosh, T. J.; Vidal, A.; Simon, S. A. Sorting of lipids and transmembrane peptides between detergent-soluble bilayers and detergent-resistant rafts. *Biophys. J.* **2003,** *85*, 1656-1666.

(100) Khan, T. K.; Yang, B.; Thompson, N. L.; Maekawa, S.; Epand, R. M.; Jacobson, K. Binding of NAP-22, a calmodulin-binding neuronal protein, to raft-like domains in model membranes. *Biochemistry* **2003,** *42*, 4780-4786.

(101) Wang, T.-Y.; Leventis, R.; Silvius, J. R. Partitioning of lipidated peptide sequences into liquid-ordered lipid domains in model and biological membranes. *Biochemistry* **2001,** *40*, 13031-13040.

(102) Melkonian, K. A.; Ostermeyer, A. G.; Chen, J. Z.; Roth, M. G.; Brown, D. A. Role of lipid modifications in targeting raft proteins to detergent-resistant membrane rafts. *J. Biol. Chem.* **1999,** *274*, 3910-3917.

(103) Sargiacomo, M.; Scherer, P. E.; Tang, Z.; Kübler, E.; Song, K. S.; Sanders, M. C.; Lisanti, M. P. Oligomeric structure of caveolin-1: implications for caveolae membrane organization. *Proc. Natl. Acad. Sci. USA* **1995,** *92*, 9407-9411.

(104) Schlegel, A.; Lisanti, M. P. A molecular dissection of caveolin-1 membrane attachment and oligomerization. *J. Biol. Chem.* **2000,** *275*, 21605-21617.

(105) Pol, A.; Martin, S.; Fernandez, M. A.; Ingelmo-Torres, M.; Ferguson, C.; Enrich, C.; Parton, R. G. Cholesterol and fatty acids regulate dynamic caveolin trafficking through the Golgi complex and between the cell surface and lipid bodies. *Mol. Biol. Cell* **2005,** *16*, 2091-2105.

(106) Razani, B.; Lisanti, M. P. Caveolins and caveolae: Molecular and functional relationships. *Exp. Cell Res.* **2001,** *271*, 36-41.

(107) Fra, A. M.; Williamson, E.; Simons, K.; Parton, R. G. *De novo* formation of caveolae in lymphocytes by expression of VIP21-caveolin. *Proc. Natl. Acad. Sci. USA* **1995,** *92*, 8655-8659.

(108) London, E.; Brown, D. A. Insolubility of lipids in Triton X-100: Physical origin and relationship to sphingolipid/cholesterol membrane domains (rafts). *Biochim. Biophys. Acta* **2000,** *1508*, 182-195.

(109) Munro, S. Lipid rafts: Elusive or illusive? *Cell* **2003,** *115*, 377-388.

(110) Devaux, P.; Morris, R. Transmembrane asymmetry and lateral domains in biological membranes. *Traffic* **2004,** *5*, 241-246.

(111) Wang, T.-Y.; Silvius, J. R. Cholesterol does not induce segregation of liquid-disordered domains in bilayers modeling the inner leaflet of the plasma membrane. *Biophys. J.* **2001,** *81*, 2762-2773.

(112) London, E. How principles of domain formation in model membranes may explain ambiguities concerning lipid raft formation in cells. *Biochim. Biophys. Acta* **2005,** *1746*, 203-220.

(113) Seul, M.; Andelman, D. Domain shapes and patterns: The phenomenology of modulated phases. *Science* **1995,** *267*, 476-483.

(114) McConnell, H. Complexes in ternary cholesterol-phospholipid mixtures. *Biophys. J.* **2005,** *88*, L23-L25.

(115) Ratanabanangkoon, P.; Gropper, M.; Merkel, R.; Sackmann, E.; Gast, A. P. Two-dimensional streptavidin crystals on giant lipid bilayer vesicles. *Langmuir* **2002,** *18*, 4270-4276.

(116) Angelova, M. I.; Soleau, S.; Meleard, P.; Faucon, J.-F.; Bothorel, P. Preparation of giant vesicles by external AC electric fields. Kinetics and applications. *Prog. in Colloid & Polymer Sci.* **1992,** *89*, 127-131.

(117) Döbereiner, H.-G.; Käs, J.; Noppl, D.; Sprenger, I.; Sackmann, E. Budding and fission of vesicles. *Biophys. J.* **1993,** *65*, 1396-1403.

(118) Saffman, P. G.; Delbrück, M. Brownian motion in biological membranes. *Proc. Natl. Acad. Sci. USA* **1975,** *72*, 3111-3113.

(119) Du, F.; Fischer, J. E.; Winey, K. I. Effect of nanotube alignment on percolation conductivity in carbon nanotube/polymer composites. *Phys. Rev. B* **2005,** *72*, 121404.

(120) Xia, W.; Thorpe, M. F. Percolation of random ellipses. *Phys. Rev. A* **1988,** *38*, 2650-2656.

(121) Ménager, C.; Cabuil, V. Reversible shrinkage of giant magnetoliposomes under an osmotic stress. *J. Phys. Chem. B* **2002,** *106*, 7913-7918.

(122) Mathivet, L.; Cribier, S.; Devaux, P. F. Shape change and physical properties of giant phospholipid vesicles prepared in the presence of an AC electric field. *Biophys. J.* **1996,** *70*, 1112-1121.

(123) Viallat, A.; Dalous, J.; Abkarian, M. Giant lipid vesicles filled with a gel: Shape instability induced by osmotic shrinkage. *Biophys. J.* **2004,** *86*, 2179-2187.

(124) Guedeau-Boudeville, M.-A.; Bernard, A.-L.; Bradley, J.-C.; Singh, A.; Jullien, L., In *Giant Vesicles*, Luisi, P. L.; Walde, P., Eds. John Wiley & Sons Ltd.: Chichester, U.K., 2000; pp Ch. 26, 341-349.

(125) Hotani, H. Transformation pathways of liposomes. *Journal of Molecular Biology* **1984,** *178*, 113-120.

(126) Seifert, U.; Berndl, K.; Lipowsky, R. Shape transformations of vesicles: Phase diagram for spontaneous-curvature and bilayer-coupling models. *Phys. Rev. A* **1991,** *44*, 1182-1202.

(127) Vaknin, D.; Kjaer, K.; Ringsdorf, H.; Blankenburg, R.; Piepenstock, M.; Diederich, A.; Lösche, M. X-ray and neutron reflectivity studies of a protein monolayer adsorbed to a functionalized aqueous surface. *Langmuir* **1993,** *9*, 1171-1174.

(128) Salditt, T. Lipid-peptide interaction in oriented bilayers probed by interface-sensitive scattering methods. *Current Opinion in Structural Biology* **2003,** *13*, 467-478.

(129) Nováková, E.; Giewekemeyer, K.; Salditt, T. Structure of two-component lipid membranes on solid support: An x-ray reflectivity study. *Physical Review E* **2006,** 051911.

(130) Ratanabanangkoon, P.; Gast, A. P. Effect of ionic strength on two-dimensional streptavidin crystallization. *Langmuir* **2003,** *19*, 1794-1801.

(131) Ku, A. C.; Darst, S. A.; Kornberg, R. D.; Robertson, C. R.; Gast, A. P. Dendritic growth of two-dimensional protein crystals. *Langmuir* **1992,** *1992*, 2357-2360.

(132) Gast, A. P.; Robertson, C. R.; Wang, S.-W.; Yatcilla, M. T. Two-dimensional streptavidin crystals: macropatterns and micro-organization. *Biomolecular Engineering* **1999,** *16*, 21-27.

(133) Zhang, L.; Granick, S. Slaved diffusion in phospholipid bilayers. *Proceedings of the National Academies of Science of the United States of America* **2005,** *102*, 9118-9121.

(134) Hendrickson, W. A.; Pähler, A.; Smith, J. L.; Satow, Y.; Merritt, E. A.; Phizackerley, R. P. Crystal structure of core streptavidin determined from multiwavelength anomalous diffraction of synchrotron radiation. *Proceedings of the National Academies of Science of the United States of America* **1989,** *86*, 2190-2194.

(135) Horton, M. R.; Manley, S.; Arevalo, S.; Lobkovsky, A. E.; Gast, A. P. Crystalline protein domains and lipid bilayer vesicle shape transformations. *Journal of Physical Chemistry B* **2006,** *accepted.*

(136) Sackmann, E.; Evans, E. Translational and rotational drag coefficients for a disk moving in a liquid membrane associated with a rigid substrate. *Journal of Fluid Mechanics* **1988,** *194*, 553-561.

(137) Rosano, C.; Arioso, P.; Bolognesi, M. The X-ray three-dimensional structure of avidin. *Biomolecular Engineering* **1999,** *16*, 5-12.

(138) Lösche, M.; Piepenstock, M.; Diederich, A.; Grünewald, T.; Kjaer, K.; Vaknin, D. Influence of surface chemistry on the structural organization of monomolecular protein layers adsorbed to functionalized aqueous interfaces. *Biophysical Journal* **1993,** *65*, 2160-2177.

(139) Merrrit, E. A.; Sarfaty, S.; van den Akker, F.; L'Hoir, C.; Martial, J. A.; Hol, W. G. J. Crystal structure of cholera toxin B-pentamer bound to receptor G_{M1} pentasaccharide. *Protein Science* **1994,** *3*.

(140) Ribi, H. O.; Ludwig, D. S.; Mercer, K. L.; Schoolnik, G. K.; Kornberg, R. D. Three-dimensional structure of cholera toxin penetrating a lipid membrane. *Science* **1998,** *239*, 1272-1276.

(141) Samsanov, A. V.; Mihalyov, I.; Cohen, F. S. Characterization of cholesterol-sphingomyelin domains and their dynamics in bilayer membranes. *Biophysical Journal* **2001,** *81*, 1486-1500.

(142) Bacia, K.; Majoul, I. V.; Schwille, P. Probing the endocytotic pathway in live cells using dual-color fluorescence cross-correlation analysis. *Biophysical Journal* **2002,** *83*, 1184-1193.

(143) Goins, B.; Masserini, M.; Barisas, B. G.; Freire, E. Lateral diffusion of ganglioside G_{M1} in phospholipid bilayer membranes. *Biophysical Journal* **1986,** *49*, 849-856.

(144) Weng, K. C.; Kanter, J. L.; Robinson, W. H.; Frank, C. W. Fluid supported lipid bilayers containing monosialoganglioside GM1: A QCM-D and FRAP study. *Colloids and Surfaces B: Biointerfaces* **2006,** *50*, 76-84.

(145) Yuan, C.; Furlong, J.; Burgos, P.; Johnston, L. J. The size of lipid rafts: An atomic force microscopy study of ganglioside GM1 domains in sphingomyelin/DOPC/cholesterol membranes. *Biophysical Journal* **2002,** *82*, 2526-2535.

(146) Yuan, C.; Johnston, L. J. Atomic force microscopy studies of ganglioside GM1 domains in phosphatidylcholine and phosphatidylcholine/cholesterol bilayers. *Biophysical Journal* **2001,** *81*, 1059-1069.

(147) Miller, C. E.; Majewski, J.; Faller, R.; Satija, S.; Kuhl, T. L. Cholera toxin assault on lipid monolayers containing ganglioside GM_1. *Biophysical Journal* **2004,** *86,* 3700-3708.

(148) Horton, M. R.; Rädler, J.; Gast, A. P. Phase behavior and the partitioning of caveolin-1 scaffolding domain peptides in model lipid bilayers. *Journal of Colloid and Interface Science* **2006,** *304,* 67-76.

(149) Wang, R.; Shi, J.; Parikh, A. N.; Shreve, A. P.; Chen, L.; Swanson, B. I. Evidence for cholera aggregation on GM1-decorated lipid bilayers. *Colloids and Surfaces B: Biointerfaces* **2004,** *33,* 45-51.

(150) Cantú, L.; Corti, M.; Del Favero, E.; Muller, E.; Raudino, A.; Sonnino, S. Thermal hysteresis in ganglioside micelles investigated by differential scanning calorimetry and light-scatterin. *Langmuir* **1999,** *15,* 4975-4980.

(151) Hirai, M.; Iwase, H.; Hayakawa, T.; Koizumi, M.; Takahashi, H. Determination of asymmetric structure of ganglioside-DPPC mixed vesicle using SANS, SAXS, and DLS. *Biophysical Journal* **2003,** *85,* 1600-1610.

(152) McIntosh, T. J.; Simon, S. A. Long- and short-range interactions between phospholipid/ganglioside GM1 bilayers. *Biochemistry* **1994,** *33,* 10477-10486.

(153) Lawrence, J. C.; Saslowsky, D. E.; Edwardson, J. M.; Henderson, R. M. Real-time analysis of the effects of cholesterol on lipid raft behavior using atomic force microscopy. *Biophysical Journal* **2003,** *84,* 1827-1832.

(154) Nezil, F. A.; Bloom, M. Combined influence of cholesterol and synthetic amphiphilic peptides upon bilayer thickness in model membranes. *Biophysical Journal* **1992,** *61,* 1176-1183.

(155) McConnell, H.; Tamm, L. K. Supported phosholipid bilayers. *Biophysical Journal* **1985,** *47,* 105-113.